Nonlinear interfacial waves in two/three-layer Euler flows

by

Xin Guan

A thesis submitted in conformity with the requirements
for the degree of Doctor of Philosophy

Department of Mathematics
Faculty of Mathematical & Physical Sciences
University College London

March, 2024

Disclaimer

I, Xin Guan, confirm that the work presented in this thesis is my own. Where information has been derived from other sources, I confirm that this has been indicated in the thesis.

Signature ____________________

Date ____________________

Abstract

In this thesis, we focus on two-dimensional interfacial waves in layered incompressible Euler flows. An unified numerical scheme based on Cauchy's integral formula is used to calculate fully nonlinear travelling waves. This method allows us to obtain almost singular solutions, known as limiting configurations. We also study their bifurcation structure and find a generic bifurcation mechanism due to symmetric breaking. The thesis is organised as follows. In chapter 1, we give an introduction. In chapter 2, we describe the fundamental mathematical formulation and the boundary-integral method. In chapter 3, we study two-layer gravity solitary waves and their limiting configuration. In chapter 4, we go to the two-layer gravity periodic waves and explain their bifurcation mechanism. In chapter 5, we study interfacial capillary waves and show their limiting configurations. In chapter 6, we study more complex three-layer periodic gravity waves. In chapter 7, we discuss possible future work. Chapter 8 is a conclusion.

This thesis was completed under the supervision of ***Professor Jean-Marc Vanden-Broeck****.*

Impact Statement

The work in this thesis concerns two-dimensional interfacial waves that occur in two/three-layer incompressible Euler flows, which are widely used in fluid dynamics to model oceanic internal waves.

Over the ourse of the PhD, the results in the thesis have been published in a variety of journals. They include Guan et al. [37], Guan et al. [35], Guan et al. [36], Nie et al. [60], Guan et al. [33] and Guan and Vanden-Broeck [34]. Some of the results have been presented in different conferences in the UK (BAMC Bristol 2023, Edinburgh 2023, Essex 2024).

The numerical methods used in this thesis provide a universal approach to two-dimensional travelling waves in multilayer flows. The superiority is illustrated in its numerical accuracy and the ability to calculate almost singular solutions. Various new solutions have been found for the first time. A generic bifurcation mechanism due to symmetry breaking has also been observed in different scenarios. These not only provide new research directions for pure mathematicians, but also give rise to the challenge to search for these solutions in the nature or laboratory.

UCL Research Paper Declaration Form

1. **For a research manuscript that has already been published** (if not yet published, please skip to section 2):
   - (a) **What is the title of the manuscript?**
     - [1] A local model for the limiting configuration of interfacial solitary waves
     - [2] New solutions for periodic interfacial gravity waves
     - [3] New solutions for interfacial capillary waves of permanent form
     - [4] Nonlinear travelling periodic waves for the Euler equations in three-layer flows
   - (b) **Please include a link to or doi for the work:**
     - [1] https://doi.org/10.1017/jfm.2021.521
     - [2] https://doi.org/10.1017/jfm.2021.854
     - [3] https://doi.org/10.1017/jfm.2022.882
     - [4] https://doi.org/10.1017/jfm.2024.73
   - (c) **Where was the work published?**
     - [1] Journal of Fluid Mechanics
     - [2] Journal of Fluid Mechanics

  - [3] Journal of Fluid Mechanics
  - [4] Journal of Fluid Mechanics

(d) **Who published the work?**

  - [1] Cambridge University Press
  - [2] Cambridge University Press
  - [3] Cambridge University Press
  - [4] Cambridge University Press

(e) **When was the work published?**

  - [1] 25/6/2021
  - [2] 12/12/2021
  - [3] 11/11/2022
  - [4] 19/2/2024

(f) **List the manuscript's authors in the order they appear on the publication:**

  - [1] Xin Guan, Jean-Marc Vanden-Broeck, Zhan Wang, Frederic Dias
  - [2] Xin Guan, Jean-Marc Vanden-Broeck, Zhan Wang
  - [3] Xin Guan, Jean-Marc Vanden-Broeck, Zhan Wang
  - [4] Xin Guan, Alex Doak, Paul Milewski, Jean-Marc Vanden-Broeck

(g) **Was the work peer reviewed?**

  - [1] Yes
  - [2] Yes
  - [3] Yes
  - [4] Yes

(h) **Have you retained the copyright?**

  - [1] Yes

  - [2] Yes
  - [3] Yes
  - [4] Yes

(i) **Was an earlier form of the manuscript uploaded to a preprint server (e.g. medRxiv)? If 'Yes', please give a link or doi** If 'No', please seek permission from the relevant publisher and check the box next to the below statement:

  - [1] No
  - [2] No
  - [3] No
  - [4] No

☐ *I acknowledge permission of the publisher named under 1d to include in this thesis portions of the publication named as included in 1c.*

2. **For a research manuscript prepared for publication but that has not yet been published (if already published, please skip to section 3):**

(a) **What is the current title of the manuscript?** A novel boundary-integral algorithm for nonlinear unsteady surface and interfacial waves

(b) **Has the manuscript been uploaded to a preprint server 'e.g. medRxiv'? If 'Yes', please please give a link or doi:** Yes. https://doi.org/10.48550/arXiv.2312.13019

(c) **Where is the work intended to be published?** Journal of Computational Physics

(d) **List the manuscript's authors in the intended authorship order:** Xin Guan, Jean-Marc Vanden-Broeck

(e) **Stage of publication:** To be submitted

3. **For multi-authored work, please give a statement of contribution covering all authors** (if single-author, please skip to section 4):

   [1] Xin Guan: computation and original draft; Jean-Marc Vanden-Broeck: methodology and supervision; Zhan Wang: writing–review and editing; Frederic Dias: conceptualization.

   [2] Xin Guan: computation and original draft; Jean-Marc Vanden-Broeck: methodology and supervision; Zhan Wang: writing–review and editing.

   [3] Xin Guan: computation and original draft; Jean-Marc Vanden-Broeck: methodology and supervision; Zhan Wang: writing–review and editing.

   [4] Xin Guan: computation and original draft; Alex Doak: writing–review and editing; Paul Milewski: conceptualization; Jean-Marc Vanden-Broeck: supervision.

4. **In which chapter(s) of your thesis can this material be found?**

   [1] Chapter 3.

   [2] Chapter 4.

   [3] Chapter 5.

   [4] Chapter 6.

Candidate: Xin Guan

Date: 31/3/2024

Supervisor/Senior Author signature (where appropriate): Jean-Marc Vanden-Broeck

Date: 31/3/2024

Acknowledgments

Firstly I would like to thank Professor Jean-Marc Vanden-Broeck for his fantastic supervision and Professor Zhan Wang for his brilliant academic help.

Secondly I would like to thank all the supporting staff at the Department of Mathematics, UCL.

Thirdly I would like to thank the Chinese Scholarship Council (CSC) for their financial support over the course of PhD.

Finally I would like to thank my parents and sister for their continuous support.

Xin Guan, *University College London*, March 2024

To my parents and sister.

The genius of Laplace was a perfect sledge hammer in bursting purely mathematical obstacles; but, like that useful instrument, it gave neither finish nor beauty to the results. In truth, in truism if the reader please, Laplace was neither Lagrange nor Euler, as every student is made to feel. The second is power and symmetry, the third power and simplicity; the first is power without either symmetry or simplicity. But, nevertheless, Laplace never attempted investigation of a subject without leaving upon it the marks of difficulties conquered: sometimes clumsily, sometimes indirectly, always without minuteness of design or arrangement of detail; but still, his end is obtained and the difficulty is conquered.

—Augustus De Morgan

Contents

List of Tables

List of Figures

Chapter 1

Introduction

Waves propagating at the interface(s) inside a fluid are usually called interfacial waves. Typical examples include internal waves in oceans, lee waves in atmosphere, etc. When viscosity is negligible, interfacial waves can be mathematically described by the Euler equations. If the density of the fluids is constant except in a thin layer, we can assume that the interface has zero thickness. The model is then simplified to layered Euler equations with free boundaries, which must be found as part of the solution.

The exploration of interfacial waves began in the last half-century through pioneering work in theoretical studies [5, 9, 64], numerical simulations [30, 56, 76] and experiments [46, 57]. In contrast to the classical water waves, which have been extensively studied for over a century, interfacial waves pose greater challenges and continue to be explored in terms of their bifurcations, limiting configurations and dynamics. The primary difficulty in studying interfacial waves arises from the discontinuity of the tangential velocity across the interface and the property that interfaces can develop multi-valued profiles.

Travelling interfacial waves driven by gravity were first studied by Holyer [41] who found that a vertical tangent appeared on the interface when solutions become highly nonlinear. Holyer asserted that these solutions represent the limiting configurations of interfacial waves. Subsequently, Meiron and Saffman [56] extended Holyerl's solutions to multi-valued profiles, known as "overhanging solutions". In fact, if Holyer had used other variables instead of the horizontal physical coordinate in her Fourier expansion, she would also have discovered these overhanging waves. Grimshaw and Pullin [30] and Turner and Vanden-Broeck [76] used different numerical formulations and found similar results. The overhanging property of interfacial waves is totally different from the behaviour of travelling gravity water waves whose limiting configuration has a local corner with 120° angle at the crest, known as the " highest Stokes waves". Grimshaw and Pullin [30] proposed a novel limiting configuration which has a closed fluid bubble sitting on top of a highest Stokes wave. Later, they found that the same type of solutions exists for interfacial solitary waves [67]. Due to its highly nonlinear nature and singularity, these solutions pose significant challenges for numerical computation. Classical conformal mapping techniques, popular for water waves, prove inefficient in addressing the complexities of interfacial waves [65].

Recent advancements by Maklakov and Sharipov [55] and Maklakov [54] introduced a novel numerical formulation, enabling highly accurate simulations of periodic interfacial gravity waves in deep water. Their simulations yielded almost limiting solutions, supporting the conjecture of Pullin and Grimshaw regarding the overhanging limiting configuration [28]. In chapters 3 and 4, this conjecture will be further explored using an alternative yet more universally applicable numerical scheme and a localized simplified model. We will show that there are secondary bifurcations due to a symmetry-breaking mechanism.

For interfacial gravity solitary waves, the overhanging limiting configuration is not the only possibility. Amick and Turner [5] proved that in a two-layer fluid system, solitary waves tend to either develop an infinite slope, or an internal front by broadening infinitely. Subsequently, such broadening solutions were numerically found by Funakosh and Oikawa [29] and Turner and Vanden-Broeck [77] in two-layer fluid system, and Rusås and Grue [69] in three-layer fluid system. It is interesting to point out that although Amick and Turner [5] did not exclude the possibility that overhanging solutions and broadening solutions can co-exist for a given density ratio and depth ratio, no supporting numerical evidence was presented. It is found that when the depth ratio $h = h_2/h_1$ is small, where $h_{1,2}$ denote the depth of the lower and upper layer, respectively, solitary waves tend to develop the broadening solutions. This aligns with the laboratory experiments where very wide solitary waves are frequently observed [32, 58]. Overhanging solitary waves, on the other hand, usually emerge when $h \gg 1$. For example, Pullin and Grimshaw [67] assumed that the upper fluid layer is infinitely deep in their calculations. It is very likely that the broadening solutions and the overhanging solutions exist in different ranges of parameters, which may have some overlaps. To the best knowledge of the author, this is still an open question so far.

When the effect of surface tension is important, the typical characteristics of waves undergo significant changes. Crapper [23] and Kinnersley [45] found analytical solutions of surface capillary water waves in infinite and finite depths, respectively. These solutions exhibit overhanging profiles with a U-shape, ultimately becoming self-intersecting. This limiting configuration can be conceptualized as the free surface developing a point of contact with a 'trapped bubble' at the trough. Subsequently, Crowdy [24] provided an alternative derivation of Crapper waves using conformal mapping method. As for numerical computation, Blyth and Vanden-Broeck [12] studied capillary waves on fluid sheets and found secondary bifurcation branches on Kinnersley's symmetric solution branch. Akers et al. [1] conducted computations on travelling capillary waves between two semi-infinite fluids of equal density in the presence of background shear currents. Additionally, Akers et al. [2] studied gravity perturbed Crapper waves and the existence of overhanging capillary-gravity waves. In the chapter 5, we will study travelling interfacial capillary waves in finite depths.

We will show that the symmetry-breaking mechanism also emerges and leads to different limiting configurations.

So far, we only talked about two-layer interfacial waves. In chapter 6, we will extend the numerical study to three-layer interfacial waves which involve two interfaces. Such a model originates from the fact that ocean is weakly density-stratified in vertical direction. The most dramatic change happens within a thin layer, known as the pycnocline. The two-layer model assumes all streamlines have the same polarity, i.e. they are all in phase, thus replacing the thin layer by an interface. This is a good approximation of the mode-1 waves. However, there is evidence from field observations and laboratory experiments [17, 26] showing the existence of mode-2 waves, i.e., streamlines show opposite polarity. In such cases, the three-layer interfacial wave model becomes the simplest representation. Previous studies of three-layer model mostly focus on weakly nonlinear theories such as the modified Korteweg-de Vries equation [31] and Gardner equation [47]. Meanwhile, the strongly nonlinear but weakly dispersive three-layer Miyata-Choi-Camassa equations [20, 59] were explored by Jo and Choi [44] and Barros et al. [8]. Using a fully nonlinear theory, a detailed description of three-layer conjugate states was obtained by Lamb [48]. Fully nonlinear wave computations have been computed by previous authors, who explored both mode-1 [69] and mode-2 [27] solitary waves. Fully nonlinear mode-1 and mode-2 periodic waves have been computed [19, 68]. However, a detailed description of the bifurcation space is thus far lacking, and will be presented in chapter 6.

The thesis is structured as the following. In chapter 2, we discuss the basic mathematical formulation and boundary-integral method used throughout the thesis. In chapter 3, we investigate interfacial gravity solitary waves in two-layer flows. In chapter 4, we study the periodic gravity waves in two-layer flows. In chapter 5, two-layer periodic capillary waves are studied. In chapter 6, the formulation is extended to three-layer gravity waves. Chapter 6 is a discussion about future work. Chapter

7 is a conclusion.

Chapter 2

Mathematical formulation and numerical scheme

2.1 Layered-Euler equations

In this thesis, we investigate two-dimensional waves propagating at the interface(s) of multiple immiscible fluids. The fundamental assumptions are that the flow is irrotational and inviscid, and that each fluid is incompressible with a constant density. Taking the two-layer system as an illustration (see figure 2.1), the fluid motion is governed by the Euler equations

$$\frac{\partial \boldsymbol{u}_i}{\partial t} + \boldsymbol{u}_i \cdot \nabla \boldsymbol{u}_i = -\frac{1}{\rho_i}\nabla p - g\boldsymbol{j}, \tag{2.1}$$

$$\nabla \cdot \boldsymbol{u}_i = 0, \tag{2.2}$$

where we denote values of the unknowns with a subscript $i = 1$ for the lower fluid and a subscript $i = 2$ for the upper fluid, $\boldsymbol{u}_i$ represents the velocity vector, $\nabla = (\partial_x, \partial_y)$ in Cartesian coordinates (x, y) and $\boldsymbol{j}$ is the unit vector pointing in the positive $y-$direction.

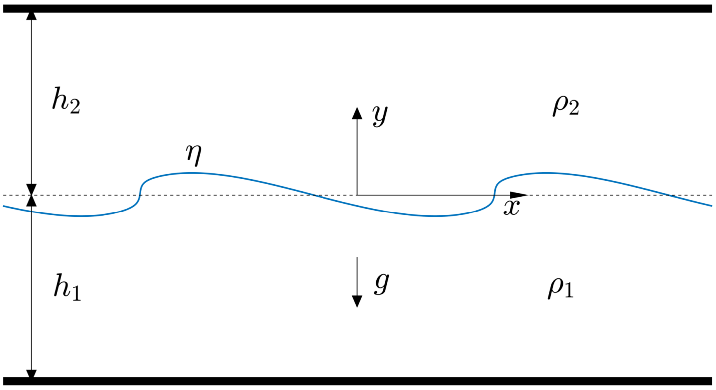

Figure 2.1: Schematic of the two-layer flow.

On the interface $y = \eta(x, t)$, we have kinematic boundary condition

$$\frac{\partial \eta}{\partial t} + u_i \frac{\partial \eta}{\partial x} = v_i, \tag{2.3}$$

where u_i and v_i are the velocity components in $x-$direction and $y-$direction, respectively. We assume that both fluids have a finite depth h_i and there are two flat walls on top $(i = 2)$ and bottom $(i = 1)$ where the impermeable condition holds

$$v_i = 0. \tag{2.4}$$

In real oceanic scenarios, the top boundary is a free surface instead of a solid wall. However, it turns out that the motion of free surface has little effects on the interface [28]. As a result, the free surface is usually replaced by a flat wall. This is known as the "rigid-lid assumption".

Using the assumption that flows are irrotational, we can further simplify equations (2.1) to (2.4) by introducing the velocity potential functions ϕ_i such that

$$\boldsymbol{u}_i = \nabla \phi_i. \tag{2.5}$$

Then, the incompressibility condition (2.2) becomes the well-known Laplace equation in each fluid layer

$$\nabla^2 \phi_i = 0. \tag{2.6}$$

The momentum equation (2.1) can be integrated and becomes the Bernoulli equation on the interface

$$\frac{\partial \phi_i}{\partial t} + \frac{1}{2}|\nabla \phi_i|^2 + g\eta + \frac{p_i}{\rho_i} = 0. \tag{2.7}$$

The pressures p_i can be eliminated by imposing the balance condition of normal stress

$$p_2 - p_1 = \begin{cases} \sigma\kappa, & \text{with surface tension,} \\ 0, & \text{without surface tension,} \end{cases} \tag{2.8}$$

where σ is the surface tension coefficient and $\kappa = \eta_{xx}/(1+\eta_x^2)^{3/2}$ represents the interface curvature. The kinematic boundary condition becomes

$$\frac{\partial \eta}{\partial t} + \frac{\partial \phi_i}{\partial x}\frac{\partial \eta}{\partial x} = \frac{\partial \phi_i}{\partial y}, \tag{2.9}$$

and the impermeable condition becomes

$$\frac{\partial \phi_i}{\partial y} = 0. \tag{2.10}$$

These equations form a complete mathematical formulation for the two-layer interfacial wave motion in two dimensions.

In the following chapters, we will focus on traveling waves that move at constant speed c and have permanent profile. To simplify the mathematical description, we choose a moving frame of reference where the waves become steady. As a result, all time-derivative terms in (2.6) to (2.10) vanish and a background flow with a uniform speed $-c$ is superposed to the original velocity field. This gives rise to a change of potential functions

$$\phi_i \to \phi_i - cx, \tag{2.11}$$

Hereafter, we assume that all interfacial waves are calculated in such a moving frame of reference.

2.2 Dispersion relation

Before going to fully nonlinear calculations, it turns out to be convenient to calculate the linear solution of equations (2.6) to (2.10) and derive the dispersion relation. Assuming that the amplitude of interfacial waves is small, we can write the unknowns in the form of normal mode

$$\begin{pmatrix} \eta \\ \phi_1 \\ \phi_2 \end{pmatrix} = \delta \mathrm{e}^{\mathrm{i}kx} \begin{pmatrix} \widehat{\eta} \\ \cosh(k(y+h_1))\widehat{\phi_1} \\ \cosh(k(y-h_2))\widehat{\phi_2} \end{pmatrix}, \tag{2.12}$$

where $\delta \ll 1$ is a small parameter, k is the wave number, $\widehat{\eta}$, $\widehat{\phi_1}$ and $\widehat{\phi_2}$ are unknown constants. Note that the Laplace equation and the impermeable condition have already been satisfied. In the moving frame of reference, we can linearize the kinematic boundary condition and dynamic boundary condition at the unperturbed water level $y = 0$

$$c\frac{\partial \eta}{\partial x} + \frac{\partial \phi_1}{\partial y} = 0, \tag{2.13}$$

$$c\frac{\partial \eta}{\partial x} + \frac{\partial \phi_2}{\partial y} = 0, \tag{2.14}$$

$$-c\left(\rho_1\frac{\partial\phi_1}{\partial x}-\rho_2\frac{\partial\phi_2}{\partial x}\right)+g(\rho_1-\rho_2)\eta-\sigma\frac{\partial^2\eta}{\partial x^2}=0. \tag{2.15}$$

Substituting (2.12), we have linear equations for $\widehat{\eta}$, $\widehat{\phi}_1$ and $\widehat{\phi}_2$

$$\begin{pmatrix} \mathrm{i}kc & k\sinh(kh_1) & 0 \\ \mathrm{i}kc & 0 & -k\sinh(kh_2) \\ (\rho_1-\rho_2)g+\sigma k^2 & -\mathrm{i}\rho_1 kc\cosh(kh_1) & \mathrm{i}\rho_2 kc\cosh(kh_2) \end{pmatrix}\begin{pmatrix}\widehat{\eta}\\ \widehat{\phi}_1\\ \widehat{\phi}_2\end{pmatrix}=\begin{pmatrix}0\\0\\0\end{pmatrix}. \tag{2.16}$$

Since this is a homogeneous equation, the coefficient matrix must have zero determinant to guarantee the existence of non-trivial solutions. This gives rise to a quadratic equation of c. After simplification, we take the positive root and thus obtain the following dispersion relation for two-layer interfacial gravity-capillary waves

$$c=\sqrt{\frac{(\rho_1-\rho_2)g/k+\sigma k}{\rho_1\coth(kh_1)+\rho_2\coth(kh_2)}}. \tag{2.17}$$

We will consider gravity waves ($\sigma=0$) in chapter 3 and 4, and capillary waves ($g=0$) in chapter 5. In chapter 6, we extend the mathematical formulation and dispersion relation to three-layer gravity waves.

In section 2.3 and 2.4, we present the general ideas of the boundary-integral equations and the numerical scheme. More details can be found in the following chapters.

2.3 Boundary-integral equations

To solve the Laplace equation, note that it is equivalent to the incompressible and irrotational conditions

$$\frac{\partial u_i}{\partial x}+\frac{\partial v_i}{\partial y}=0, \tag{2.18}$$

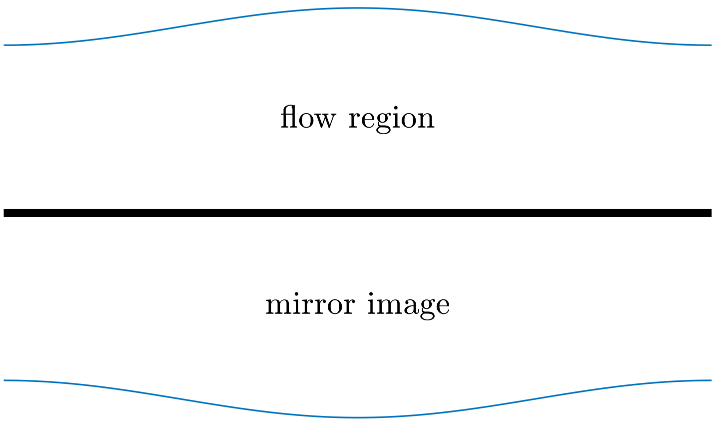

Figure 2.2: Schwarz reflection principle

$$\frac{\partial u_i}{\partial y} - \frac{\partial v_i}{\partial x} = 0, \tag{2.19}$$

which are exactly the Cauchy-Riemann equations. Therefore, we can define complex velocities $w_i = u_i - \mathrm{i}v_i$, which are analytic functions and satisfy the Cauchy's integral formula. We satisfy the impermeable condition (2.4) by applying the Schwarz reflection principle to get rid of the solid wall (see figrue 2.2). As a result, the integral is evaluated on the interface and its mirror image. For periodic waves having wave number k, it is convenient to introduce the following complex variable

$$\zeta = \mathrm{e}^{-\mathrm{i}kz}, \tag{2.20}$$

which maps the physical region in one spatial period to an annular region with wiggly boundaries in the $\zeta-$plane and enables us to rewrite the Cauchy's integral formula after using the Sokhotski–Plemelj theorem

$$w_i(\zeta_0) = \frac{1}{\pi \mathrm{i}} \mathrm{p.v.} \oint_{C_i} \frac{w_i(\zeta)}{\zeta - \zeta_0} \, \mathrm{d}\zeta, \tag{2.21}$$

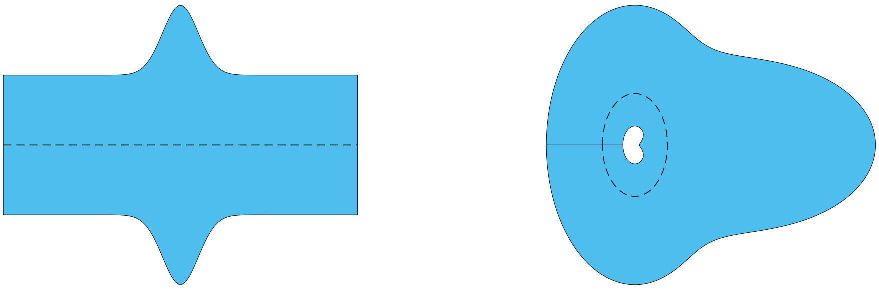

Figure 2.3: Flow region of the lower fluid in one spatial period in the the z-plane (left) and ζ-plane (right).

where C_i denotes the image of the real interface and the mirror interface under the transformation (2.20), ζ_0 is a point on C_i, and p.v. denotes the Cauchy's principal value. The integral is now evaluated on the boundary of an annulus region with wiggly boundaries, as shown in figure 2.3. The two side walls in the z-plane are mapped into the branch cut in the ζ-plane, thus having zero net contribution to the integral. Note that an alternative approach is to apply the Cauchy's integral in the z-plane. We take the deep-water case as example,

$$\begin{aligned} w_i(z_0) &= \frac{1}{\pi \mathrm{i}}\text{p.v.}\int_{S_i} \frac{w_i(z)}{\zeta-\zeta_0}\frac{\mathrm{d}\zeta}{\mathrm{d}z}\,\mathrm{d}z && (2.22)\\ &= -\frac{k}{2\pi}\text{p.v.}\int_{S_i} \frac{2w_i(z)\zeta}{\zeta-\zeta_0}\,\mathrm{d}z && (2.23)\\ &= -\frac{k}{2\pi}\text{p.v.}\int_{S_i} w_i(z)\left(\frac{\zeta+\zeta_0}{\zeta-\zeta_0}+1\right)\mathrm{d}z, && (2.24)\end{aligned}$$

where S_i denotes the interface in one spatial period in the z-plane. Since w_i is assumed a periodic function, we have

$$\begin{aligned} w_i(z_0) &= -\frac{k}{2\pi}\text{p.v.}\int_{S_i} w_i(z)\frac{\zeta+\zeta_0}{\zeta-\zeta_0}\,\mathrm{d}z && (2.25)\\ &= -\frac{k}{2\pi}\text{p.v.}\int_{S_i} w_i(z)\frac{\mathrm{e}^{-\mathrm{i}kz}+\mathrm{e}^{-\mathrm{i}kz_0}}{\mathrm{e}^{-\mathrm{i}kz}-\mathrm{e}^{-\mathrm{i}kz_0}}\,\mathrm{d}z && (2.26)\\ &= -\frac{k}{2\pi}\text{p.v.}\int_{S_i} w_i(z)\frac{\mathrm{e}^{-\mathrm{i}k(z-z_0)/2}+\mathrm{e}^{\mathrm{i}k(z-z_0)/2}}{\mathrm{e}^{-\mathrm{i}k(z-z_0)/2}-\mathrm{e}^{\mathrm{i}k(z-z_0)/2}}\,\mathrm{d}z && (2.27)\\ &= \frac{k}{2\pi \mathrm{i}}\text{p.v.}\int_{S_i} w_i(z)\cot(k(z-z_0)/2)\,\mathrm{d}z. && (2.28)\end{aligned}$$

In the rest part of the thesis, however, we continue to apply equation (2.21). Since the interface becomes a streamline for travelling waves, the velocity vector $\boldsymbol{u}_i$ must be tangent to the interface. Therefore, the complex velocity can be expressed as

$$w_i = q_i \mathrm{e}^{-\mathrm{i}\theta}, \tag{2.29}$$

where q_i denotes the tangential component of velocity vector $\boldsymbol{u}_i$ on the interface, and θ is the tangent angle of the interface. On the other hand, using the physical arclength s of the interface as a variable, we have the following relation

$$\frac{\mathrm{d}z}{\mathrm{d}s} = \mathrm{e}^{\mathrm{i}\theta}. \tag{2.30}$$

As a result, we have

$$w_i \, \mathrm{d}\zeta = q_i \mathrm{e}^{-\mathrm{i}\theta} \frac{\mathrm{d}\zeta}{\mathrm{d}z} \frac{\mathrm{d}z}{\mathrm{d}s} \, \mathrm{d}s = -\mathrm{i}k q_i \, \zeta \, \mathrm{d}s. \tag{2.31}$$

The purpose of using the physical arclength is to guarantee a uniform distribution of the mesh points and achieve a good resolution. Ultimately, (2.21) becomes

$$q_i(s_0)\mathrm{e}^{-\mathrm{i}\theta(s_0)} + \frac{k}{\pi}\mathrm{p.v.} \oint_{C_i} \frac{q_i(s)}{1 - \zeta(s_0)/\zeta(s)} \, \mathrm{d}s = 0. \tag{2.32}$$

Equation (2.32) will be extensively used for numerical calculation in chapter 4 to chapter 6.

2.4 Newton's method and Newton-Krylov method

In the subsequent chapters, we assume that the traveling waves possess an even-symmetry property. In other words, the wave profiles remain unchanged when subjected to a reflection operation with respect to a vertical axis passing through a crest or a trough. To obtain such solutions, we introduce a set of uniform grid points for the arclength variable

$$s_n = \frac{(n-1)S}{N-1}, \qquad n = 1, 2, \cdots, N, \tag{2.33}$$

where S is either the total arclength in one spatial period for periodic waves, or a large enough number for solitary waves. Since the integral equations have singularity when $s = s_0$, we also introduce another set of grid points

$$s_n^m = \frac{s_n + s_{n+1}}{2}, \qquad n = 1, 2, \cdots, N-1. \tag{2.34}$$

The boundary-integral equations are either satisfied on s_n^m by using the values on s_n to calculate the integrals, or vice versa. Consequently, the singular integrals can be numerically computed similar to the regular type of integrals.

To solve nonlinear equations, a traditional approach is to use Newton's method, which has been widely applied in the community of water waves. It offers the advantage of having a quadratic convergence speed and it can be easily extended to high-dimensional vector equations. For N nonlinear equations

$$\boldsymbol{F}(\boldsymbol{x}) = \boldsymbol{0}, \tag{2.35}$$

where $\boldsymbol{x}$ denotes a N-dimensional unknown, Newton's method requires an initial guess $\boldsymbol{x}_0$ and updates its value by iterations

$$\boldsymbol{x}_{n+1} = \boldsymbol{x}_n + \delta\boldsymbol{x}_n. \tag{2.36}$$

The correction $\delta\boldsymbol{x}_n$ is obtained by solving the following system of linear equations

$$\boldsymbol{J}_n \delta\boldsymbol{x}_n = \boldsymbol{r}_n, \tag{2.37}$$

where $\boldsymbol{J}_n = \partial\boldsymbol{F}(\boldsymbol{x}_n)/\partial\boldsymbol{x}_n$ is the Jacobian matrix, and $\boldsymbol{r}_n = -\boldsymbol{F}(\boldsymbol{x}_n)$ is the residual. A severe drawback of this approach is that one has to calculate the $N \times N$ Jacobian matrix and renew it at each iteration step. For nonlinear systems involving boundary integrals or non-analytical operations, the Jacobian matrix is usually too difficult to calculate analytically. Instead, it can be numerically approximated by using the finite difference method. However, the corresponding time cost increases significantly as N becomes large, making the classical Newton's method inconvenient to be applied in large-scale computations. In recent decades, the Newton-Krylov method became popular in the field of computational physics and has been gradually employed to water waves [66, 75]. This method does not require to construct the Jacobian matrix, and thus has a much smaller time cost than Newton's method. The genius of Newton-Krylov method is reflected in the following aspects

- One does not need to solve (2.37) exactly because $\delta\boldsymbol{x}_n$ only provides an approximate direction to update $\boldsymbol{x}_n$. This is the underlying idea of the so-called "inexact Newton's method".

- One can search for the approximate solution of (2.37) from its Krylov subspace $\mathcal{K}_m$. A Krylov subspace of a linear equation $\boldsymbol{J}_n \delta\boldsymbol{x}_n = \boldsymbol{r}_n$ is defined as

$$\mathcal{K}_m = \operatorname{span}\{\boldsymbol{r}_n, \boldsymbol{J}_n\boldsymbol{r}_n, \boldsymbol{J}_n^2\boldsymbol{r}_n, \cdots, \boldsymbol{J}_n^m\boldsymbol{r}_n\}. \tag{2.38}$$

Usually, an accurate enough solution can be constructed when $m \ll N$. For comparison, directly solving (2.37) is equivalent to searching for a solution in the N-dimensional vector space with the standard basis $\{\mathbf{e}_1, \mathbf{e}_2, \cdots, \mathbf{e}_N\}$. To construct the Krylov subspace, one only needs to calculate the matrix-vector product. From definition,

$$\boldsymbol{J}_n \boldsymbol{r}_n \approx \frac{\boldsymbol{F}(\boldsymbol{x}_n + \epsilon \boldsymbol{r}_n) - \boldsymbol{F}(\boldsymbol{x}_n)}{\epsilon}, \tag{2.39}$$

where $\epsilon \ll 1$ is a small constant. Therefore, one can build the Krylov subspace without calculating the Jacobian matrix.

In numerical calculations, the Krylov subspace is usually constructed using the "Arnoldi iteration" instead of the successive power method [74]. A Gram-Schmidt process is applied to find a set of orthonormal basis of the Krylov subspace. For example, the first two orthonormal vectors are calculated

(1). $\boldsymbol{q}_1 = \boldsymbol{r}_n / \|\boldsymbol{r}_n\|$;

(2). $\widetilde{\boldsymbol{q}}_2 = \boldsymbol{J}_n \boldsymbol{q}_1 - \boldsymbol{q}_1^* \cdot (\boldsymbol{J}_n \boldsymbol{q}_1) \boldsymbol{q}_1$, then $\boldsymbol{q}_2 = \widetilde{\boldsymbol{q}}_2 / \|\widetilde{\boldsymbol{q}}_2\|$.

Similarly, one can calculate other orthonormal vectors. This process is equivalent to

$$\boldsymbol{J}_n \boldsymbol{Q}_m = \boldsymbol{Q}_{m+1} \boldsymbol{H}_m, \tag{2.40}$$

where $\boldsymbol{Q}_m = [\boldsymbol{q}_1; \boldsymbol{q}_2; \cdots; \boldsymbol{q}_m]$ is an orthogonal matrix, and $\boldsymbol{H}_m$ is a $(m+1) \times m$ upper Hessenberg matrix. Therefore, the equation (2.37) is transformed to

$$\boldsymbol{H}_m \cdot (\boldsymbol{Q}_m^* \delta \boldsymbol{x}_n) = \boldsymbol{Q}_{m+1}^* \boldsymbol{r}_n, \tag{2.41}$$

which can be solved quickly by the least square method. This is an essential idea of the "Generalized minimum residual method" (GMRES).

In addition, a preconditioning matrix $\boldsymbol{P}$ is usually needed for the GMRES to work effectively. The preconditioning matrix is an approximation of the Jacobian matrix $\boldsymbol{J}_n$ to cluster its eigenvalues. In our calculation, we use a matrix, which equals to the real Jacobian except those derivatives directly related to the boundary-integral equations, as the preconditioning matrix. For example, (2.32) is a linear equation for $q_i(s)$, therefore, the corresponding derivative is trivial to calculate. However, it is a highly nonlinear equation for $\theta(s)$. As a result, when we calculate the corresponding elements of the preconditioning matrix, we only consider the derivatives due to the term $\mathrm{e}^{-\mathrm{i}\theta(s)}$. It turns out, the resulting preconditioning matrix works pretty well. Using the matrix $\boldsymbol{P}$, the linear equation (2.37) becomes

$$(\boldsymbol{J}_n \cdot \boldsymbol{P}^{-1})\delta \boldsymbol{y}_n = \boldsymbol{r}_n, \tag{2.42}$$

$$\delta \boldsymbol{x}_n = \boldsymbol{P}^{-1}\delta \boldsymbol{y}_n. \tag{2.43}$$

In summary, the Newton-Krylov method consists of an outer iteration to update $\boldsymbol{x}_n$ and an inner iteration to obtain the correction vector $\delta \boldsymbol{x}_n$ approximately. In our computation, we set a maximum value N_{max} to restrict the number of inner iteration. When it terminates, $\delta \boldsymbol{x}_n$ is passed to the outer iteration to check whether the convergence condition is satisfied. Based on our numerical experiments, N_{max} is usually set to 10. When solutions become highly nonlinear, N_{max} needs to be gradually increased but without exceeding 40. Increasing the value of N_{max} too much can cause convergence failure.

Chapter 3

Two-layer interfacial gravity solitary waves

In the following two chapters, we will consider the two-layer interfacial gravity waves. In this chapter, we will focus on the solitary waves and its limiting configuration, as shown in figure 3.1. The results of this chapter can be found in Guan et al. [37]

3.1 Introduction

It was conjectured by Stokes that for two-dimensional surface gravity waves in deep water, there exists a family of periodic travelling waves that terminates at an 'extreme wave' as it reaches the maximum amplitude. Such limiting configuration termed the Stokes highest wave, can be characterised by a stagnation point at the crest and an enclosed angle of 120°. The existence of the Stokes highest wave was extensively studied by a variety of authors from asymptotic and numerical perspectives [39, 52, 71, 79, 82], and ultimately proved rigorously by Amick et al. [4]. They also pointed out that Stokes' conjecture holds regardless of wavelength and water depth, and in particular, in the limit of infinite wavelength, the extreme solitary wave features the same limiting crest angle. Yamada [83] is the first known author for numerically solving the limiting solitary waves (see [61] for a detailed description of Yamada's method). Lenau [49] used a series truncation method to compute the same wave. Hunter and Vanden-Broeck [43] improved Lenau's results.

For waves between two homogeneous fluids, the sharp crest of 120° cannot serve as the limiting configuration of the interface, since it would result in infinite velocity in the upper fluid [56]. Attempts to understand the limiting profile of interfacial periodic waves were made by Saffman and Yuen [70], Meiron and Saffman [56], and Turner and Vanden-Broeck [76], who numerically discovered the overhanging structure (i.e., multivalued wave profiles). Meiron and Saffman [56] further asserted that the related limiting profile would become self-intersecting. Grimshaw and Pullin [30] obtained the (almost) self-intersecting solutions when the upper fluid is of infinite depth. They conjectured that a possible extreme profile features a stagnant fluid bubble on top of a 120° angle. Recently, Maklakov and Sharipov [55] conducted a thorough numerical study on the almost limiting configuration between semi-infinite fluid layers. They obtained highly accurate solutions, providing reliable evidence for the extreme profile predicted by Grimshaw and Pullin. Maklakov [54] discussed the transition from interfacial waves to surface waves when the density ratio tends to zero. For interfacial solitary waves, Amick and Turner [5] proved that a possible extreme configuration is an internal front developed from flattening and unlimited broadening of the solitary pulse as the wave speed approaches a limiting value. This theoretical result was verified later by several numerical computations [29, 69, 77]. However, Amick and Turner [5] also showed that the interface could develop a vertical tangent indicating the existence of multi-valued solutions, thus provided another possibility. Pullin and Grimshaw [67] computed the interfacial solitary waves with an overhanging structure and suggested the existence of a self-intersecting profile. However, they could not obtain overhanging waves when the density ratio $R = \rho_2/\rho_1$

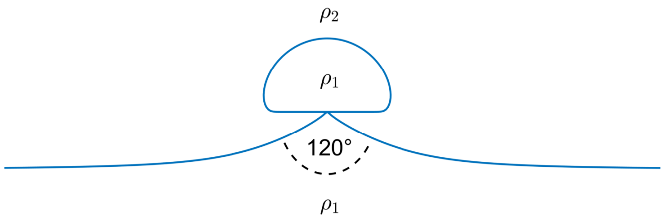

Figure 3.1: A possible limiting configuration for overhanging interfacial solitary waves: a sharp 120° angle with a closed fluid bubble on top of it.

(ρ_1 and ρ_2 are the densities of the lower and upper fluids) is smaller than 0.0256, which was explained by a rapid shrinking of the overhanging structure when the density ratio is small and is further decreased, and therefore more grid points are required to capture overhanging solutions.

In this chapter, we consider interfacial solitary waves between two fluids with finite depths. A boundary integral equation method is used to calculate overhanging solutions and the results of Pullin and Grimshaw [67] are extended to very small density ratios. Based on numerical results and local analysis, we suggest a possible limiting configuration featuring a 120° angle-bubble structure, akin to the periodic case (see figure 3.1). A reduced model, which replaces the curved angle with two straight rigid walls intersecting at the bottom of the fluid bubble, is proposed and numerically solved using a series truncation method. It turns out that the simplified model provides a good local approximation for the cases of a small density ratio when the upper layer is deep enough. The reduced model can also be applied to periodic interfacial waves due to its local nature.

3.2 Mathematical formulation

We consider a two-dimensional solitary wave travelling at speed c between two incompressible and inviscid fluids, bounded above and below by horizontal solid walls. In the moving frame of reference, we set the $x-$axis parallel to the rigid walls and choose the level $y = 0$ as the undisturbed level of the interface at infinity. As stated in the chapter 2, we confine our attention to symmetric waves with the crest on the $y-$axis. Gravity is assumed to act in the negative $y-$direction. We denote by h_i and ρ_i $(i = 1, 2)$ the depth and density in each fluid layer, where subscripts 1 and 2 refer to fluid properties associated with the lower and upper fluid layers, respectively. To perform nondimensionalization, velocities, lengths and densities are measured in scalings of c, h_1 and ρ_1. The motion of each fluid is assumed to be irrotational, thus the velocity potentials ϕ_1 and ϕ_2 satisfy the Laplace equation

$$\phi_{1,xx} + \phi_{1,yy} = 0\,, \qquad \text{for} \quad -1 < y < \eta, \tag{3.1}$$

$$\phi_{2,xx} + \phi_{2,yy} = 0\,, \qquad \text{for} \quad \eta < y < h, \tag{3.2}$$

where η denotes the interfacial displacement and $h = h_2/h_1$ is the depth ratio. On the interface, we have the kinematic boundary conditions

$$\phi_{1,y} - \phi_{1,x}\eta_x = 0, \qquad \text{at} \quad y = \eta, \tag{3.3}$$

$$\phi_{2,y} - \phi_{2,x}\eta_x = 0, \qquad \text{at} \quad y = \eta. \tag{3.4}$$

Using the balance condition of the normal stress (2.8), we get the dynamic boundary condition

$$R|\nabla\phi_2|^2 - |\nabla\phi_1|^2 + \frac{2(R-1)}{F^2}\eta = R - 1\,, \qquad \text{at} \quad y = \eta, \tag{3.5}$$

where $R = \rho_2/\rho_1 < 1$ for a density-stable configuration, $F = c/\sqrt{gh_1}$ is the Froude number, and g is the acceleration due to gravity. Note that the term $R - 1$ on the right-hand side is the Bernoulli constant which can be determined by imposing conditions at infinity

$$\eta \to 0, \qquad \text{as} \quad |x| \to \infty \tag{3.6}$$

$$\phi_{i,x} \to -1, \qquad \text{as} \quad |x| \to \infty \tag{3.7}$$

$$\phi_{i,y} \to 0, \qquad \text{as} \quad |x| \to \infty. \tag{3.8}$$

The boundary conditions at the solid walls read

$$\phi_{1,y} = 0\,, \quad \text{at} \quad y = -1 \tag{3.9}$$

$$\phi_{2,y} = 0\,, \quad \text{at} \quad y = h\,. \tag{3.10}$$

3.3 Numerical method and results

For solitary waves, we write the Cauchy's integral formula in the physical plane

$$w_i(z_0) + 1 = \frac{1}{\mathrm{i}\pi} \text{p.v.} \oint_{C_i} \frac{w_i(z) + 1}{z - z_0}\, \mathrm{d}z\,, \tag{3.11}$$

where $z = x + \mathrm{i}\eta$ is the complex coordinate of the interface, $w_i = \phi_x - \mathrm{i}\phi_y = u_i - \mathrm{i}v_i$ is the complex velocity, and C_i stands for the boundary of the considered fluid domain. We parameterise the interface by arclength $s \in (-\infty, \infty)$ and let $s = 0$ at $x = 0$. Simplifying the Cauchy's integral and taking its real part, we have

$$\begin{aligned}
&\pi[u_1(s_0) + 1] \\
&= \int_0^\infty \frac{[(u_1(s) + 1)x'(s) + v_1(s)\eta'(s)][2 + \eta(s) + \eta(s_0)] - \eta'(s)[x(s) - x(s_0)]}{[x(s) - x(s_0)]^2 + [2 + \eta(s) + \eta(s_0)]^2}\, \mathrm{d}s \\
&+ \int_0^\infty \frac{[(u_1(s) + 1)x'(s) + v_1(s)\eta'(s)][2 + \eta(s) + \eta(s_0)] - \eta'(s)[x(s) + x(s_0)]}{[x(s) + x(s_0)]^2 + [2 + \eta(s) + \eta(s_0)]^2}\, \mathrm{d}s \\
&+ \int_0^\infty \frac{[(u_1(s) + 1)x'(s) + v_1(s)\eta'(s)][\eta(s) - \eta(s_0)] - \eta'(s)[x(s) - x(s_0)]}{[x(s) - x(s_0)]^2 + [\eta(s) - \eta(s_0)]^2}\, \mathrm{d}s \\
&+ \int_0^\infty \frac{[(u_1(s) + 1)x'(s) + v_1(s)\eta'(s)][\eta(s) - \eta(s_0)] - \eta'(s)[x(s) + x(s_0)]}{[x(s) + x(s_0)]^2 + [\eta(s) - \eta(s_0)]^2}\, \mathrm{d}s\,,
\end{aligned} \tag{3.12}$$

$$
\begin{aligned}
&\pi[u_2(s_0)+1]\\
&=\int_0^\infty \frac{[(u_2(s)+1)x'(s)+v_2(s)\eta'(s)][2h-\eta(s)-\eta(s_0)]+\eta'(s)[x(s)-x(s_0))]}{[x(s)-x(s_0)]^2+[2h-\eta(s)-\eta(s_0)]^2}\,\mathrm{d}s\\
&+\int_0^\infty \frac{[(u_2(s)+1)x'(s)+v_2(s)\eta'(s)][2h-\eta(s)-\eta(s_0)]+\eta'(s)[x(s)+x(s_0))]}{[x(s)+x(s_0)]^2+[2h-\eta(s)-\eta(s_0)]^2}\,\mathrm{d}s\\
&-\int_0^\infty \frac{[(u_2(s)+1)x'(s)+v_2(s)\eta'(s)][\eta(s)-\eta(s_0)]-\eta'(s)[x(s)-x(s_0)]}{[x(s)-x(s_0)]^2+[\eta(s)-\eta(s_0)]^2}\,\mathrm{d}s\\
&-\int_0^\infty \frac{[(u_2(s)+1)x'(s)+v_2(s)\eta'(s)][\eta(s)-\eta(s_0)]-\eta'(s)[x(s)+x(s_0)]}{[x(s)+x(s_0)]^2+[\eta(s)-\eta(s_0)]^2}\,\mathrm{d}s\,, \qquad (3.13)
\end{aligned}
$$

where the Schwarz reflection principle (see figure 2.2) and the symmetry of the interface with respect to the $y-$axis are used. To perform numerical computation, (3.12) and (3.13) are calculated over a finite interval $[0, S]$ for the physical arclength s, where S is large enough to approach a uniform flow state in the far field. Two sets of mesh points

$$s_n = \frac{(n-1)S}{N-1}\,, \quad n = 1, 2, \ldots, N\,, \qquad (3.14)$$

$$s_n^m = \frac{s_n + s_{n+1}}{2}\,, \quad n = 1, 2, \ldots, N-1\,, \qquad (3.15)$$

are introduced. $2N-2$ algebraic equations can be obtained by evaluating the integrals at s_n^m using the trapezoid rule. Together with the kinematic boundary conditions (3.3) and (3.4), and the dynamic boundary condition (3.5), as well as the arc length equation

$$x'^2(s) + \eta'^2(s) = 1\,, \qquad (3.16)$$

are evaluated at s_n, we have $6N-2$ algebraic equations. Since there are $6N+1$ unknowns, namely $x'(s_n)$, $\eta'(s_n)$, $u_1(s_n)$, $v_1(s_n)$, $u_2(s_n)$, $v_2(s_n)$ $(n = 1, 2, \cdots, N)$ and F (for a given wave height H), three additional equations are needed to close the system:

$$u_1(S) = -1, \qquad (3.17)$$

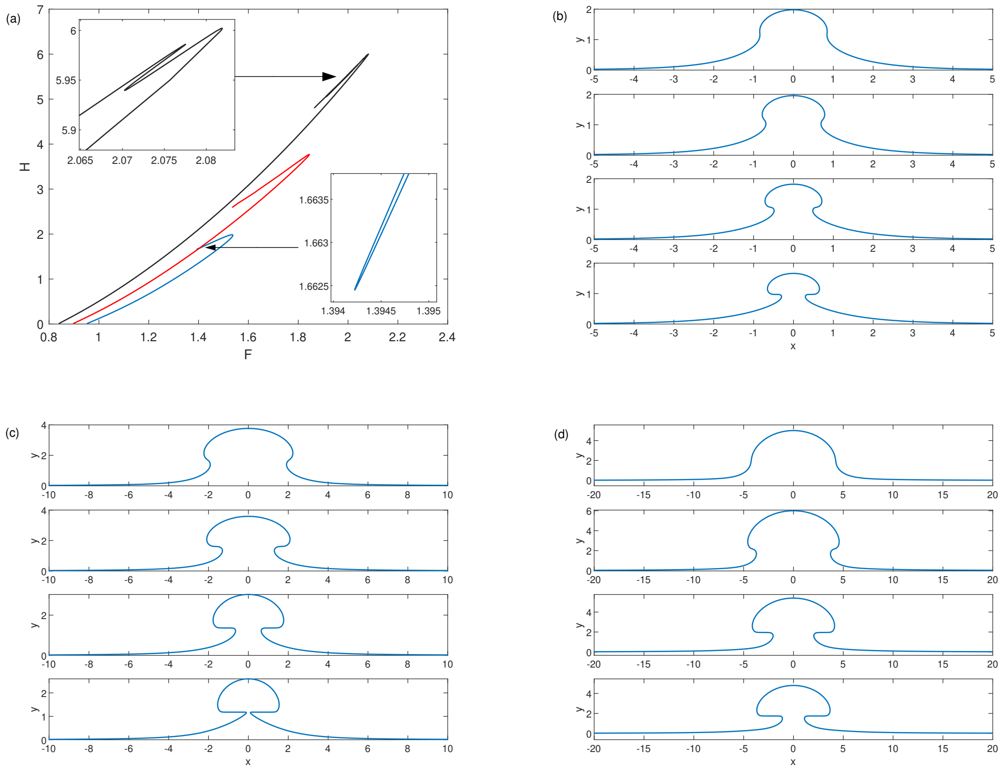

Figure 3.2: (a) Speed-amplitude bifurcation curves for $h = 80$ and $R = 0.1$ (blue), $R = 0.2$ (red), $R = 0.3$ (dark). (b-d) Typical overhanging profiles following the bifurcations for $R = 0.1$, 0.2, 0.3 respectively.

$$\eta'(0) = 0, \tag{3.18}$$

$$\eta(0) = H\,. \tag{3.19}$$

The unknowns at s_n^m can be obtained by means of a four-point interpolation formula. For fixed values of R and h, we calculate solitary waves via the Newton-Krylov method as stated in section 2.4. The initial guess for iteration is chosen to be a set of small-amplitude Gaussian profiles. The iteration process is repeated until the maximum residual error is less than 10^{-8}. We slowly change the value of H (or F) and use the known solutions as the initial guess, thus solution branches can be systematically explored by continuation method.

Numerical results indicate that unlimited broadening of the central core of solitary waves that ultimately turn into internal fronts is likely to occur for small h [77]. In order to obtain overhanging solutions, we choose large values for h, say $h = 80$, in the subsequent computations. Three speed-amplitude bifurcation curves are shown in figure 3.2(a) for the density ratios $R = 0.1$, 0.2, 0.3. Accordingly, the numerical calculations are performed with $S = 40$, 50, 100 and $N = 1200$, 800, 500. Some typical wave profiles are plotted in figure 3.2(b,c,d). In general, it is found that along the bifurcation curve solitary waves gradually steepen, reach the maximum speed corresponding to the first turning point, and form a mushroom-shaped solitary pulse ultimately. It is observed that multiple turning points of speed may exist on the same branch (see the small box in figure 3.2(a)) where the overhanging structure oscillates between closing and opening before it reaches the limiting configuration, meaning that the waves could become less overhanging after passing through a turning point, or on the contrary. The wave profile in the bottom figure of 3.2(c) is the closest to the proposed limiting configuration shown in figure 3.1 among all the numerical solutions that we obtained. Our numerical results agree well with those found by Pullin and Grimshaw [67] who conjectured that all solitary waves for small density ratios would develop an overhanging structure. Solitary waves with an overhanging structure can also be found for other values of R, and for instance, figure 3.3 shows the numerical results obtained based on two sets of parameters: $(R, S, N) = (0.01, 8, 2000)$ and $(0.6, 200, 290)$. It is noted that solutions for $R = 0.01$ extend the result of [67] since they could not get overhanging profiles for $R < 0.0256$ due to numerical difficulties. As R is gradually increased, solitary waves have larger length scale. The numerical calculation thus becomes harder, especially near the first bifurcation turning point.

Based on the aforementioned numerical evidence, it is reasonable to conjecture that the limiting configuration is a self-intersecting interface consisting of a sharp angle and a closed fluid bubble as shown in figure 3.1. To verify this assertion, we plot the velocity magnitude distributions (i.e. $u_{1,2}^2 + v_{1,2}^2$) at the interface in figure

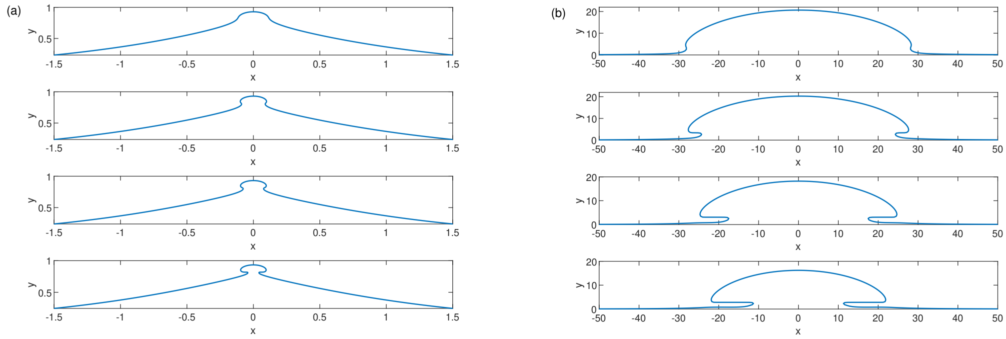

Figure 3.3: Overhanging waves for $h = 80$ and (a) $R = 0.01$, (b) $R = 0.6$.

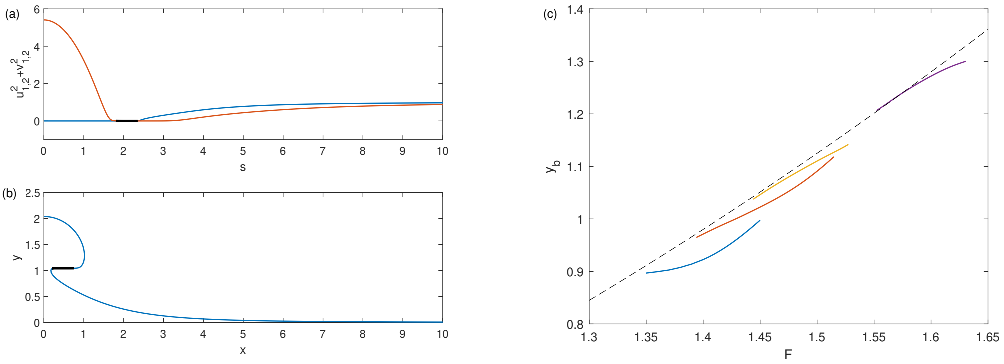

Figure 3.4: (a) Interfacial velocity magnitude of the upper fluid (red) and lower fluid (blue) for $R = 0.15$ and $h = 80$. The segment on which $u_{1,2}^2 + v_{1,2}^2 < 0.005$ is labeled by the black thick line. (b) Wave profile associated with (a), and the black part of the interface corresponds to $u_{1,2}^2 + v_{1,2}^2 < 0.005$. (c) Numerical relations between y_b and F for $R = 0.08$ (blue), $R = 0.1$ (red), $R = 0.15$ (yellow), and $R = 0.2$ (purple), together with the theoretical prediction $y_0 = F^2/2$ (dashed line). y_b denotes the vertical coordinate of the bubble bottom, and y_0 is the theoretical vertical coordinate of the stagnation point.

3.4(a) for $R = 0.15$ and $h = 80$. It is clear that there are two segments where velocities above or below the interface are almost zero. The common segment on which $u_{1,2}^2 + v_{1,2}^2 < 0.005$ is labeled by a thick black line in (a) and correspondingly highlighted on the wave profile in (b). Consequently, for the limiting configuration shown in figure 3.1, if it exists, the fluid inside the bubble should be stationary. Otherwise there must be closed streamlines inside, implying the flows are rotational. Based on a similar argument of the Stokes highest wave, the sharp corner attached to the fluid bubble should be of an interior angle of 120° with the vertex being a stagnation point. On the other hand, Bernoulli's equation at the stagnation point implies $y_0 = F^2/2$ for all density ratios, where y_0 is the vertical coordinate of the vertex. The theoretical prediction $y_0 = F^2/2$ is plotted as the dashed line in figure 3.4(c). Typical numerical values for $y_b(F)$ are shown in the same figure as solid lines, where y_b is the vertical coordinate of the flat bottom of the fluid bubble, namely the part labeled as black in figure 3.4(b). The four curves correspond to $R = 0.08, 0.1, 0.15, 0.2$.

3.4 A simplified model

Although the almost self-intersecting solutions can be obtained by the boundary integral equation method, the appearance of the singularity, i.e. the 120° angle, is a formidable difficulty to overcome. As one can see from figures 3.2 and 3.3, the overhanging structure is fully localised and shrinks rapidly when the value of R is decreased and, furthermore, the local structure beneath the bubble looks very much like an obtuse angle between two straight lines if the density ratio is small, e.g. $R = 0.01$. Motivated by these observations, we attempt to propose a simplified model to describe the local structure of the limiting configuration for small density ratios.

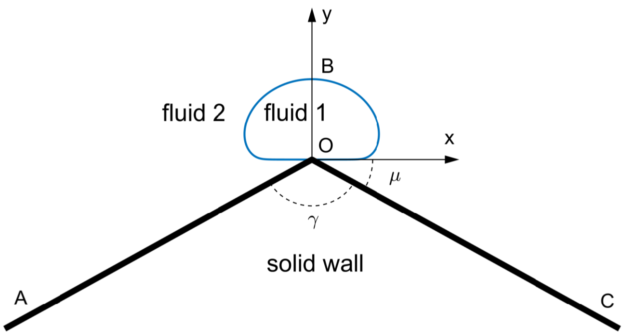

Figure 3.5: A simplified model: two straight solid walls intersect at the origin forming an angle γ and a closed fluid bubble with flat bottom is on top of the angle.

As shown in the simplified model of figure 3.5, the end points A and C, which respectively represent upstream and downstream sides of a flow, are assumed to extend to infinity. The lines OA and OC are supposed to be solid walls where impermeability boundary conditions need to be satisfied. The angle γ is considered to be a parameter, and $\gamma = 2\pi/3$ is the relevant one to model interfacial waves. This is because the flow inside the angle μ approaches a stagnation flow as the point O is approached, where μ is the angle between the solid wall and the bubble bottom (see figure 3.5). The flow of fluid 1 inside the angle γ near the point O reduces then to the local flow considered by Stokes to model surface waves. It then follows that $\gamma = 2\pi/3$. Note that the dynamic boundary condition is not satisfied on the solid walls. This does not affect the local structure of the bubble since it is completely determined by the flow in the corner with angle μ, under the assumption that the bubble is small compared with crest below it. We note that the bottom part of the bubble near O is horizontal, so that $\mu = (\pi - \gamma)/2$. This can be justified by a local analysis of the flow inside the angle μ, a flow bounded above by a free surface and below by a solid wall. It can be shown that the free surface has to be horizontal at O (the only other possibility is the value $\mu = 2\pi/3$ which is not relevant here), and the interested reader is referred to the third chapter of [78] for details.

For the sake of convenience, the origin of the Cartesian coordinate system is set to coincide with the angle vertex O, with the $y-$axis pointing upward, and the summit of the bubble is label as B. Since the fluid inside the bubble is stationary, Bernoulli's equation now reads

$$\frac{\rho_2}{2}\left(u_2^2+v_2^2\right)+(\rho_2-\rho_1)g\eta=0\,. \tag{3.20}$$

Our aim is to find the shape of the fluid bubble as well as the velocity potential ϕ_2. This is a single layer problem since the fluid status beneath the interface is either known or irrelevant.

To solve the problem, we introduce the complex velocity potential $f=\phi_2+\mathrm{i}\psi_2$, with ψ being the stream function. The value of ψ_2 at the interface and along the solid walls as well as $\phi_2(\mathrm{B})$ are set to zero. It is noted the origin is actually the intersection of two walls, and hence we denote by O_- and O_+ the left- and right-hand limits when approaching O along the corresponding walls and let $\Phi=\phi_2(\mathrm{O}_+)=-\phi_2(\mathrm{O}_-)$ due to symmetry. We then non-dimensionalise the system by choosing $\left(\Phi^2/g\right)^{1/3}$ and $\left(\Phi g\right)^{1/3}$ as characteristic length and velocity scales, respectively. Following the work of [25], we solve the problem by using the series truncation method. We introduce a transformation

$$f=-\frac{1+\beta^2}{2\beta}\,, \tag{3.21}$$

which maps the upper half $f-$plane (i.e. the domain occupied by the lighter fluid) onto the upper half unit disk in the complex $\beta-$plane, shown by figure 3.6. The images of A, O_-, B, O_+, C labelled in figure 3.5 are $\beta=0$, 1, i, -1, 0. The complex velocity $w_2=u_2-\mathrm{i}v_2$ is analytic everywhere except at $\beta=0$ and $\beta=\pm1$, where the asymptotic behaviors are

$$w_2\sim\beta^{1-\frac{\gamma}{\pi}}\,,\quad \text{as } \beta\to0\,, \tag{3.22}$$

$$w_2\sim\left(1-\beta^2\right)^{2-\frac{2\mu}{\pi}}\,,\quad \text{as } \beta\to\pm1\,, \tag{3.23}$$

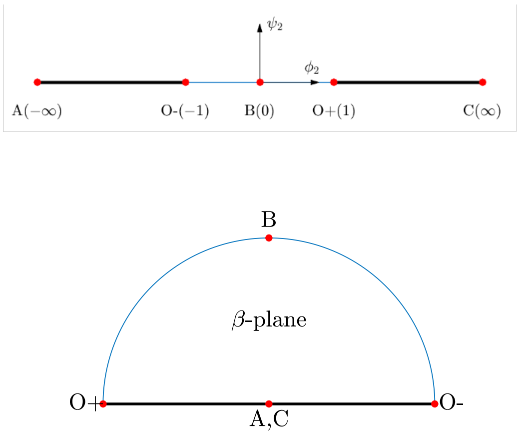

Figure 3.6: Top: Values of ϕ_2 along the solid walls and the surface of the bubble. Bottom: The region above the solid walls and outside the bubble is mapped into the upper semicircle in the β-plane after using (3.21).

with $\mu = (\pi - \gamma)/2$. Therefore, the complex velocity w_2 can be expanded as

$$w_2 = \mathrm{e}^{\mathrm{i}\frac{\gamma-\pi}{2}} \beta^{1-\frac{\gamma}{\pi}} \left(1-\beta^2\right)^{2-\frac{2\mu}{\pi}} \xi \,, \tag{3.24}$$

where ξ is an analytic function inside the upper semicircle. We introduce two real functions τ and ν so that

$$\xi = \mathrm{e}^{\tau - \mathrm{i}\nu}, \tag{3.25}$$

and expand $\tau - \mathrm{i}\nu$ as power series of β

$$\tau - \mathrm{i}\nu = \sum_{n=0}^{\infty} a_n \beta^{2n} = \sum_{n=0}^{\infty} a_n \cos(2n\chi) - \mathrm{i} \sum_{n=1}^{\infty} a_n \sin(2n\chi) \,, \tag{3.26}$$

where the coefficients a_n are real. Note that this means we can perform the Schwarz reflection to continue ξ analytically into the lower unit semicircle. At the interface, $\beta = \mathrm{e}^{\mathrm{i}\chi}$ and $\chi \in [0, \pi]$. Upon noting the identity $x_\phi + \mathrm{i} y_\phi = 1/w_2$, it is easy to verify that

$$y_\phi = \mathrm{e}^{-\tau}\Big(2\sin(\chi)\Big)^{-2+\frac{2\mu}{\pi}} \sin\left[\nu - \left(3 - \tfrac{\gamma}{\pi} - \tfrac{2\mu}{\pi}\right)\left(\chi - \tfrac{\pi}{2}\right)\right] , \qquad (3.27)$$

$$x_\phi = \mathrm{e}^{-\tau}\Big(2\sin(\chi)\Big)^{-2+\frac{2\mu}{\pi}} \cos\left[\nu - \left(3 - \tfrac{\gamma}{\pi} - \tfrac{2\mu}{\pi}\right)\left(\chi - \tfrac{\pi}{2}\right)\right] . \qquad (3.28)$$

Thus Bernoulli's equation becomes

$$\frac{R}{2}\mathrm{e}^{2\tau}\Big(2\sin(\chi)\Big)^{4-\frac{4\mu}{\pi}} + (R-1)\int_0^{\chi} y_\phi \sin(\chi)\mathrm{d}\chi = 0. \qquad (3.29)$$

To solve equation (6.5), the infinite series in (3.26) are truncated at $n = N - 1$ and N collocation points are uniformly distributed on the interval $\left[0, \frac{\pi}{2}\right]$, namely

$$\chi_n = \frac{\pi(n-1)}{2(N-1)}, \qquad n = 1, 2, \cdots, N . \qquad (3.30)$$

Equation (6.5) is then satisfied at the mesh points $\chi_2, \chi_3, \cdots, \chi_N$ with an additional equation

$$\int_0^{\frac{\pi}{2}} x_\phi \sin(\chi)\, \mathrm{d}\chi = 0 , \qquad (3.31)$$

which means that the interface is closed. Finally, this system of N (which is no less than 300 in numerical calculations) nonlinear equations with N unknowns a_0, a_1, $\cdots$, a_{N-1} is solved via Newton's method for a given value of γ. This method of series truncation has been applied successfully to solve many free surface problems (see [78] for details and references).

Case I. $\gamma = 2\pi/3$

Numerical results for $\gamma = 2\pi/3$ (i.e. $\mu = \pi/6$) are shown in figure 3.7. A typical profile and corresponding streamlines are plotted in (a) for $R = 0.1$. From Bernoulli's

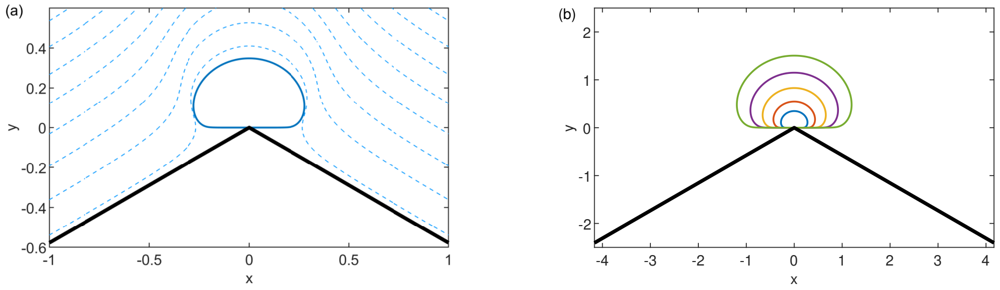

Figure 3.7: (a) Numerical solution of the simplified model for $\gamma = 2\pi/3$ and $\mu = \pi/6$ (solid curve), together with streamlines (dashed curves). (b) Similarity solutions for $R = 0.9$, 0.8, 0.6, 0.3, 0.1 from large to small.

equation

$$R(u_2 u_{2\chi} + v_2 v_{2\chi}) + (R-1)\sin(\chi)\frac{v_2}{u_2^2 + v_2^2} = 0\,, \tag{3.32}$$

which is derived from equation (3.20) by taking the derivative with respect to χ, one can eliminate R by introducing

$$u_2' = \sqrt[3]{\frac{R}{1-R}}\,u_2\,, \qquad v_2' = \sqrt[3]{\frac{R}{1-R}}\,v_2\,. \tag{3.33}$$

This fact immediately suggests that profiles for different values of R are geometrically similar, which is reasonable since no natural length scale appears in the reduced model. To verify this assertion, numerical solutions are plotted in figure 3.7(b) where the profiles from large to small correspond to $R = 0.9$, 0.8, 0.6, 0.3, 0.1 respectively.

Figure 5.11 shows comparisons between solutions of the simplified model and the almost self-intersecting solutions obtained from the boundary integral equation method. The black line represents the assumed 120° angle. To plot these solutions under the same scaling, we enlarge the profiles of the simplified model and then move the profiles vertically so that their top and bottom match the highest point and flat bottom of the bubble structure of the primitive problem. The density ratios from (a) to (d) are 0.01, 0.05, 0.1, 0.2 respectively. It is observed that for a small density ratio, the simplified model provides a good approximation to the almost self-intersecting

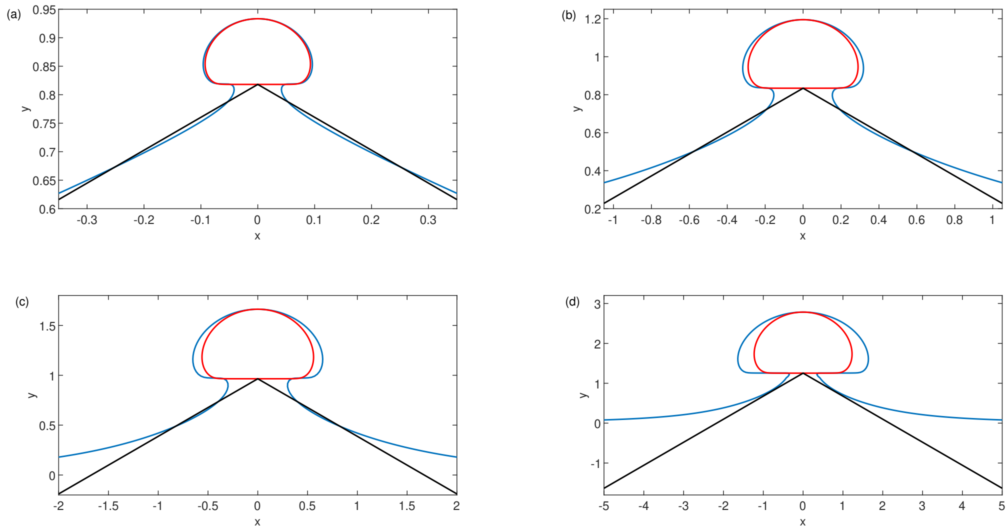

Figure 3.8: Comparisons between the almost self-intersecting solutions (blue curves) and profiles resulting from the simplified model (red curves). The black lines represent solid walls intersecting at a 120° angle. (a) $R = 0.01$, (b) $R = 0.05$, (c) $R = 0.1$, (d) $R = 0.2$.

solution of the primitive equations and further to the limiting configuration shown in figure 3.1, if it exists.

Case II. $\gamma \neq 2\pi/3$

It is natural to ask what happens to the reduced model when $\gamma \neq \frac{2\pi}{3}$. In fact, numerical solutions can be found for arbitrary $\gamma \in [0, \pi]$. Four typical solutions with $R = 0.1$ are shown in figure 3.9.

Two limiting cases, $\gamma = 0$ and $\gamma = \pi$, merit special attention. As can be seen from figure 3.9, the profile becomes more and more circular as the value of γ is decreased. Therefore, one may expect a perfect circular interface to appear when $\gamma = 0$. In fact, it is not difficult to check that $w_2 = \mathrm{i}\beta\,(1-\beta^2)\,a_0$ is an explicit solution of equation (6.48), where $a_0 = \sqrt[3]{(1-R)/4R}$. One can then obtain the parametric form of the interface as

$$x = -\frac{1}{4a_0}\sin(2\chi), \quad y = -\frac{1}{4a_0}\Big(\cos(2\chi) - 1\Big)\,, \tag{3.34}$$

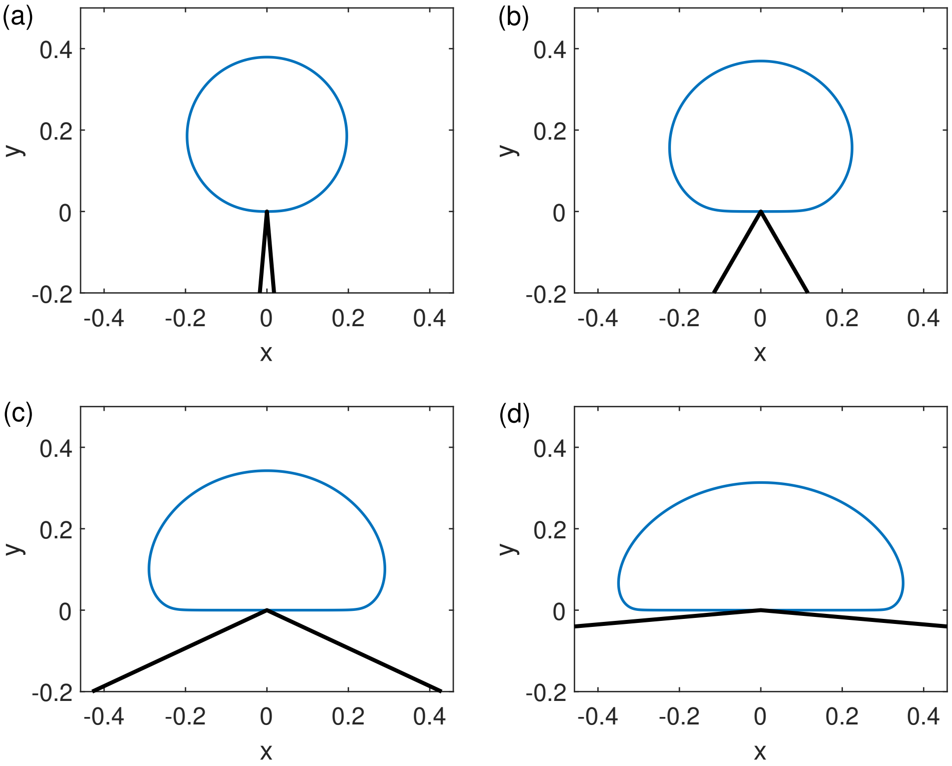

Figure 3.9: Solutions of the simplified model for (a) $\gamma = \frac{\pi}{18}$, (b) $\gamma = \frac{\pi}{3}$, (c) $\gamma = \frac{13\pi}{18}$, (d) $\gamma = \frac{17\pi}{18}$.

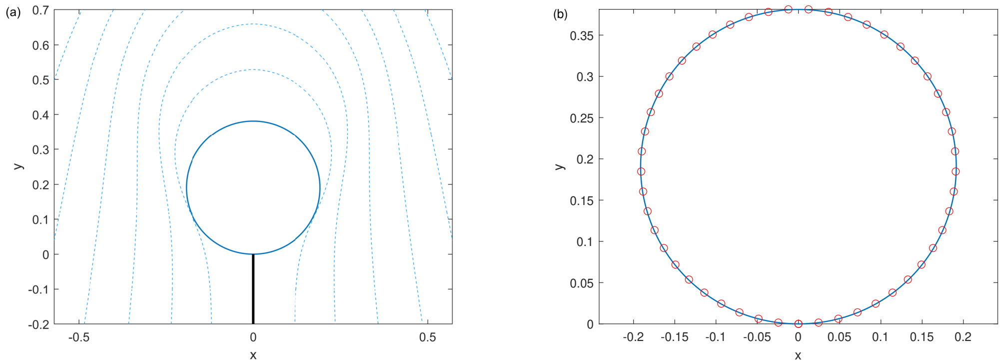

Figure 3.10: (a) Numerical solution for $\gamma = 0$ and $\mu = \frac{\pi}{2}$ (solid curve) and streamlines (dashed curves). (b) Comparison between the numerical solution (solid curve) and theoretical prediction (red circles).

which is a circle with radius $1/4a_0$. The numerical solution for $R = 0.1$ is plotted in figure 3.10, where the profile and streamlines are displayed in (a) while the comparison with the exact solution is in (b). It thus demonstrates the validity of the numerical algorithm.

For the case of $\gamma = \pi$, the bottom of the fluid bubble entirely attaches to the solid wall, therefore the interface should intersect the solid wall with a 120° angle and form a stagnation point according to the local analysis. A typical solution for $R = 0.1$ is shown in figure 3.11 by setting $\mu = 2\pi/3$ and dropping equation (3.31) since the profile is no longer closed at the origin. These solutions describe a still water bubble lying on the flat bottom. Unlike those shown in figure 3.7 which represent the limiting solutions for $R \ll 1$, solution shown in figure 3.11 correspond to another possible limiting configuration of interfacial solitary waves under the Boussinesq limit, i.e. $R \to 1$. Such solutions were found by Pullin and Grimshaw [67] when the upper fluid is infinitely deep. They proposed that in such a scenario solitary waves are unbounded and calculated the limiting configuration by fixing the wave height and gradually decreasing the lower layer thickness to zero. In particular, they concluded that the limiting interface features a half-lens shape with an approximate aspect ratio (i.e. the ratio of width to height) of 4.36, which perfectly agrees with 4.353 resulting from our simplified model. According to equation (3.33), solutions of the simplified model have a spatial scale proportional to $\sqrt[3]{R/(1-R)}$, thus become unbounded when $R \to 1$.

3.5 Conclusions

In conclusion, we have found numerical evidence for a possible limiting configuration of interfacial solitary waves. Overhanging solutions which become almost self-intersecting have been calculated via a boundary integral equation method for

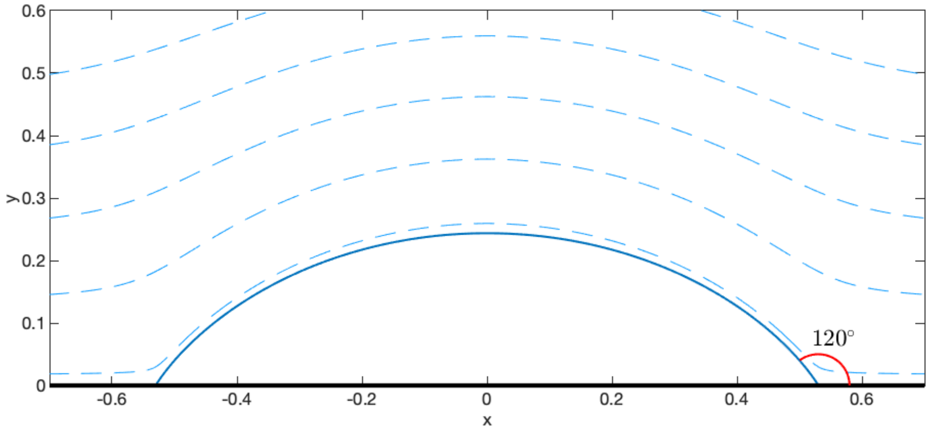

Figure 3.11: Numerical solution for $\gamma = \pi$ and $\mu = \frac{2\pi}{3}$ (solid curve), together with streamlines (dashed curves).

various density ratios, strongly suggesting a limiting configuration characterised by a stagnation point at a 120° angle and a closed fluid bubble on top of the angle (see figure 3.1). A simplified model based on these numerical results has been proposed to study the local structure of these singular solutions. Using a series truncation method, we have found exotic solutions depending on the value of γ, i.e. the angle formed by two intersecting walls. When $\gamma = 2\pi/3$, the simplified model provides a good approximation to those almost self-intersecting solutions for small density ratios. Solutions for other values of γ have also been computed. In particular, we have found an explicit solution featuring a circular profile for $\gamma = 0$, and a solution corresponding to another limiting configuration of interfacial solitary waves for $\gamma = \pi$. Furthermore, it is important to mention that the reduced model can also be applied to periodic interfacial waves due to its local nature. Finally, considering the crest instability of the Stokes highest waves (see detailed numerical investigations in [53]), the Kelvin-Helmholtz instability of interfacial gravity waves [10], and the Rayleigh-Taylor instability due to the mushroom structure, it is very likely that the almost limiting configurations of progressive interfacial waves are unstable. Therefore, the competition mechanism among different instabilities and the time-evolution of the instability are of particular interest which merit further thorough studies. Some progress will be presented in chapter 7.

Chapter 4

Two-layer interfacial gravity periodic waves

In this chapter, we investigate the interfacial gravity traveling-wave solutions in two-layer periodic domain. With a detailed description of the limiting configuration in chapter 3, we concentrate on the bifurcation mechanism of the periodic waves in the current chapter. The results of this chapter can be found in Guan et al. [35].

4.1 Introduction

The singular limiting configuration of interfacial gravity waves (see figure 3.1) were first proposed by Grimshaw and Pullin [30] when studying periodic solutions. They assumed that both fluids have almost equal density and the flows have a constant vorticity ω. They found that the relation between wave amplitude and wave speed shows a good agreement with that of the Stokes highest waves when $\omega \to 0$. Therefore, they conjectured the existence of such limiting configuration that two highest Stokes waves are parallel placed with a half-period shift and their crest pointing oppositely, see figure 4.1(c). When $\omega \neq 0$, they found a mushroom-shape overhanging solution and proposed a second limiting configuration which features a closed bubble of heavier fluid on top a 120° angle, see figure 4.1(a). In addition, some of their numerical results suggested a third limiting configuration as shown in figure 4.1(b). It has a closed bubble of lighter fluid underneath a 120° angle pointing downward, thus can be regarded as a counterpart of the solution shown in figure 4.1(a). For convenience, we shall call these limiting configurations type I limit, type II limit and type III limit, as shown in figure 4.1 from top to bottom, respectively. Although these solutions were obtained under the constant-vorticity assumption, it turns out they also emerge in irrotational flows. This was shown recently by Maklakov and Sharipov [55] who restudied the periodic interfacial gravity waves in the infinite deep water case. They developed a new numerical method based on the piecewise-analytical function theory, which gives highly accurate results and solid numerical evidence of type I limit. Maklakov [54] further illustrated the connection between the Stokes highest waves and type I solution in the limit that upper fluid density tends to zero.

In the present chapter, we study two-dimensional periodic progressive interfacial gravity waves in a two-fluid system with finite depths. The interface is assumed to have a permanent form hence any possible dynamical instabilities would result in distortion are not considered. Using the boundary-integral equations and the Fourier expansion method, we obtain high-accuracy numerical solutions whose agreement with those from [55] is perfect. We find the almost limiting profiles within a variety of parameter ranges and the numerical evidence which support the existence of all three limiting types shown in figure 4.1. Especially, we confirm the assertion of Grimshaw and Pullin [30] on the type III solution in the Boussinesq limit. Suprisingly, we obtain another branch of solutions which bifurcate from a secondary bifurcation point and end up with type I and type II limits. This new branch is observed to separate and form a second bifurcation curve with a size-shrinking tendency and ultimately vanishes when the density ratio is away from 1. We further confirm that

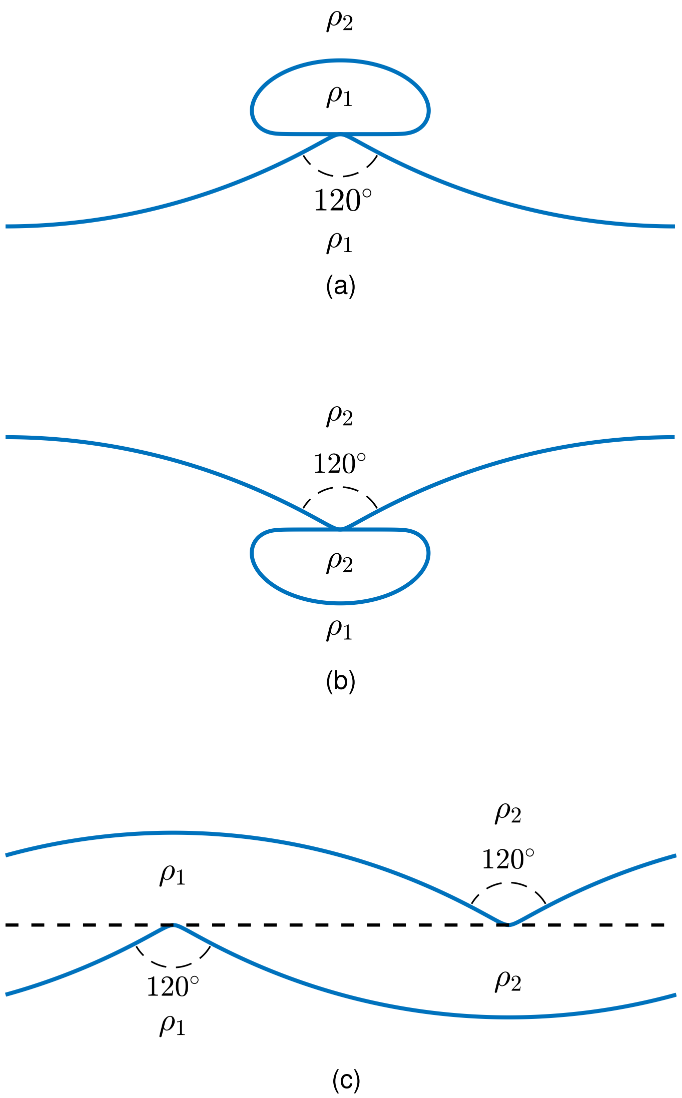

Figure 4.1: Three limiting profiles. (a): type I, (b): type II and (c): type III.

the secondary bifurcation point exists under special parameter choices and all three limiting types coexist. Once the parameter state is away from these special cases, new bifurcation curves separate and gradually shrink to zero.

4.2 Mathematical formulation

Consider two-dimensional periodic interfacial waves propagating at constant speed c with a permanent form between two immiscible fluids that are bounded above and below by horizontal solid walls. The lower fluid and the upper fluid have densities ρ_1, ρ_2, and depths h_1, h_2 which are measured from the undisturbed interface level. In the moving frame of reference, waves are steady and symmetric, as stated in chapter 2. We choose Cartesian coordinates with the $x-$axis on the undisturbed interface level and the $y-$axis on a line of symmetry. The $x-$axis points to the direction of wave propagation and the $y-$axis points from the lower fluid to the upper fluid. The only external force under consideration is gravity which acts in the negative $y-$direction. It is convenient to choose ρ_1, h_1 and c to be the scalings of density, length and velocity. Suppose the motion of each fluid is incompressible, inviscid and irrotational, the velocity potentials ϕ_1 and ϕ_2 satisfy Laplace equation

$$\phi_{1,xx} + \phi_{1,yy} = 0, \qquad \text{for} \quad -1 < y < \eta \tag{4.1}$$

$$\phi_{2,xx} + \phi_{2,yy} = 0, \qquad \text{for} \quad \eta < y < h \tag{4.2}$$

where η denotes the interfacial displacement and $h = h_2/h_1$ is the depth ratio. On the interface, the kinematic and dynamical boundary conditions are expressed as

$$\phi_{1,y} - \phi_{1,x}\eta_x = 0, \qquad \text{at} \quad y = \eta, \tag{4.3}$$

$$\phi_{2,y} - \phi_{2,x}\eta_x = 0, \qquad \text{at} \quad y = \eta, \tag{4.4}$$

$$R|\nabla\phi_2|^2 - |\nabla\phi_2|^2 + \frac{2(R-1)}{F^2}\eta = B, \qquad \text{at} \quad y = \eta, \tag{4.5}$$

where $R = \rho_2/\rho_1 < 1$ is the density ratio, $F = \sqrt{c^2/gh_1}$ is the Froude number and B stands for the unknown Bernoulli constant. Finally, on the solid walls, we have impermeable condition:

$$\phi_{1,y} = 0, \qquad \text{at} \quad y = -1, \tag{4.6}$$

$$\phi_{2,y} = 0, \qquad \text{at} \quad y = h. \tag{4.7}$$

4.3 Numerical methods

4.3.1 Boundary integral equations

Using complex variable $\zeta = \mathrm{e}^{-\mathrm{i}kz}$, where k is the wavenumber of periodic waves and $z = x + \mathrm{i}y$, we write the Cauchy's integral formula in the $\zeta-$plane

$$w_i(\zeta_0) = \frac{1}{\mathrm{i}\pi}\mathrm{p.v.}\oint_{C_i} \frac{w_i(\zeta)}{\zeta - \zeta_0}\,\mathrm{d}\zeta\,, \tag{4.8}$$

where $w_i = \phi_{i,x} - \mathrm{i}\phi_{i,y} = u_i - \mathrm{i}v_i$ is the complex velocity and C_i represents the boundary of the lower layer ($i = 1$) or upper layer ($i = 2$). For travelling waves, velocity vector $\boldsymbol{u}_i$ must be tangential to the interface, thus

$$w_i = q_i \mathrm{e}^{-\mathrm{i}\theta}, \tag{4.9}$$

where θ is the tangent angle of the interface. Cauchy's integral is rewritten as

$$q_i(s_0)\mathrm{e}^{\mathrm{i}\theta(s_0)} + \frac{k}{\pi}\mathrm{p.v.}\oint_{C_i} \frac{q_i(s)}{1 - \zeta(s)/\zeta(s_0)}\,\mathrm{d}s = 0\,, \tag{4.10}$$

where s is the interface arclength. Let $Y_+ = \eta(s_0) + \eta(s)$, $Y_- = \eta(s_0) - \eta(s)$, $X_+ = x(s_0) + x(s)$, and $X_- = x(s_0) - x(s)$. Applying the Schwarz reflection principle (see figure 2.2) for both fluid layers and taking the real part of equations, we obtain two real-valued integral equations

$$\begin{aligned}
&\pi q_1(s_0)x'(s_0)/k = \\
&-\int_0^\alpha \left(\frac{q_1(s)(1-\mathrm{e}^{k(Y_++2)}\cos(kX_-))}{1+\mathrm{e}^{2k(Y_++2)}-2\mathrm{e}^{k(Y_++2)}\cos(kX_-)} - \frac{q_1(s)(1-\mathrm{e}^{kY_-}\cos(kX_-))}{1+\mathrm{e}^{2kY_-}-2\mathrm{e}^{kY_-}\cos(kX_-)} \right) \mathrm{d}s \\
&-\int_0^\alpha \left(\frac{q_1(s)(1-\mathrm{e}^{k(Y_++2)}\cos(kX_+))}{1+\mathrm{e}^{2k(Y_++2)}-2\mathrm{e}^{k(Y_++2)}\cos(kX_+)} - \frac{q_1(s)(1-\mathrm{e}^{kY_-}\cos(kX_+))}{1+\mathrm{e}^{2kY_-}-2\mathrm{e}^{kY_-}\cos(kX_+)} \right) \mathrm{d}s\,,
\end{aligned} \tag{4.11}$$

$$\begin{aligned}
&\pi q_2(s_0)x'(s_0)/k = \\
&-\int_0^\alpha \left(\frac{q_2(s)(1-\mathrm{e}^{kY_-}\cos(kX_-))}{1+\mathrm{e}^{2kY_-}-2\mathrm{e}^{kY_-}\cos(kX_-)} - \frac{q_2(s)(1-\mathrm{e}^{k(Y_+-2h)}\cos(kX_-))}{1+\mathrm{e}^{2k(Y_+-2h)}-2\mathrm{e}^{k(Y_+-2h)}\cos(kX_-)} \right) \mathrm{d}s \\
&-\int_0^\alpha \left(\frac{q_2(s)(1-\mathrm{e}^{kY_-}\cos(kX_+))}{1+\mathrm{e}^{2kY_-}-2\mathrm{e}^{kY_-}\cos(kX_+)} - \frac{q_2(s)(1-\mathrm{e}^{k(Y_+-2h)}\cos(kX_+))}{1+\mathrm{e}^{2k(Y_+-2h)}-2\mathrm{e}^{k(Y_+-2h)}\cos(kX_+)} \right) \mathrm{d}s\,,
\end{aligned} \tag{4.12}$$

where α denotes the total arclength of the interfacial wave in half period and the assumed symmetry property of waves has been used to simplify the equations.

4.3.2 The Fourier method

Due to the periodicity and symmetry of the computed waves, we can express the unknown functions q_1, q_2, x and η as Fourier series. For convenience, we introduce a normalised arclength parameter $\tau = s/\alpha \in [-1, 1]$ and write the Fourier expansions as

$$q_1(\tau) = \sum_{n=0}^{\infty} a_n \cos(n\pi\tau)\,, \tag{4.13}$$

$$q_2(\tau) = \sum_{n=0}^{\infty} b_n \cos(n\pi\tau)\,, \tag{4.14}$$

$$x(\tau) = c_0\tau + \sum_{n=1}^{\infty} \frac{c_n}{n\pi} \sin(n\pi\tau)\,, \tag{4.15}$$

$$\eta(\tau) = d_0 - \sum_{n=1}^{\infty} \frac{d_n}{n\pi} \cos(n\pi\tau)\,. \tag{4.16}$$

Truncating these series after N terms gives $4N$ unknowns, namely a_n, b_n, c_n, and d_n $(n = 0, 1, \cdots, N-1)$. Putting them together with F, B, and α, there are eventually $4N+3$ unknowns to be found. We evaluate (4.11) and (4.12) over the interval $[0,1]$ at N equally spaced mesh points

$$\tau_n = \frac{n-1}{N-1}\,, \quad n = 1, \cdots, N\,.$$

To avoid the singularity in the Cauchy integral formula, we introduce another set of mesh points

$$\tau_n^m = \frac{\tau_n + \tau_{n+1}}{2}\,, \quad n = 1, \cdots, N-1\,,$$

and calculate the integrals by applying the alternative-point trapezoidal/midpoint rule [6]. The Bernoulli equation and the arclength equation become

$$Rq_2^2 - q_1^2 + \frac{2(R-1)\eta}{F^2} = B\,, \tag{4.17}$$

$$x'(\tau)^2 + \eta(\tau)'^2 = \alpha^2\,, \tag{4.18}$$

and are satisfied at the mesh points τ_n $(n = 1, 2, \cdots, N)$. Since the $x-$axis is fixed on the undisturbed interface level, we impose the volume-conservation condition

$$\int_0^1 \eta(\tau)x'(\tau)\,\mathrm{d}\tau = 0 \quad \Rightarrow \quad \sum_{n=1}^{N-1} \frac{c_n d_n}{2\pi n} - c_0 d_0 = 0\,. \tag{4.19}$$

The periodicity in $x-$direction requires

$$x(1) - x(0) = \frac{\pi}{k} \quad \Rightarrow \quad c_0 = \frac{\pi}{k}. \tag{4.20}$$

To close the system, we also need to give a definition of the wave amplitude H

$$H = \eta(0) - \eta(1)\,, \tag{4.21}$$

and prescribe the wave speed, which has been scaled to unity. There are different ways to define it. Following a widely used condition in surface gravity waves, we define the wave speed as the averaged velocity in the lower layer or the upper layer

$$\frac{k}{\pi}\int_0^{\pi/k} u_i(x, y = \text{const.})\,\mathrm{d}x = -1\,. \tag{4.22}$$

The negative sign reflects the fact that the background current is from right to left in the moving frame of reference. (4.22) can be rewritten in terms of q_i by using the Stokes theorem and irrotationality condition

$$\oint_{C_i} \boldsymbol{u}\cdot\boldsymbol{t}\,\mathrm{d}s = \iint_{S_i} \nabla\times\boldsymbol{u}_i = 0, \tag{4.23}$$

where $\boldsymbol{t}$ denotes the unit tangential vector along the boundary C_i, and S_i stands for the region enclosed by C_i. Thus (4.22) can be expressed by integral of q_i evaluated on the interface

$$\frac{\alpha k}{\pi}\int_0^1 q_1(\tau)\,\mathrm{d}\tau = -1 \Rightarrow a_0\alpha = -\frac{\pi}{k}\,. \tag{4.24}$$

$$\frac{\alpha k}{\pi}\int_0^1 q_2(\tau)\,\mathrm{d}\tau = -1 \Rightarrow b_0\alpha = -\frac{\pi}{k}\,. \tag{4.25}$$

Note that there are some extra constraints due to the symmetry of waves

$$x(0) = 0\,, \qquad \eta'(0) = 0\,, \qquad \eta'(1) = 0\,, \tag{4.26}$$

which are automatically satisfied owing to their Fourier representations. Finally, we have $4N + 5$ equations (4.11)–(4.12), (4.17)–(4.21) and (4.24)–(4.25) with only

$4N + 3$ unknowns. Therefore, we choose to drop the equations of (4.11) and (4.12) at the point $\tau = 1$, and perform the Newton-Krylov method to solve the system for given values of R, k, h, and H. The iteration process is repeated until the maximum residual error is less than 10^{-10}. At first glance it seems dangerous to abandon two integral equations. However, our numerical results show that the maximum residual error of these two equations (denoted as δ hereafter) is of the order of 10^{-11} in most cases. Based on our numerical experience, $N = 600$ usually gives accurate enough results and thus is used in most computations. For almost limiting solutions, however, typically 1200 Fourier modes are necessary to maintain appropriate accuracy and to ensure $\delta < 10^{-4}$.

4.4 Numerical Results

4.4.1 Validation

In Table 4.1, we present results for $R = 0.1$ and compare them with the works of Saffman and Yuen [70] and Maklakov and Sharipov [55]. Since their results were obtained in the case when both layers are infinitely deep, we let $h = 1$ and $k \gg 1$ to achieve a good approximation of their results, and after many tests it was found that $k = 100$ is large enough to provide an excellent agreement. Note that these authors used a different length scale, $\sqrt{g/k}$, so their dimensionless wave amplitude reads kH. The dimensionless wave speed defined by Saffman and Yuen (C_s) and Maklakov and Sharipov (C_m) can be expressed as

$$C_s = F\sqrt{k}\sqrt{\frac{1+R}{1-R}}\,, \qquad C_m = F\sqrt{k}\,. \tag{4.27}$$

Increasing N up to 300, we have nine correct decimals in comparison with [55] in most cases except for a few solutions very close to the limiting configuration. Though not

kH	C_s(S&Y)	C_s(M&S)	$C_s(N = 200)$	$C_s(N = 300)$
0.1	1.0010433	1.001043327	1.001043327	1.001043327
0.3	1.0093851	1.009385147	1.009385147	1.009385147
0.5	1.0260381	1.026038075	1.026038075	1.026038075
0.7	1.0509243	1.050924313	1.050924313	1.050924313
0.9	1.0839603	1.083960270	1.083960271	1.083960271
1.10	1.125454	1.125454593	1.125454593	1.125454593
1.20	1.149904	1.149903889	1.149903889	1.149903889
1.30	1.177	1.177754503	1.177754503	1.177754503
1.32	-	1.183901408	1.183901408	1.183901408
1.34	-	1.190327567	1.190327567	1.190327567
1.36	-	1.197125838	1.197125838	1.197125838
1.38	-	1.204514662	1.204514662	1.204514662
1.39	-	1.208645838	1.208645838	1.208645838
1.39	-	1.213326106	1.213326105	1.213326106
1.38	-	1.210675485	1.210675484	1.210675485
1.36	-	1.204401123	1.204401182	1.204401123
1.34	-	1.197369928	1.197369998	1.197369929
1.32	-	1.189740717	1.189740717	1.189740717
1.30	-	1.181506483	1.181506847	1.181506483
1.28	-	1.172510673	1.172523419	1.172510684

Table 4.1: C_s versus kH for $R = 0.1$, $h = 1$, and $k = 100$. The second and third columns are the results of Saffman and Yuen [70] and Maklakov and Sharipov [55], respectively.

explicitly shown in Table 4.1, for most solutions $\delta = O(10^{-11})$, which demonstrates the validity of our numerical method. Even when δ increases to $O(10^{-6})$, seven correct decimals can be guaranteed with $N = 300$.

4.4.2 Bifurcations and profiles

For any $R \in (0, 1)$, there is a branch of solutions bifurcating from infinitesimal periodic waves, which always leads to overhanging solutions. When $h \geq 1$, the limiting profiles of these branches are of type I and their geometry relies on the values of k and R. From a physical point of view, overhanging waves and associated limiting profiles would presumably suffer different instabilities (Kelvin-Helmholtz, Rayleigh-Taylor, etc.) and thus are difficult to be observed in experiments. However, our main concern here is the existence of limiting shapes which is separate from the question of instability. In figure 4.2, we show typical speed-amplitude bifurcation curves and related almost limiting profiles for $h = 1$. The bubble features a half-lens shape and becomes horizontally long and vertically thin when the value of k is gradually decreased for a fixed R. Note that to compare the profiles with different wavelengths, we rescale the horizontal and vertical coordinates by multiplying k, as shown in figure 4.2(b). On the other hand, for a given wavenumber k, the bubble enlarges when the value of R is increased, which is clearly demonstrated by figure 4.2(d). For general sets of parameters, bifurcation curves, along which almost limiting profiles that are either of type I or of type II, can be found. They appear qualitatively similar to those shown in Figures 4.2(a) and 4.2(c). In chapter 3, we have proposed a local model for the limiting configuration of type I for a small density ratio and calculated numerically profiles of the closed bubble. The almost limiting profiles computed with the primitive equations when both layers are deep ($h = 1$, $k = 100$) and solutions of the simplified model are shown in figure 4.3. For comparison purpose, we make sure they match at the wave crest and flat bottom. The density ratios are $R = 0.1$, 0.2, and 0.3 from top to bottom and, as expected, the smaller density ratio gives a better agreement.

When $R \to 1$, i.e. the Boussinesq limit, Grimshaw and Pullin [30] predicted the existence of the type III solution. This is intuitively reasonable since gravity is negligible and the wave profile should be invariant after being turned upside down, if one omits the possible phase shift. Maklakov and Sharipov [55] also supported this assertion but did not provide direct numerical evidence. In the top diagram of figure 4.4(a), we display an almost limiting solution in the Boussinesq limit ($R = 0.999999$) where $h = 1$ and $k = 100$ are used to approximate the condition that both layers are of infinite depth. This solution features a wave steepness of 0.1518π and a wave speed of 1.141 after being converted to the scaling of Grimshaw and Pullin [30], which agree well with the corresponding values of 0.1411π and 1.0923 for the Stokes highest

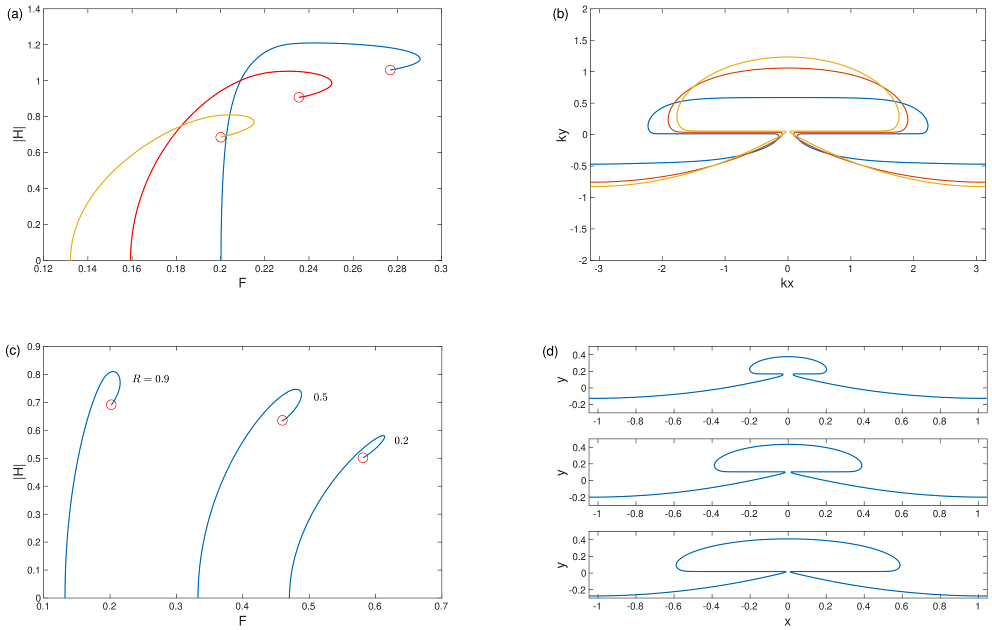

Figure 4.2: Typical speed-amplitude bifurcation curves and related almost limiting profiles. (a,b) $R = 0.9$, $h = 1$, and $k = 1$ (blue), $k = 2$ (red), $k = 3$ (yellow). (c,d) $k = 3$, $h = 1$, and $R = 0.2$, 0.5, 0.9. The corresponding almost limiting profiles are plotted from top to bottom.

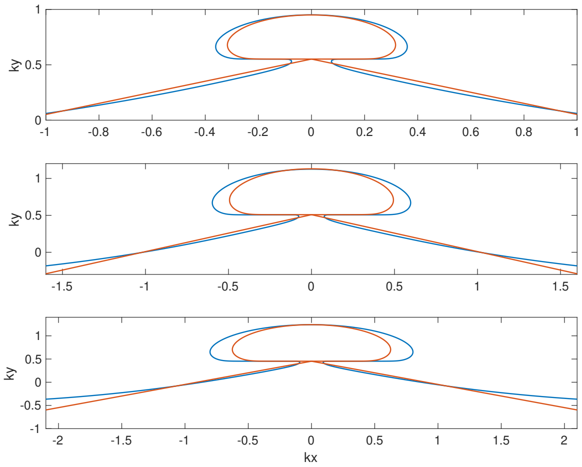

Figure 4.3: Comparisons between the almost limiting solutions (blue) and solutions of the simplified model (red) from chapter 3. The parameters are chosen as $h = 1$, $k = 100$, and $R = 0.1$, 0.2, 0.3 from top to bottom.

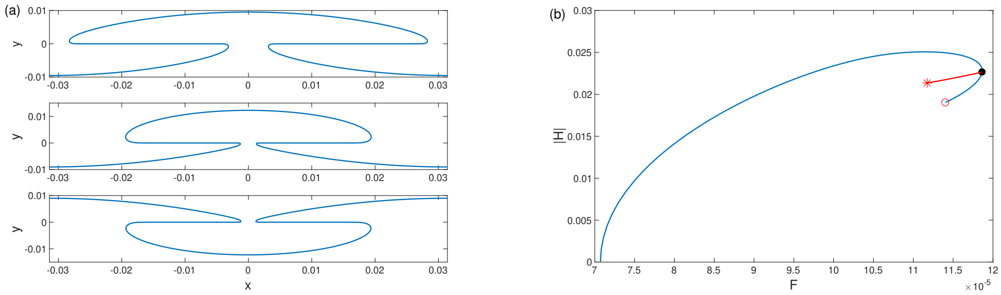

Figure 4.4: The bifurcation in the Boussinesq limit with $h = 1$, $k = 100$, and $R = 0.999999$. (a) Three almost limiting profiles that correspond to type III, type I, and type II limits from top to bottom. (b) A new speed-amplitude bifurcation branch (red) bifurcates from the primary one (blue) at a secondary bifurcation point (black dot). The circle relates to type III limit and the asterisk corresponds to type I and type II limits.

wave. It is also clear that the almost limiting profile tends to become self-intersecting at both $x = 0$ and $x = \pm\pi/k$, hence yielding a limiting profile of type III. It is not surprising that the condition $k \gg 1$ is unnecessary to lead to such solutions, since the mirror symmetry with a possible phase shift relies only on the conditions $R \to 1$ and $h = 1$ (recalling that the lower layer has a unit depth).

However, it is found that the type III solution is not the only possible limiting profile in the Boussinesq limit. Other branches of solutions can arise through a secondary bifurcation point as shown in figure 4.4(b). This is a “symmetry-breaking” mechanism since the new solutions lose the upside-down symmetry. The blue curve is the primary branch bifurcating from infinitesimal periodic waves and the red circle denotes the almost limiting configuration of type III (see the top figure of 4.4a). We check the Jacobian matrix along the primary branch and the solution is picked up as a candidate for the secondary bifurcation point if the matrix becomes nearly singular (the interested readers are referred to [18] for more details). It is shown in figure 4.4(b) that a secondary bifurcation point is found to exist (black dot), from which two coincident branches of new solutions (red curve) arise terminating at the limiting profiles of type I and type II. The almost limiting profiles are labeled by the asterisk and plotted in the middle and bottom figures of 4.4(a). Therefore, limiting

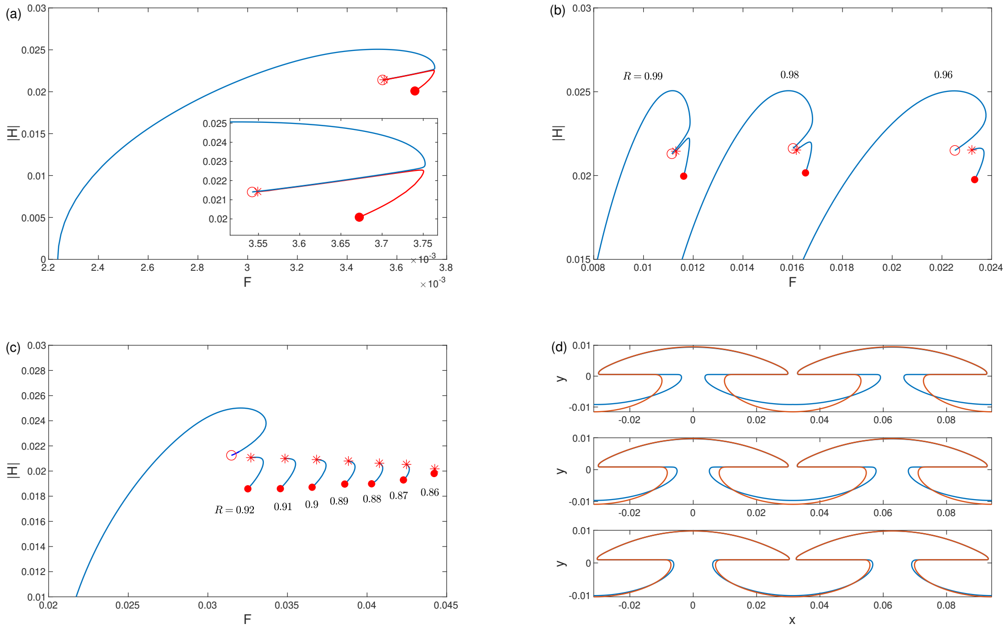

Figure 4.5: Speed-amplitude bifurcation curves and related almost limiting profiles with $h = 1$ and $k = 100$. (a) $R = 0.999$. (b) $R = 0.99$, 0.98, 0.96. (c) A series of new bifurcation branches shrinking from left to right. The leftmost curve bifurcating from a uniform flow corresponds to $R = 0.92$. (d) Almost limiting profiles with $R = 0.92$, 0.88, 0.86 from top to bottom. Blue and red profiles correspond to dots and asterisks in (c), respectively.

configurations of types I– III co-exist in the Boussinesq limit for $h = 1$.

We take one of the secondary bifurcation branches as an example (the one which terminates at the type II limit say) to explore its behavior as R varies. If the value of R is slightly decreased, one can observe a separation of the secondary bifurcation curve from the primary branch as shown in figure 4.5(a). The isolated branch connects two limiting profiles labeled by a red dot and an asterisk, both of which are of type II. Three curves for $R = 0.99$, 0.98, 0.96 are shown in figure 4.5(b), from which one can see a growing distance between the isolated branch and the primary one as R is gradually decreased. Another striking feature is the shrinking tendency of these isolated curves as R decreases (see figure 4.5c). For $R < 0.86$, the new branch almost becomes a point, which indicates that these new solutions can exist only in a specific range of parameters. Therefore, it is also expected that the difference between the two limiting profiles at opposite ends of the isolated curve should gradually diminish

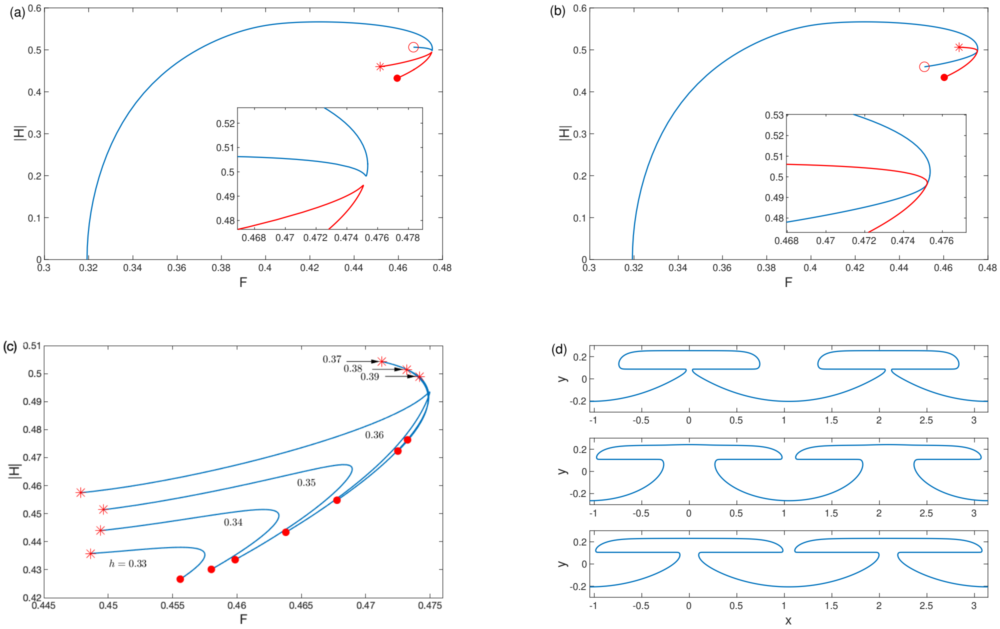

Figure 4.6: Speed-amplitude bifurcation curves and related almost limiting profiles with $R = 0.5$ and $k = 3$. (a) $h = 0.3601$. (b) $h = 0.3602$. (c) A sequence of new bifurcation curves. (d) Three almost limiting profiles corresponding to the asterisk, the circle and the dot in (a) from top to bottom.

as shown in figure 4.5(d), where blue and red curves correspond to dots and asterisks, respectively. It is worth mentioning that when the density ratio deviates from 1, the limiting configuration on the primary branch (labeled by a red circle) becomes type I, and the readers should not associate these markers (circle, dot, and asterisk) with any specific type of limit in general.

As discussed above, the existence of the secondary bifurcation and of the branch separation phenomenon is found near the Boussinesq limit. One can then ask whether or not this novel bifurcation mechanism exists in other situations. We give a positive answer to this question based on the numerical results shown in figure 4.6. For $k = 3$ and $R = 0.5$, it is found that there is a special depth ratio h_s for which three types of limiting solutions co-exist and are linked via a secondary bifurcation point. The numerical evidence shown in figure 4.6(a,b) strongly suggests $0.3601 < h_s < 0.3602$ in this case. As h deviates from h_s, there are two types of branch separation depending on whether h is decreasing or increasing. There are three sub-branches arising from the secondary bifurcation point at $h = h_s$. When h is slight below h_s, as shown in 4.6(a) for $h = 0.3601$, the top sub-branch stays on the primary branch (blue line) while the bottom two sub-branches form a new curve with a sharp corner (red line). Figure 4.6(b) shows the result for $h = 0.3602$ where the top and bottom sub-branches form a new curve (red line) breaking away from the primary branch (blue line). Note that although the two curves intersect at a common point in the parameter space as shown in 4.6(b), the two wave profiles at the intersection point are slightly different and this difference increases with h indicating the branch separation phenomenon. A sequence of new bifurcation curves for different values of h are plotted in 4.6(c) which clearly shows a transition near 0.36. Almost limiting waves akin to types I–III are labeled by the asterisk, circle, and dot in 4.6(a) for $h = 0.3601$, and corresponding typical profiles are plotted in 4.6(d) from top to bottom.

4.5 Conclusion

In the present chapter, we have investigated the bifurcation mechanism and limiting configurations of periodic interfacial gravity waves. Highly accurate numerical solutions have been obtained by applying a boundary integral equation method together with the Fourier representation of the unknown functions on the interface. Strong numerical evidence has been provided to support the existence of three kinds of limiting configurations as shown in figure 4.1. New branches of solutions, which are either isolated or connected to primary branches via secondary bifurcation points, have been discovered in both the Boussinesq and non-Boussinesq cases. The new bifurcations are due to the symmetry-breaking mechanism and can be understood as follows. At some critical points in the parameter space (k, h, R) the secondary bifurcation occurs on the primary branch and three types of limiting configurations co-exist in the same bifurcation diagram. As the parameter set deviates from the critical point, the new branch breaks away from the primary branch and gradually shrinks until it vanishes completely as the parameter set further varies.

Chapter 5

Two-layer interfacial capillary periodic waves

In this chapter, we investigate the interfacial capillary traveling-wave solutions in two-layer periodic domain. We exhibit that there exists a bifurcation mechanism similar to that of interfacial gravity waves studied in last chapter. The limiting configurations are also studied. The results of this chapter can be found in Guan et al. [36].

5.1 Introduction

Based on a hodograph transformation, Crapper [23] first found a family of exact travelling-wave solutions for capillary surface waves on a fluid of infinite depth. He found that the large-amplitude solutions have an overhanging shape and a self-intersecting limiting configuration. Such a solution can be regarded as the free surface develops a point of contact with a "trapped bubble" at the trough (see figure 5.1a). The uniqueness of Crapper's solutions was established by [63] and [62]. Crapper's pioneering work was later extended by various investigators. Kinnersley [45] generalised Crapper's waves to finite-depth case and obtained exact nonlinear solutions involving elliptic functions. Crowdy [24] provided a different derivation of Crapper's waves using conformal mapping techniques. As for the numerical investigations, Blyth and Vanden-Broeck [12] considered capillary waves on fluid sheets with two free surfaces and found secondary bifurcation branches on the symmetric Kinnersley's solution branch. Akers et al. [1] computed progressive capillary waves between two semi-infinite fluids of equal density in the presence of background shear currents. Akers et al. [2] perturbed Crapper's waves by gravity to show the existence of overhanging solutions for capillary-gravity waves. The stability properties of capillary waves were investigated respectively by Tiron and Choi [73] for Crapper's waves and by Blyth and Părău [11] for fluid sheets.

In the present chapter, progressive interfacial capillary waves in a channel of finite vertical extent are numerically studied using the Cauchy-integral method. We obtain highly accurate numerical solutions and bifurcations in various cases. New solutions are found to bifurcate from the branches that arise from infinitesimal periodic waves (referred to as the primary branches hereafter) for special sets of parameters (for example, when both layers are of the same density and thickness), akin to the symmetry-breaking bifurcation mechanism found in last chapter for interfacial gravity waves. When the parameters are perturbed, these new branches separate from the primary bifurcations and become isolated in parameter space. Besides the limiting waves of the self-intersecting type, we also find two limiting solutions of boundary-touching type (see figure 5.1(b) and (c)). For convenience, the limiting configurations shown in figure 5.1 are termed type I, type II, and type III limits from top to bottom, respectively. We examine the geometric characteristics of the boundary-touching interfaces, which are shown to be piecewise circular. This fact enables us to predict the types of limiting waves for most parameter settings.

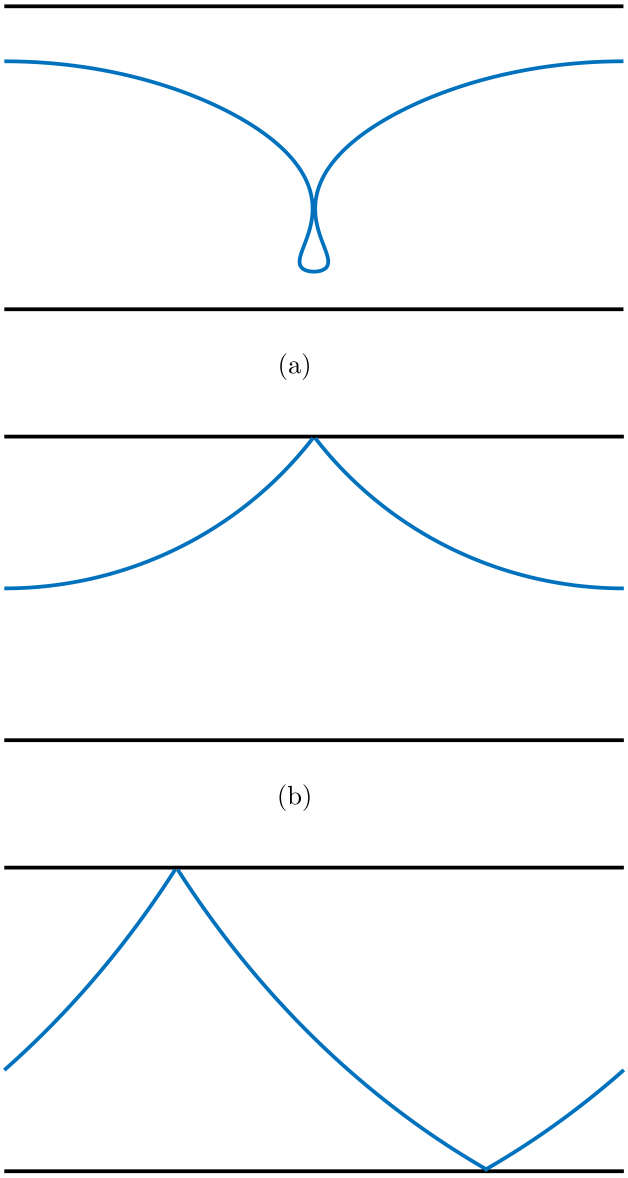

(a)

(b)

(c)

Figure 5.1: Three limiting configurations. (a): type I, (b): type II, (c): and type III.

5.2 Boundary integral equations

We consider two-dimensional periodic traveling waves moving at constant speed c through the interface between two incompressible, inviscid, and immiscible fluids. In the moving frame of reference, they are steady and assumed symmetric as stated in chapter 2. The mean depths and the densities of each fluid layer are denoted by h_i and ρ_i $(i = 1, 2)$, where subscripts 1 and 2 refer to fluid properties associated with the lower and upper fluid layers respectively. Cartesian coordinates are established such that the x-axis is on the mean level of the interface, and the y-axis on a line of symmetry. We assume that the only restoring force under consideration is surface tension. In this case, it is convenient to choose $1/k$ and c as the scalings of length and velocity.

Since the physical setting and mathematical description are similar to that of last chapter, we will skip the mathematical formulation and go to the numerical scheme. The flow is assumed to be irrotational and incompressible, thus the velocity potential ϕ_i satisfies the Laplace equation. Following the methodology same as chapter 4, we have the following Cauchy's integral formula

$$q_i(s_0)\mathrm{e}^{\mathrm{i}\theta(s_0)} + \frac{1}{\pi}\mathrm{p.v.}\oint_{C_i} \frac{q_i(s)}{1-\zeta(s)/\zeta(s_0)}\,\mathrm{d}s = 0, \qquad \text{with} \quad \zeta = \mathrm{e}^{-\mathrm{i}z} \tag{5.1}$$

where q_i is the tangential velocity on the interface, θ is the angle between the interface and the $x-$axis, s is the interface arclength, C_i represents the boundary of the lower fluid $(i = 1)$ and upper fluid $(i = 2)$, and $z = x + \mathrm{i}\eta$. Using the symmetry property of waves, we obtain two real-valued integral equations for the lower and upper layers, respectively,

$$\begin{aligned}
&\pi q_1(s_0)x'(s_0) = \\
&-\int_0^\alpha \left(\frac{q_1(s)(1-\mathrm{e}^{Y_+ + 2h_1}\cos(X_-))}{1+\mathrm{e}^{2(Y_+ + 2h_1)} - 2\mathrm{e}^{Y_+ + 2h_1}\cos(X_-)} - \frac{q_1(s)(1-\mathrm{e}^{Y_-}\cos(X_-))}{1+\mathrm{e}^{2Y_-} - 2\mathrm{e}^{Y_-}\cos(X_-)} \right) \mathrm{d}s \\
&-\int_0^\alpha \left(\frac{q_1(s)(1-\mathrm{e}^{Y_+ + 2h_1}\cos(X_+))}{1+\mathrm{e}^{2(Y_+ + 2h_1)} - 2\mathrm{e}^{Y_+ + 2h_1}\cos(X_+)} - \frac{q_1(s)(1-\mathrm{e}^{Y_-}\cos(X_+))}{1+\mathrm{e}^{2Y_-} - 2\mathrm{e}^{Y_-}\cos(X_+)} \right) \mathrm{d}s \,,
\end{aligned} \tag{5.2}$$

$$\begin{aligned}
&\pi q_2(s_0)x'(s_0) = \\
&-\int_0^\alpha \left(\frac{q_2(s)(1-\mathrm{e}^{Y_-}\cos(X_-))}{1+\mathrm{e}^{2Y_-} - 2\mathrm{e}^{Y_-}\cos(X_-)} - \frac{q_2(s)(1-\mathrm{e}^{Y_+ - 2h_2}\cos(X_-))}{1+\mathrm{e}^{2(Y_+ - 2h_2)} - 2\mathrm{e}^{Y_+ - 2h_2}\cos(X_-)} \right) \mathrm{d}s \\
&-\int_0^\alpha \left(\frac{q_2(s)(1-\mathrm{e}^{Y_-}\cos(X_+))}{1+\mathrm{e}^{2Y_-} - 2\mathrm{e}^{Y_-}\cos(X_+)} - \frac{q_2(s)(1-\mathrm{e}^{Y_+ - 2h_2}\cos(X_+))}{1+\mathrm{e}^{2(Y_+ - 2h_2)} - 2\mathrm{e}^{Y_+ - 2h_2}\cos(X_+)} \right) \mathrm{d}s \,,
\end{aligned} \tag{5.3}$$

where $Y_+ = \eta(s_0) + \eta(s)$, $Y_- = \eta(s_0) - \eta(s)$, $X_+ = x(s_0) + x(s)$, $X_- = x(s_0) - x(s)$, and α is the total arclength of the interfacial wave in half period. On the interface, we also have the Bernoulli equation

$$Rq_2^2 - q_1^2 + \frac{2\kappa}{\mu} = B \,, \tag{5.4}$$

where $R = \rho_2/\rho_1$ is the density ratio, κ is the interface curvature, B is the unknown Bernoulli constant, and $\mu = \rho_1 c^2/k\sigma$ with the surface tension coefficient σ. From definition, we have the arclength equation

$$x'(s)^2 + \eta'(s)^2 = 1 \,. \tag{5.5}$$

5.3 Numerical method and results

5.3.1 Fourier method

Following last chapter, we introduce the normalised arclength $\tau = s/\alpha \in [-1, 1]$ and write the unknowns q_1, q_2, x, and η as the following Fourier series

$$q_1(\tau) = \sum_{n=0}^{\infty} a_n \cos(n\pi\tau)\,, \tag{5.6}$$

$$q_2(\tau) = \sum_{n=0}^{\infty} b_n \cos(n\pi\tau)\,, \tag{5.7}$$

$$x(\tau) = c_0\tau + \sum_{n=1}^{\infty} \frac{c_n}{n\pi} \sin(n\pi\tau)\,, \tag{5.8}$$

$$\eta(\tau) = d_0 - \sum_{n=1}^{\infty} \frac{d_n}{n\pi} \cos(n\pi\tau)\,. \tag{5.9}$$

Truncating these series after N terms gives $4N$ unknowns: a_n, b_n, c_n and d_n (for $n = 0, 1, \cdots, N-1$). Together with α, μ and B, there are $4N + 3$ unknowns in total to be found. We introduce N equally spaced collocation points

$$\tau_n = \frac{n-1}{N-1}\,, \qquad n = 1, 2, \cdots, N\,, \tag{5.10}$$

at which equations (5.2)-(5.5) are satisfied. The integrals are numerically calculated by applying the mid-point rule together with a Fourier interpolation on another set of grid points

$$\tau_n^m = \frac{\tau_n + \tau_{n+1}}{2}, \qquad n = 1, 2, \cdots, N-1. \tag{5.11}$$

Note that there are three extra constraints

$$x(0) - x(1) = \pi \quad \Rightarrow \quad c_0 = \pi, \tag{5.12}$$

$$\int_0^\pi \eta(x)\,\mathrm{d}x = 0 \quad \Rightarrow \quad \sum_{n=1}^{N-1} \frac{c_n d_n}{2\pi n} - c_0 d_0 = 0, \tag{5.13}$$

$$\eta(0) - \eta(1) = H, \quad \Rightarrow \quad \sum_{n=1}^{N-1} \frac{d_n}{n\pi}\Big(1 - (-1)^n\Big) = -H, \tag{5.14}$$

representing the periodicity in the $x-$direction, the zero-mean interface and the pre-assigned wave amplitude. The definition of wave speed, which has been normalised to 1, requires the following two equations

$$\frac{\alpha}{\pi}\int_0^1 q_1(\tau)\,\mathrm{d}\tau = -1 \Rightarrow a_0\alpha = -\pi, \tag{5.15}$$

$$\frac{\alpha}{\pi}\int_0^1 q_2(\tau)\,\mathrm{d}\tau = -1 \Rightarrow b_0\alpha = -\pi. \tag{5.16}$$

Note that another way to define the wave speed is by fixing the Bernoulli constant $B = R - 1$. [80]

A closed algebraic system with $4N + 3$ unknowns and $4N + 3$ equations can be obtained if we abandon two integral equations, for example, those evaluated at $\tau = 1$. However, in the present work, we select one evaluated at $\tau = 1$ in (5.2) and the other evaluated at $\tau = 0$ in (5.3). It turns out that this numerical scheme, together with the Newton-Krylov method, gives more accurate results. The iteration process terminates when the maximum residual of the system is less than 10^{-10}. At the same time, we monitor the residuals of the two abandoned integral equations (denoted by δ), which we require to be less than 10^{-4} for an appropriate choice of N. Generally, we start calculating with $N = 300$, then increase N when the waves become steep or $\delta > 10^{-4}$. All the numerical results presented were recalculated with a larger N to ensure they are grid-independent within graphical accuracy.

$\lvert H\rvert/(2\pi)$	0.1	0.3	0.5	0.7	0.730
μ ($N=300$)	0.987886702	0.904591811	0.786439100	0.672820992	0.657257889
μ ($N=500$)	0.987886702	0.904591811	0.786439100	0.672820992	0.657258103
μ (Crapper)	0.987886702	0.904591811	0.786439100	0.672820992	0.657258092

Table 5.1: Comparison of μ between numerical results and Crapper's exact solutions for $h_1 = h_2 = 100$ and $R = 0$.

5.3.2 Numerical results

We do not need to worry about the Rayleigh-Taylor instability since we neglect gravity. Therefore all non-negative density ratios are allowed. However, solutions for (h_1, h_2, R) have a one-to-one relation to solutions for $(h_2, h_1, 1/R)$ if one notices that the two-fluid system can be turned upside down, namely by reversing the direction of the y-axis. This relation can be established by mapping (μ, B) to $(R\mu, -B/R)$ in the Bernoulli equation. Therefore, we shall only focus on $R \in [0, 1]$ in the subsequent computations.

In the first example, we set $h_1 = h_2 = 100$ to approximate the deep-water limit and calculate solutions for different values of R. In figure 5.2(a), we plot a collection of speed-amplitude bifurcation curves starting with infinitesimal periodic waves. The linear dispersion relation (2.17) reduces to $\mu \approx 1/(1+R)$ in this situation. In figure 5.2(b), the same branches are plotted in the $(B, |H|)$-plane. On each branch, the Bernoulli constant $B = R - 1$. This is valid under the deep-water assumption. For each value of R, as the wave amplitude increases, the wave profile gradually overhangs and ultimately develops a point of contact enclosing a pendant-shaped bubble (i.e., the type I limit). These extreme waves are labeled by the circles in figure 5.2(a) and 5.2(b). For the particular case $R = 0$, the solutions are the well-known Crapper's waves with a limiting wave height $|H| \approx 1.46\pi$ (see [23] for the explicit expression). In 5.2(a) and 5.2(c), the theoretical results of the Crapper's waves (black dots) are compared with our numerical solutions. The amplitude of the limiting wave increases with the density ratio increase; therefore, the numerical

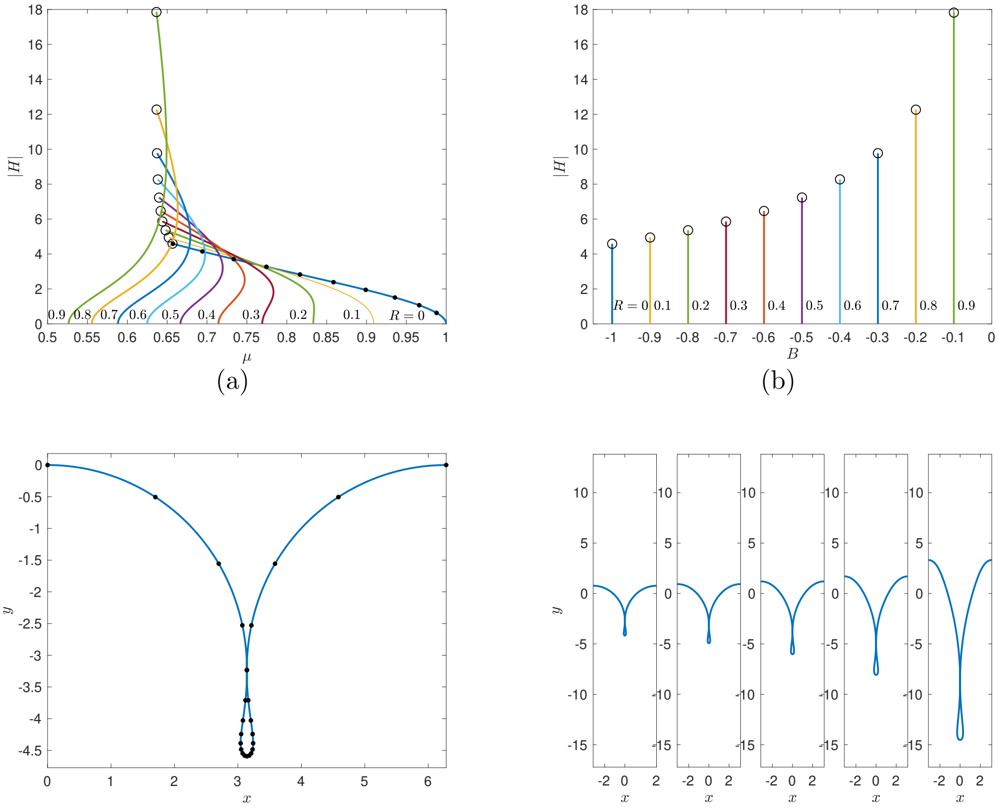

(a) (b)

(c) (d)

Figure 5.2: Bifurcation diagrams and limiting profiles for $h_1 = h_2 = 100$. (a) Speed-amplitude bifurcation curves for various density ratios. The circles correspond to the self-intersecting solutions, and the black dots represent the Crapper's waves. (b) Bifurcation curves in the $(B, |H|)$-plane for various density ratios. (c) Limiting profiles for $R = 0$: numerical solution (solid line) and analytic solution (dots). (d) Typical limiting profiles for $R = 0.1$, 0.3, 0.5, 0.7, and 0.9 from left to right, respectively.

calculation becomes more difficult for larger R. Typical profiles are shown in 5.2(d) for various R. The numerical accuracy is shown in table 5.1 via comparing the values of μ for $h_1 = h_2 = 100$ and $R = 0$ with the exact values of the Crapper's waves for given wave amplitudes. Remarkably, our numerical scheme provides at least 9-decimal-places accuracy for most solutions; even for the limiting waves, a 7-decimal-places agreement can be achieved with $N = 500$. Both Crapper [23] and Kinnersley [45] chose $B = -1$ in their calculations. This choice is equivalent to our definition of wave speed only when the fluid is of finite depth. Therefore, we choose the Crapper's wave, rather than the Kinnersley solution, to compare, although the latter deals with the finite-depth situation.

In the second numerical experiment, we let $h_1 = h_2 = 1$, a shallow-water case. The linear dispersion relation (2.17) gives $\mu = 1/(\coth(h_1) + R\coth(h_2)) \approx 0.3808$. We start the computation with small-amplitude sinusoidal waves and complete this bifurcation curve via a numerical continuation. Besides this primary branch, other bifurcation curves also exist. This is clearly illustrated by considering first the particular case $R = 1$. This is the same symmetry-breaking mechanism found in chapter 4. In figure 5.3(a), we plot the primary and new bifurcation curves (denoted by blue and red, respectively) in the $(\mu, |H|)$-plane and $(B, |H|)$-plane. Interestingly, these curves are linked together via secondary bifurcations. The black dot represents the secondary bifurcation point where the new branches start. Note that the left subfigure has two coinciding red curves. Three typical solutions corresponding to the crosses are plotted in 5.3(b). One can see that the solutions on the primary branch are invariant under the upside-down operation, which yields a zero Bernoulli constant. However, waves on the new branches mirror each other under an upside-down manipulation, thus having opposite sign Bernoulli constants. We stop the numerical continuation when the wave crest/trough almost touches a wall boundary (shown in $\triangle$, $\triangledown$, and $\diamond$ in 5.3a), because Newton's method converges poorly if the wave amplitude is further increased. These almost limiting profiles (solid lines), together with the typical streamline pattern (dashed lines) and cloud image of the velocity field, are shown in 5.3(c). Due to small fluid depths, the waves develop the type II and type III limits rather than the type I limit. We then vary the value of the density ratio to understand the bifurcation mechanism for relatively general cases. If the value of R is slightly decreased, all these branches break up from the secondary bifurcation point, forming separated curves, as shown in figure 5.3(d). This is the symmetry-breaking bifurcation mechanism found in chapter 4 for interfacial gravity waves.

If the fluid depths increase to a certain level, the limiting configuration is expected

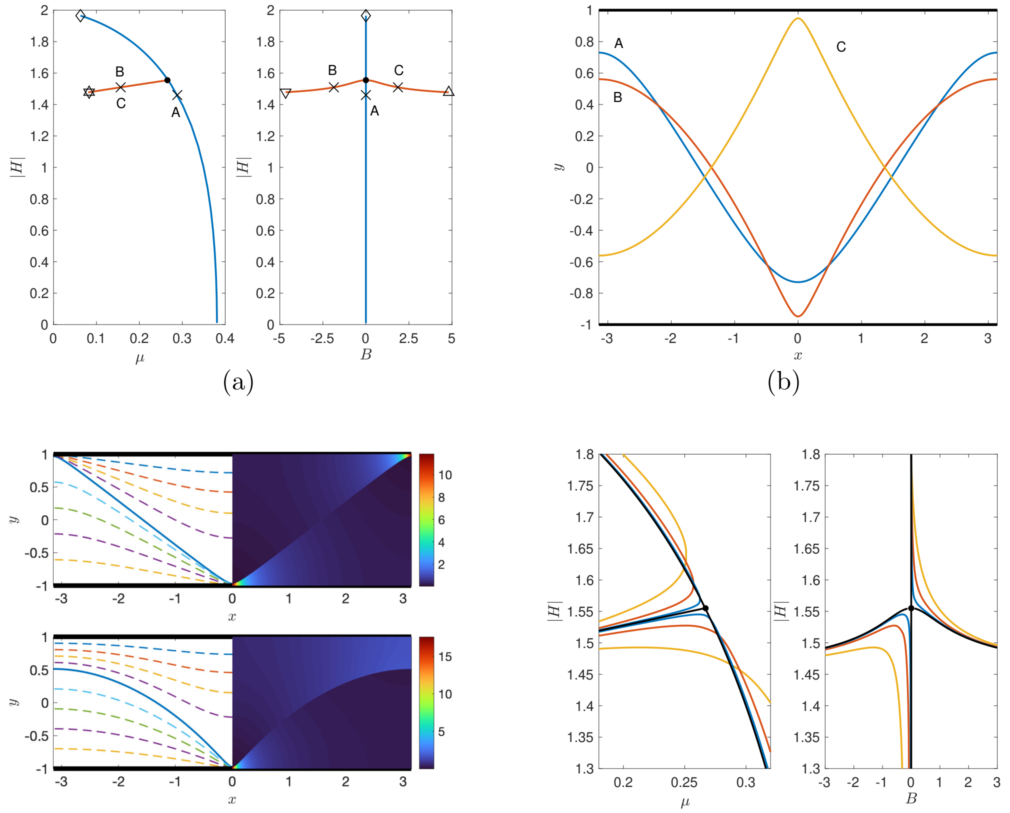

(a) (b)

(c) (d)

Figure 5.3: Bifurcation mechanism and almost limiting profiles for $h_1 = h_2 = 1$. (a) Bifurcation curves in the $(\mu, |H|)$-plane and the $(B, |H|)$-plane for $R = 1$. The black dot is the secondary bifurcation point where the new branches (red line) grow. The almost limiting profiles denoted by $\triangle$, ∇, and $\diamond$ correspond to top-touching, bottom-touching and top-bottom-touching solutions. (b) Typical wave profiles corresponding to the crosses in 5.3(a). (c) Velocity fields of the almost limiting solutions corresponding to $\diamond$ and ∇ in (a). The solid and dashed curves are interfaces and streamlines, respectively, and velocity magnitudes are shown on the right with different colors. (d) Bifurcation curves in the $(\mu, |H|)$-plane and the $(B, |H|)$-plane for $R = 1$ (black), $R = 0.99$ (blue), $R = 0.95$ (red) and $R = 0.8$ (yellow).

to become self-intersecting, as in the deep-water case shown in 5.2. In figure 5.4, we set $R = 1$, $h_1 = h_2 = 5$ and $h_1 = h_2 = 10$, and the speed-amplitude bifurcation curves are shown in 5.4(a). Similarly, secondary bifurcation points are found on the primary branches (blue), from which new branches appear. Three (almost) limiting configurations for $h_1 = h_2 = 5$ are plotted in 5.4(b). Solutions on the primary bifurcation branch feature an upside-down symmetry and ultimately form a top-bottom-touching singularity labeled by $\diamond$ in 5.4(a). On the new branches, the solutions develop overhanging profiles as the wave amplitude $|H|$ increases and become self-intersecting before the interface touches the boundary. We plot the streamline pattern and velocity cloud image in 5.4(c) for the type I limit. It is observed that the flow in the upper layer is almost uniform (similar to unit speed) except near the bubble, where it becomes almost stationary. As for the lower layer, the flow is almost static under the wave crest, while the velocity reaches its maximum in a small region under the wave trough. The bifurcation mechanism and limiting configuration for $h_1 = h_2 = 10$ are similar to those for $h_1 = h_2 = 5$.

As discussed above, the secondary bifurcation and branch separation are found near $R = 1$; however, these phenomena also occur for other parameter settings, and we show an example in figure 5.5. We set $h_1 = 3$ and $h_2 = 2$ and search for the new bifurcation branch. Our computations show that the primary and new branches approach each other when R increases to 0.5178 or decreases to 0.5179. The results for $R = 0.5178$ and $R = 0.5179$ are demonstrated in 5.5(a) and 5.5(b), respectively, where the solution branches display sharp turning points, as seen in the $(B, |H|)$-plane. We should emphasize that although the two speed-amplitude curves appear to intersect mutually in the $(\mu, |H|)$-plane of 5.5(a), it is clear that they do not have a common solution as shown in the $(B, |H|)$-plane. However, we can infer from 5.5(a,b) that an exchange of subbranches between the primary and new curves occurs at some particular density ratio, R_c, between 0.5178 and 0.5179. The computations for $R \in$

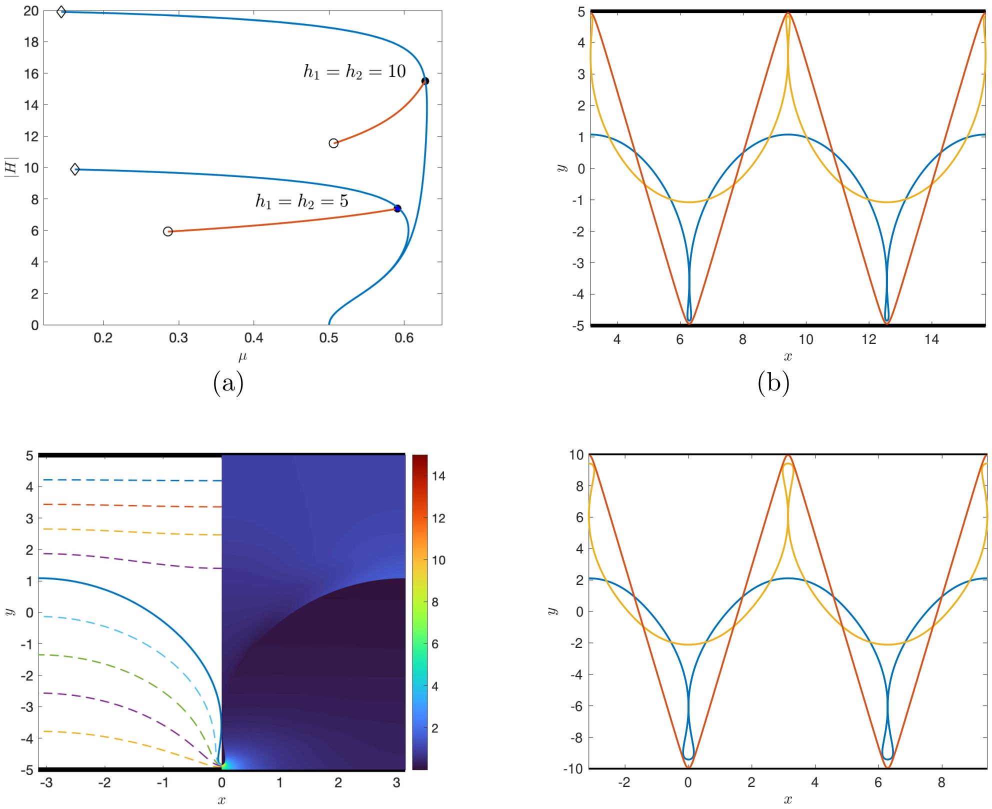

(a) (b)

(c) (d)

Figure 5.4: Bifurcation curves and wave profiles for two sets of parameters: $R = 1$, $h_1 = h_2 = 5$ and $R = 1$, $h_1 = h_2 = 10$. (a) Primary bifurcation branches (blue) and new branches (red) are linked by and secondary bifurcation point (black dots). (b, d) Almost limiting profiles for $h_1 = h_2 = 5$ and $h_1 = h_2 = 10$, respectively. Blue and yellow waves correspond to $\circ$ in (a) and red waves correspond to $\diamond$ in (a). (c) Velocity field of the limiting solutions labeled by $\diamond$ for $h_1 = h_2 = 5$. The solid and dashed curves are interface and streamlines, respectively, and the velocity magnitudes are shown on the right together with the color bar.

(0.5178, 0.5179) show some sign exchanges of the determinant of the Jacobian matrix near the turning points, giving rise to numerical difficulties in the Newton iteration near R_c. It is therefore reasonable to conclude that there exists a critical $R_c \in (0.5178, 0.5179)$ at which a secondary bifurcation point emerges to connect the two branches. In that case, following the primary branch from infinitesimal waves to the secondary bifurcation point, three subbranches subsequently appear whose limiting configurations are type I, type II, and type III, respectively. When R slightly deviates from R_c, the bifurcation curves break up and finally form two separated branches through a pairwise combination. The combination mode depends on whether $R < R_c$ or $R > R_c$. In 5.5(c), we plot the typical profiles of the three almost limiting solutions for $R = 0.5178$. A similar bifurcation-separation phenomenon is observed for other parameter settings, indicating a generic mechanism. We cannot extend these new branches to cases $R \ll 1$ or $h_{1,2} \to \infty$ since the new solutions tend to approach the wall boundaries as R decreases or $h_{1,2}$ increases. Thus one can neither continuously decrease R to zero because of numerical difficulties nor approximate solutions for $h_{1,2} \to \infty$ by a series of solutions with increasing depths.

5.4 Limiting configurations

5.4.1 Asymptotic analysis

An asymptotic analysis of the limiting configurations as $\mu \to 0$ can be performed if we rewrite the Bernoulli equation (5.4) as

$$\mu\left(Rq_2^2 - q_1^2\right) + 2\kappa - \mu B = 0\,. \tag{5.17}$$

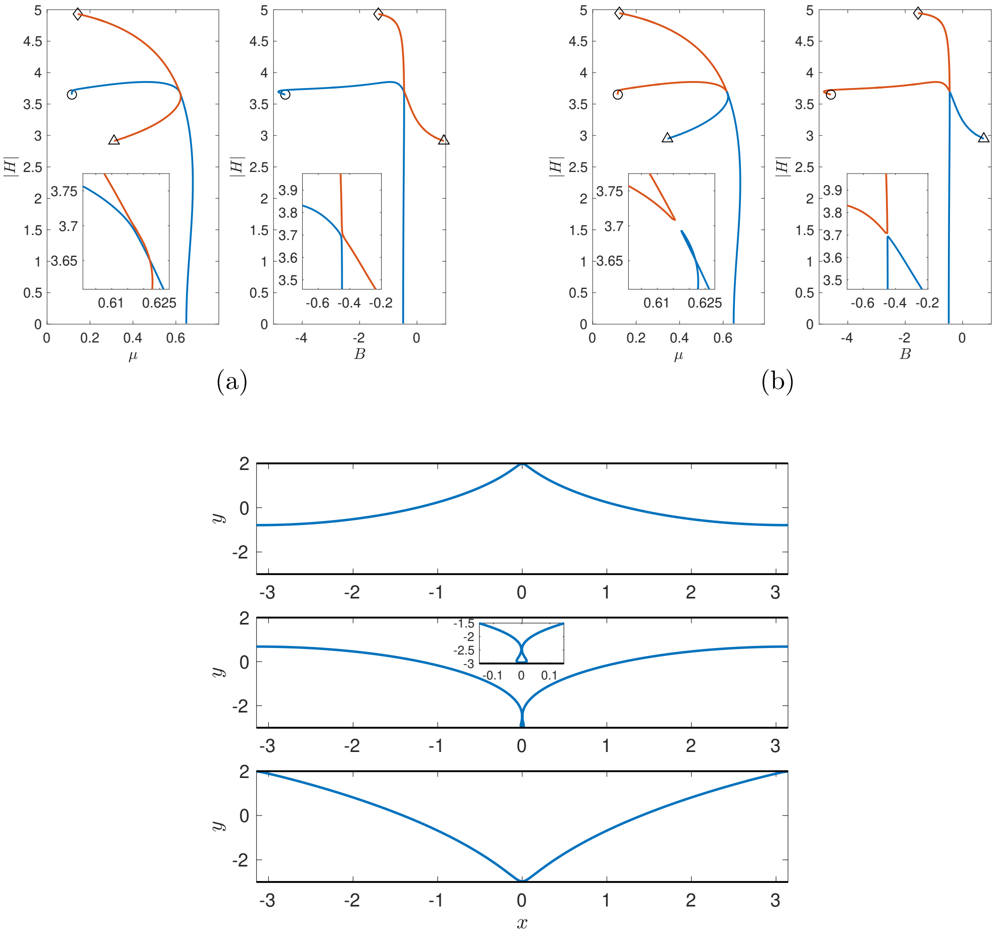

(a) (b)

(c)

Figure 5.5: Bifurcation diagrams and almost limiting profiles for $h_1 = 3$ and $h_2 = 2$. (a) Bifurcation curves in the $(\mu, |H|)$-plane and $(B, |H|)$-plane for $R = 0.5178$. (b) Bifurcation curves in the $(\mu, |H|)$-plane and $(B, |H|)$-plane for $R = 0.5179$. (c) From top to bottom, almost limiting profiles correspond to $\triangle$, $\circ$, and $\diamond$ in (a) for $R = 0.5178$.

There are two possibilities to balance the leading-order terms, namely

$$\kappa \sim \begin{cases} \dfrac{\mu}{2}\left(Rq_2^2 - q_1^2\right) \,, & \text{close to the contact point}\,, \\ \dfrac{\mu B}{2} \to \text{const.}\,, & \text{far from the contact point}\,, \end{cases} \tag{5.18}$$

indicating that the main portion of the wave describes almost a circular arc. For the particular case $R = 1$ and $h_1 = h_2$, it is already known that $B = 0$ on the primary branch. Therefore, the main section of the interface should be approximated by straight lines with slope $\pm(h_1 + h_2)/\pi$, which is confirmed by our numerical results (see figures 5.3 and 5.4). On the other hand, we must have the following scaling near the contact point:

$$Rq_2^2 - q_1^2 \sim \frac{1}{\mu^\beta}\,, \quad \kappa \sim \frac{1}{\mu^{\beta-1}}\,, \qquad \text{as } \mu \to 0\,, \tag{5.19}$$

where β is an unknown constant.

In figure 5.6(a), solutions on the primary branches for $R = 1$ and $h_1 = h_2 = 1, 5, 10$ are selected to give the μ-κ relation at $x = 0$ (red dots) and the relation between μ and $Rq_2^2 - q_1^2$ at $x = 0$ (black dots). The almost limiting profiles on these branches are plotted in 5.3(c) (top figure), 5.4(b) (red curve), and 5.4(d) (red curve). The numerical results agree well with the asymptotic relation (5.19), provided that $\beta = 2.5$. In figure 5.6(b), we choose two almost limiting solutions shown in the bottom figures of 5.3(c) and 5.5(c), plot the x-κ relation based in the numerical results (red dots) and theoretical prediction $\kappa = \mu B/2$ (black lines). It is clear from the comparisons that the segment away from the wave crest and trough approaches a circular arc.

Based on the above analyses and comparisons, we can propose two possible boundary-touching limits as shown in figure 5.1. These limiting waves only emerge when $\mu = 0$. In fact, according to the definition of waves speed (5.15) and (5.16), if

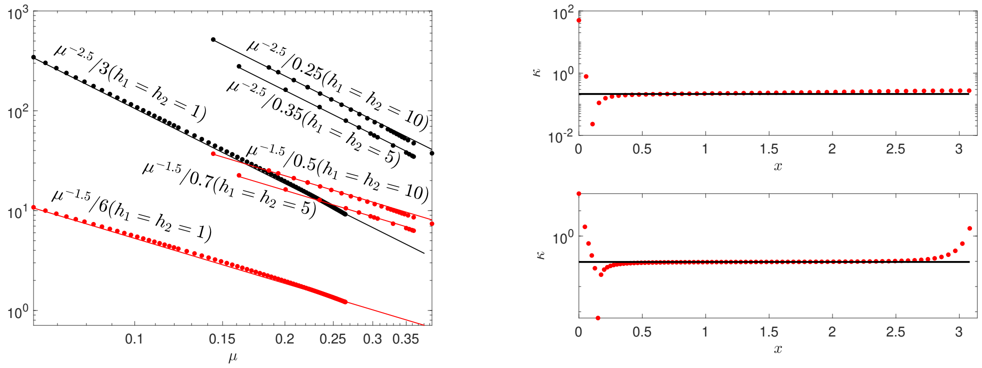

(a) (b)

Figure 5.6: (a) κ versus μ (red dots) at $x = 0$ and $Rq_2^2 - q_1^2$ versus μ (black dots) at $x = 0$ in a log scale. Numerical solutions are chosen on the primary branches for $R = 1$ and $h_1 = h_2 = 1$, 5, 10. The straight lines are the asymptotic approximations (5.19) with $\beta = 2.5$. (b) κ versus x for the almost limiting solutions shown in the bottom figures of 5.3(c) and 5.5(c).

the interface becomes boundary-touching, then there must be a bulk of static fluid, which gives rise to $c = \mu = 0$. It is also worth mentioning that both the type II and type III limits rely on the geometry of the channel, i.e., $h_{1,2}$, rather than the density ratio R, since the fluids cannot feel the influence of density difference when flows become stationary.

5.4.2 Geometry of limiting configurations

5.4.2.1 Type II

In figure 5.7, we plot the typical geometric structure of the type II limit. For the convenience of illustration, we assume the wave has a sharp angle 2γ at the contact point. Using the Pythagorean theorem to triangle OAB, we can derive the following relation between the wave height $|H|$ and limiting radius r:

$$r^2 = (r - |H|)^2 + \pi^2 \Rightarrow r = \frac{|H|}{2} + \frac{\pi^2}{2|H|}\,. \tag{5.20}$$

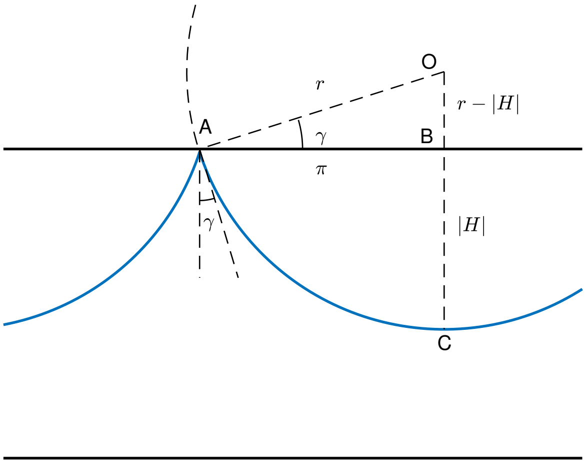

Figure 5.7: Geometric structure of the type II limit. The blue curve and black horizontal lines denote the interface and rigid walls.

To uniquely determine $|H|$ and r, one needs the condition of volume conservation, i.e., the area between the interface and the boundary in one spatial period is a constant for all waves since we fix the x-axis on the mean level of the interface. Thus we have

$$S_{\mathrm{OAC}} - S_{\mathrm{OAB}} = \pi h\,, \tag{5.21}$$

$$S_{\mathrm{OAC}} = (\pi/2-\gamma)r^2/2\,, \tag{5.22}$$

$$S_{\mathrm{OAB}} = \pi(r-|H|)/2\,, \tag{5.23}$$

where h represents h_2 (top-touching) or h_1 (bottom-touching). Eliminating r and γ, we have the equation for H:

$$\left[\frac{\pi}{2} - \sin^{-1}\left(\frac{\pi^2-H^2}{\pi^2+H^2}\right)\right]\left(\frac{\pi^2}{2|H|}+\frac{|H|}{2}\right)^2 - \pi\left(\frac{\pi^2}{2|H|}-\frac{|H|}{2}\right) = 2\pi h\,. \tag{5.24}$$

The value of $|H|$ must be within $[0,\pi]$ to ensure that $\gamma \geq 0$. One can easily show that the left-hand side of (5.24) is an increasing function of $|H|$ by drawing the function graph. The maximum value, $\pi^3/2$, is obtained at $|H|= \pi$. Therefore, the necessary

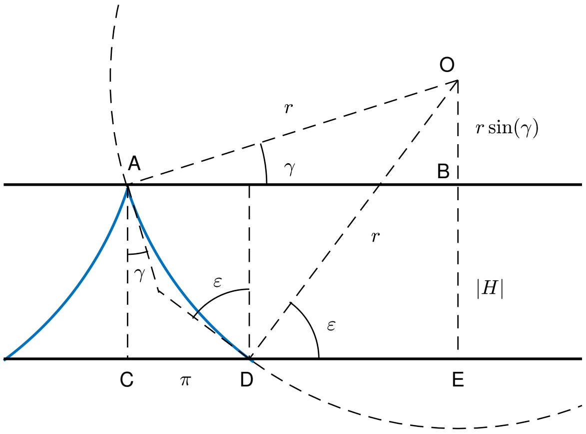

Figure 5.8: Geometric structure of the type III limit. The blue curve and black horizontal lines denote the interface and channel walls.

condition for the existence of the type II limit is

$$h \leq \frac{\pi^2}{4}\,. \tag{5.25}$$

If not satisfied, γ would become negative, implying that waves tend to overhang, and one should expect the type I limit. When condition (5.25) is met, the monotonicity of the left-hand side of (5.24) guarantees the uniqueness of the type II limit.

5.4.2.2 Type III

For the type III limit shown in figure 5.8, applying the Pythagorean theorem to the triangle ODE yields

$$r^2 = \Big(r\sin(\gamma) + |H|\Big)^2 + \Big(r\cos(\gamma) - \pi\Big)^2 \Longrightarrow r = \frac{\pi^2 + H^2}{2\Big(\pi\cos(\gamma) - |H|\sin(\gamma)\Big)}\,. \tag{5.26}$$

For the consistency of notations, the smaller one of the two crest angles is denoted by 2γ, and the larger one is marked by 2ε, where ε and γ have the following relations:

$$\begin{aligned} \sin(\varepsilon) &= \frac{r\sin(\gamma)+|H|}{r}\,, && (5.27)\\ \cos(\varepsilon) &= \frac{r\cos(\gamma)-\pi}{r}\,. && (5.28)\end{aligned}$$

Using the conservation of volume, we have

$$\begin{aligned} S_{\mathrm{OACE}} &- S_{\mathrm{ODE}} - S_{\mathrm{OAD}} = \pi h\,, && (5.29)\\ S_{\mathrm{OACE}} &= \Big(2|H|+r\sin(\gamma)\Big)r\cos(\gamma)/2\,, && (5.30)\\ S_{\mathrm{ODE}} &= \Big(r\cos(\gamma)-\pi\Big)\Big(r\sin(\gamma)+|H|\Big)/2\,, && (5.31)\\ S_{\mathrm{OAD}} &= (\varepsilon-\gamma)r^2/2\,, && (5.32)\end{aligned}$$

where h represents h_1 if the steeper crest contacts the top wall or h_2 if the other way around. Synthesizing the above equations, we have

$$\Big(|H|\cos(\gamma)+\pi\sin(\gamma)\Big)r+\pi|H|-\left[\sin^{-1}\left(\frac{(\pi^2-|H|^2)\sin(\gamma)+2\pi|H|\cos(\gamma)}{\pi^2+|H|^2}\right)-\gamma\right]r^2=2\pi h\,. \qquad (5.33)$$

One can see from figure 5.8 that there is an extra constraint on γ:

$$r\cos(\gamma)\geq\pi \Longrightarrow \tan(\gamma)\geq\frac{\pi^2-|H|^2}{2\pi|H|}\,, \qquad (5.34)$$

which gives a lower bound of γ. On the other hand, since $\gamma\leq\varepsilon$, the upper bound is obtained when $\gamma=\varepsilon$, i.e., $\tan(\gamma)=\pi/|H|$. As a result, there are two possible ranges for γ:

$$\gamma\in\begin{cases}\left[0,\ \tan^{-1}\left(\dfrac{\pi}{|H|}\right)\right]\,, & |H|\geq\pi\,,\\[2ex] \left[\tan^{-1}\left(\dfrac{\pi^2-|H|^2}{2\pi|H|}\right),\ \tan^{-1}\left(\dfrac{\pi}{|H|}\right)\right]\,, & |H|<\pi\,.\end{cases} \qquad (5.35)$$

A plot of the left-hand side of (5.33) as a function of γ yields an increasing function with the maximum value $\pi|H|$. Note that $|H|=h_1+h_2$ for type III limit, and hence

$h \leq (h_1+h_2)/2$, namely the steeper crest is always formed in the deeper layer. When $h_1 = h_2$ and $r \to \infty$, the interface becomes piecewise straight lines with slopes of $\pm(h_1+h_2)/\pi$. Using the monotonicity property, we can derive from (5.33) the range of h for the type III limit:

- $|H| \geq \pi$,

$$|H|\frac{3\pi^2+H^2}{4\pi^2} - \sin^{-1}\left(\frac{2\pi|H|}{\pi^2+H^2}\right)\frac{(\pi^2+H^2)^2}{8\pi^3} \leq h \leq \frac{|H|}{2}\ ; \tag{5.36}$$

- $|H| < \pi$,

$$\frac{\pi^2+3H^2}{4|H|} - \cos^{-1}\left(\frac{\pi^2-H^2}{\pi^2+H^2}\right)\frac{(\pi^2+H^2)^2}{8\pi H^2} \leq h \leq \frac{|H|}{2}\,. \tag{5.37}$$

When these conditions are satisfied, the monotonicity of the left-hand side of (5.33) guarantees the uniqueness of the type III limit for given fluid depths.

5.4.3 Limiting configurations in the (h_1, h_2)-plane

Next, we are able to predict the possible limiting configurations by checking h_1 and h_2. The (h_1, h_2)-plane can be divided into several regions, and the boundaries between different regions can be determined by the critical conditions given in the previous analyses. In figure 5.9, the two straight lines, CP and CF, originating from the point $(\pi^2/4,\ \pi^2/4)$, are plotted according to condition (5.25). It is easily known that the L-shaped region between two axes and PCF is where the type II limits exist. On the other hand, curves OA and OB are the lower bound of (5.37), where the coordinates of A and B are $(\pi^2/4,\ \pi - \pi^2/4)$ and $(\pi - \pi^2/4,\ \pi^2/4)$, respectively. Curves AG and BQ are the lower bound of condition (5.36), where the coordinates of D and E are $(5.4243,\ \pi^2/4)$ and $(\pi^2/4,\ 5.4243)$, respectively. Therefore, the region between the red curves is where the type III limits exist. Note that the two triangular

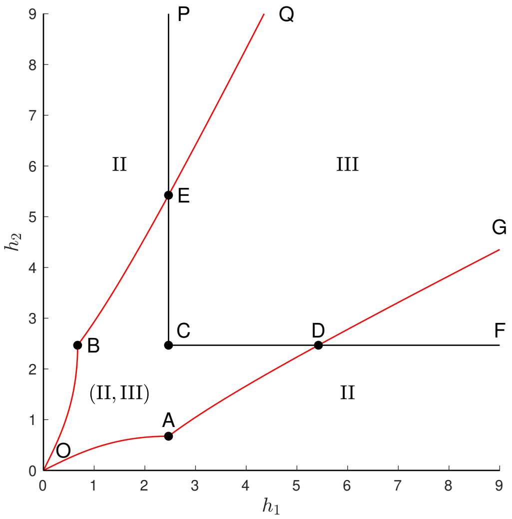

Figure 5.9: The (h_1, h_2)-plane is divided into six regions. The L-shaped region between the axes and PCF accounts for the existence of the type II limits. The wedge-shaped area between the two red curves is where the type III limits exist. The specially marked points are: O (0, 0), A ($\pi^2/4$, $\pi - \pi^2/4$), B ($\pi - \pi^2/4$, $\pi^2/4$), C ($\pi^2/4$, $\pi^2/4$), D (5.4243, $\pi^2/4$), E ($\pi^2/4$, 5.4243).

zones, GDF and QEP, support neither the type II limits nor the type III limits; hence, only the type I limits may exist in these areas.

In figure 5.10, we exhibit the limiting configurations of $R = 0.5$ with two different settings of h_1 and h_2. In (a), we choose $h_1 = 7$ and $h_2 = 3$, and this parameter setting is located in the GDF-region. Based on the above argument, there exist three different extreme solutions of type I, and this fact is confirmed by the numerical calculations. In (b), we choose $h_1 = 6$ and $h_2 = 2$, and this setting is within the L-shaped region where type II limits appear. Indeed, since $h_2 < \pi^2/4$, a top-touching solution is plausible. On the other hand, this setting is outside the wedge-shaped region between the red curves and thus excludes the type III limits. Therefore, we can infer that one limiting configuration of type II and two limits of type I coexist, which is again confirmed by the numerical results. In the bottom of 5.10(b), we compare the almost limiting profile of type II (blue) with the predicted limiting solution (red), and a satisfactory agreement is achieved.

Other numerical experiments presented in §3 also support our theoretical results.

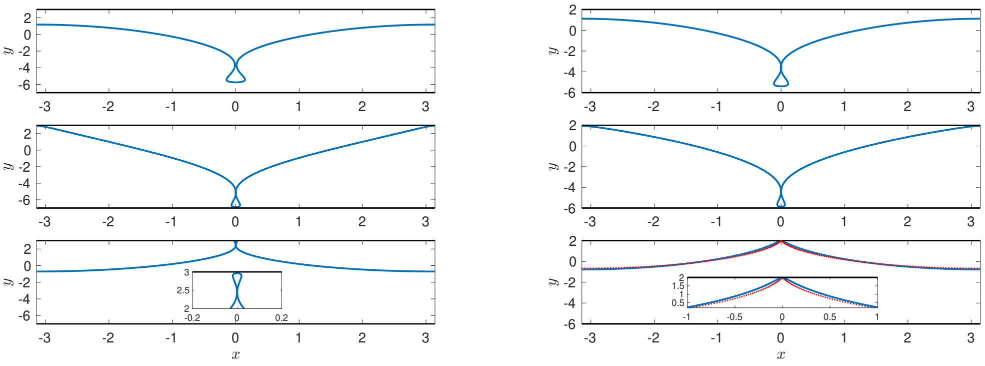
(a) (b)

Figure 5.10: Limiting configurations for $R = 0.5$ and (a) $h_1 = 7$, $h_2 = 3$; (b) $h_1 = 6$, $h_2 = 2$. In (b), the red dots represent the theoretical prediction of the limiting profile of type II.

- The case of $R = 1$ and $h_1 = h_2 = 1$, shown in figure 5.3, is within the overlap area of the L-shaped and wedge-shaped regions, thus possessing both type II and III limits. A comparison between the almost limiting solution and theoretical approximation is shown in figure 5.11 (top).

- The cases of $R = 1$ and $h_1 = h_2 = 5$, 10, shown in figure 5.4, are outside the L-shaped region but inside the wedge-shaped region, thus possessing only one limit of type III. Since there are generally two bifurcation branches, two extra limits of type I can be expected.

- The case of $R = 0.5178$, $h_1 = 3$, and $h_2 = 2$, shown in figure 5.5, is within the overlap area of the L-shaped and wedge-shaped regions. Since $h_1 > \pi^2/4$, there is only one limit of type II (top-touching) and one limit of type III. As a consequence, an extra limit of type I shold exist. Comparisons between the numerical solution of type II and III limits and theoretical predictions are shown in figure 5.11 (middle and bottom).

On the boundaries of the L-shaped and wedge-shaped regions (see figure 5.9), the extreme waves usually show mixed features. Figure 5.12 exhibits a series of theoretical limiting solutions on these boundaries. On curve OA, type III limits are

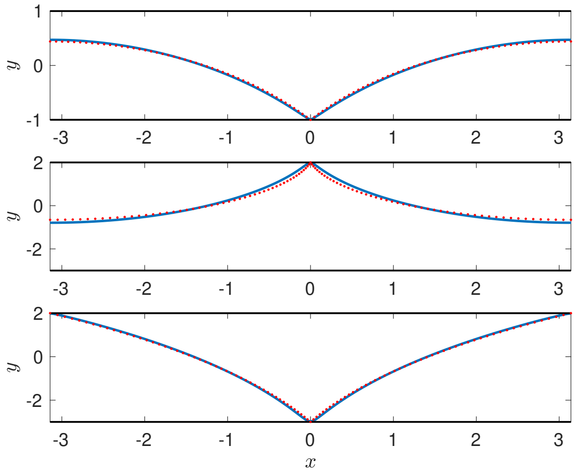

Figure 5.11: Comparisons between the numerical solutions of the almost limiting waves (blue curves) and theoretical solutions (red dots). Top: $R = 1$ and $h_1 = h_2 = 1$; middle and bottom: $R = 0.5178$, $h_1 = 3$, and $h_2 = 2$.

.

characterised by $\gamma > 0$ and $\varepsilon = \pi/2$, i.e., the crests of waves are tangential to the top wall. Therefore, these profiles can also be considered particular type II limits. As solution moves on OA, the value of γ gradually decreases until it ultimately vanishes at point A, which can be recognized from figures 5.12(a) and 5.12(A). If we continue moving onto AG, solutions are characterised by $\gamma = 0$ and $0 < \varepsilon < \pi/2$ (see the typical profile in figure 5.12(d)). However, if we trace the solution along AP after passing through point A, i.e., fixing $h_1 = \pi^2/4$ and increasing h_2, type II limits become a series of semicircle with $\gamma = 0$ (see the typical profiles in figure 5.12(b) and 5.12(C)). As to curves AG and AP, $\gamma = 0$ and thus solutions may ultimately develop into self-intersecting profiles (namely the type I limits) rather than the boundary-touching ones. Finally, we should point out that although the theoretical analysis is elementary, numerical calculations become extremely difficult near these boundaries.

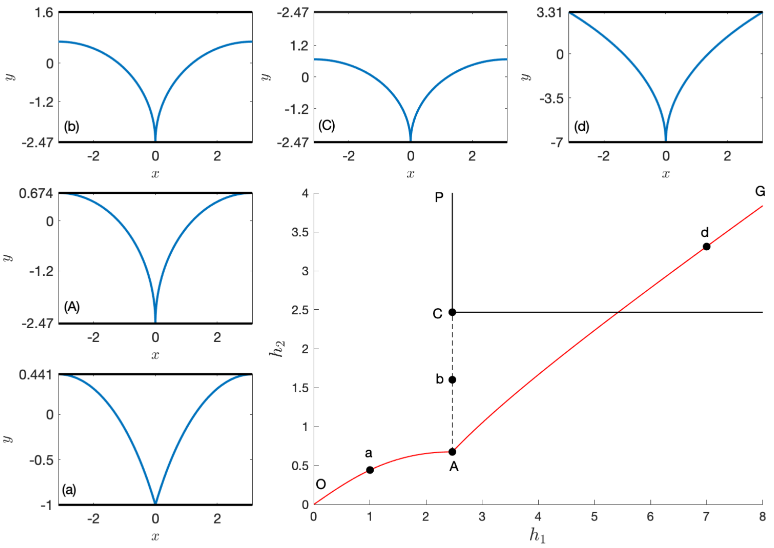

Figure 5.12: A series of theoretical limiting waves on boundaries of the L-shaped and wedge-shaped regions in the (h_1, h_2)-plane.

5.5 Conclusions

The present chapter is concerned with two-dimensional progressive interfacial capillary waves between two immiscible fluids of finite thicknesses. Highly accurate numerical solutions have been obtained via a boundary integral equation formulation and the Fourier series method. Global bifurcations and three limiting waves: type I, type II, and type III (see figure 5.1), have been investigated. New bifurcation branches are found in various cases, and the bifurcation mechanism is the symmetry breaking shown in chapter 4. In a special case, $R = 1$ and $h_1 = h_2 < \infty$, a secondary bifurcation point has been found on the primary branch, where two new curves branch out. Solutions on these new branches mirror each other under an upside-down manipulation. More generally, there are particular sets of parameters (R_c, h_{1c}, h_{2c}), for which a secondary bifurcation point emerges on the primary curve and connects all these branches. When any parameter slightly deviates from the original one, new bifurcation curves break up with the primary branch to form two isolated curves ultimately. Besides this novel bifurcation mechanism, the geometry characteristics of type II and type III limits have been thoroughly studied. The limiting profiles can be approximated by piecewise circular arcs except for the regions near wave crests and troughs, where a power-law singularity is observed. Based on these geometry properties, the (h_1, h_2)-plane can be divided into sixth regions, whereby the types of limiting configuration in each region can be predicted.

Chapter 6

Three-layer interfacial gravity periodic waves

In this chapter, we investigate periodic travelling waves in a three-layer system with the rigid-lid assumption. We calculate the mode-1 and mode-2 solutions both with and without the Boussinesq assumption. Their bifurcations and limiting configurations are described in detail. We especially concentrate on the mode-resonance mechanism. The results of this chapter can be found in Guan et al. [33].

6.1 Introduction

Density-layered models are widely used in the study of oceanic internal waves. The three-layer rigid-lid model is especially interesting since the model admits two baroclinic modes, the so-called fast mode (mode-1) and the slow mode (mode-2). Weakly nonlinear theories for three-layer flows such as the modified Korteweg-de Vries equation [31] and Gardner equation [47] have been derived and used to model solitary waves of the system. Meanwhile, the strongly nonlinear but weakly dispersive three-layer Miyata-Choi-Camassa equations were explored by Jo and Choi [44] and Barros et al. [8]. Using a fully nonlinear theory, a detailed description of three-layer conjugate states was obtained by Lamb [48]. Fully nonlinear wave computations have been computed by previous authors, who explored both mode-1 [69] and mode-2 [27] solitary waves. Fully nonlinear mode-1 and mode-2 periodic waves have been computed [19, 68]. However, a detailed description of the bifurcation space is thus far lacking, and is presented below.

The Boussinesq assumption is a common assumption made in the theory of stratified flows, and is asymptotically justified when the density differences between the layers is small compared to a reference density. The Boussinesq assumption adds a symmetry into the system of equations such that, given a solution, one can obtain an additional solution with the same speed and energy by flipping the properties (depths and densities) of the upper and lower layer and replacing interface displacements with their negative value. Furthermore, with a symmetric choice of parameters (i.e. when the density difference between the upper and middle is equivalent to the difference between the middle and lower layer, and the depths of the upper and lower layer are equivalent), some Boussinesq solutions have an additional symmetry that the two interface displacements are mirror images (potentially with a phase shift of a half wavelength of the wave). We refer to such solutions as having "upside-down" symmetry here-after. Note that not all solutions with such parameters have such symmetry, as discussed below. In this chapter, we explore the solution space both with and without the Boussinesq assumption.

While reasonable on physical grounds, both the Boussinesq and rigid-lid assumptions do have clear structural mathematical consequences which are not often emphasised in the literature, for example the aforementioned breaking of symmetry, changes in the stability characteristics [7, 13, 38, 40] of certain flows, and a momentum paradox [16].

For mode-1 Boussinesq solutions with a symmetric choice of parameters it is found that there exists an upside-down symmetric branch of solutions (with a half wavelength phase-shift between the interfaces). Along this branch, a bifurcation point is found, and the bifurcating branch has solutions which are not upside-down symmetric. In fact, there are two branches emerging from the bifurcation point: one is obtained from the other by swapping the depths and density jumps of the upper and lower layer and replacing interface displacements with their negative value, according to the symmetry in the Boussinesq system described above. All of the solutions on these branches form overhangs, until either one or both interfaces touches itself and forms a trapped bubble, as found for two-layer solutions [35, 55]. Removing the Boussinesq assumption, or changing the symmetric choice of parameters, results in two distinct solution branches, in which no solutions have the upside-down symmetry.

For mode-2 solutions, the bifurcation space is more complicated. The Boussinesq upside-down symmetric branch of solutions in this case does not have a phase-shift in the interface reflections, and in fact the streamline at the mid-depth is a horizontal line running through the middle of the middle layer. In this sense, the solutions can be seen as two-layer mode-1 solutions reflected across a wall. Unlike the mode-1 upside-down symmetric branch, the branch has not one but two bifurcation points. All solution branches again terminate with overhanging profiles, although previously unseen limiting solutions are found in which two trapped bubbles are formed either side of the overhanging region. A detailed analysis of such solutions is beyond the scope of this chapter. Breaking of the symmetry in the parameter choices (or removal of the Boussinesq assumption) results in three distinct branches. We also explore long mode-2 waves, in which mode-1 resonances are found. This results in additional branches of periodic solutions which bifurcate from a periodic Stokes wave, akin to the theory of Wilton ripples [81]. As the wavelength is further increased, the solutions ultimately approach generalised solitary waves [3, 27, 69].

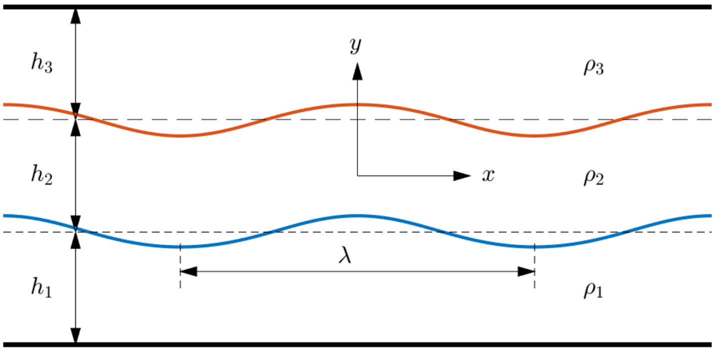

Figure 6.1: Schematic of the flow configuration. The dashed lines are the mean interfacial levels.

6.2 Mathematical formulation

Consider two-dimensional progressive waves travelling with constant speed c along two interfaces between three incompressible, inviscid and immiscible fluids layers (see the sketch in figure 6.1). We consider steady solutions on a background current of $-c$. We denote by h_j and ρ_i $(i = 1, 2, 3)$ the mean depths and densities in each fluid layer, where subscripts 1, 2, and 3 refer to fluid properties associated with the lower, middle, and upper fluid layers, respectively. We denote the wavelength of the wave as λ. A Cartesian coordinate system is introduced such that the $x-$axis is half way between the mean levels of the upper and lower interfaces, and the $y-$axis coincides with a vertical line through a wave crest/trough. We choose ρ_2, h_2, and c as the scalings of density, length, and velocity, hence in the nondimensionalised system that follows we have set $h_2 = 1$ and $\rho_2 = 1$. We concentrate on solutions with mirror symmetry about the y-axis. The flows are irrotational; hence there exist potential functions ϕ_j $(j = 1, 2, 3)$ satisfying the Laplace equation in the respective domains

$$\phi_{1,xx} + \phi_{1,yy} = 0, \qquad \text{for} \quad -1/2 - h_1 < y < -1/2 + \eta^-, \tag{6.1}$$

$$\phi_{2,xx} + \phi_{2,yy} = 0, \qquad \text{for} \quad -1/2 + \eta^- < y < 1/2 + \eta^+, \tag{6.2}$$

$$\phi_{3,xx} + \phi_{3,yy} = 0, \qquad \text{for} \qquad 1/2 + \eta^+ < y < 1/2 + h_3, \tag{6.3}$$

where h_1 and h_3 become the nondimensional depths of the lower and upper layers, η^- and η^+ are the deviations of the lower and upper layers from their mean water levels (dashed lines in figure 6.1). On the interfaces, continuity of pressure gives (making use of the Bernoulli equation)

$$\phi_{2,x}^2 + \phi_{2,y}^2 - R_1(\phi_{1,x}^2 + \phi_{1,y}^2) + \frac{2(1 - R_1)}{F^2}(-1/2 + \eta^-) = B^-, \qquad \text{at} \quad y = -1/2 + \eta^- \tag{6.4}$$

$$R_3(\phi_{3,x}^2 + \phi_{3,y}^2) - \phi_{2,x}^2 - \phi_{2,y}^2 + \frac{2(R_3 - 1)}{F^2}(1/2 + \eta^+) = B^+, \qquad \text{at} \quad y = 1/2 + \eta^+, \tag{6.5}$$

where $R_1 = \rho_1/\rho_2 > 1$, $R_3 = \rho_3/\rho_2 < 1$, $F^2 = c^2/(gh_2)$, g is the acceleration due to the gravity, and $B^\pm$ are the unknown Bernoulli constants. The Boussinesq approximation consists of setting $R_1 = R_3 = 1$ only in the kinetic energy terms above. There are four kinematic boundary conditions imposed on the interfaces

$$\phi_{1,x}\eta_x^- - \phi_{1,y} = 0, \qquad \text{at} \quad y = -1/2 + \eta^-, \tag{6.6}$$

$$\phi_{2,x}\eta_x^- - \phi_{2,y} = 0, \qquad \text{at} \quad y = -1/2 + \eta^-, \tag{6.7}$$

$$\phi_{2,x}\eta_x^+ - \phi_{2,y} = 0, \qquad \text{at} \quad y = 1/2 + \eta^+, \tag{6.8}$$

$$\phi_{3,x}\eta_x^+ - \phi_{3,y} = 0, \qquad \text{at} \quad y = 1/2 + \eta^+. \tag{6.9}$$

On the solid walls, we need to impose the following impermeability conditions

$$\phi_{1,y} = 0, \qquad \text{at} \quad y = -1/2 - h_1, \tag{6.10}$$

$$\phi_{3,y} = 0, \qquad \text{at} \quad y = 1/2 + h_3. \tag{6.11}$$

Eqs (6.1)-(6.11) complete the mathematical description of the three-layer travelling waves. There are 6 nondimensional parameters: $h_1, h_3, R_1, R_3, \lambda$, and F. Under the Boussinesq approximation, the following symmetry leaves the equations unchanged:

$$h_1 \leftrightarrow h_3, \qquad R_1 - 1 \leftrightarrow -(R_3 - 1), \qquad \eta^+ \leftrightarrow -\eta^-, \qquad y \leftrightarrow -y. \tag{6.12}$$

Hence, for each solution found in the original system, another solution exists by reflecting the original solution about $y = 0$ and appropriate reassignment of layer densities and heights. If, in addition, $h_1 = h_3$ and $R_1 - 1 = -(R_3 - 1)$, the second solution has the same physical parameters (physical domain and density stratification) as the original one. Hence if the solution itself is not symmetric about $y = 0$, a new solution may be obtained this way.

6.2.1 Linear Solutions

To obtain the dispersion relation, we consider perturbations with wavenumber $k = 2\pi/\lambda$ of the form

$$\begin{aligned}
\eta^- =& \epsilon K \mathrm{e}^{\mathrm{i}kx} + \text{c.c.}, \qquad \eta^+ = \epsilon L \mathrm{e}^{\mathrm{i}kx} + \text{c.c.} \\
\phi_1 =& -x + \epsilon P \cosh(k(y + h_1 + 1/2)) \mathrm{e}^{\mathrm{i}kx} + \text{c.c.}, \\
\phi_2 =& -x + \epsilon \Big(Q \cosh(k(y + 1/2)) + S \cosh(k(y - 1/2)) \Big) \mathrm{e}^{\mathrm{i}kx} + \text{c.c.}, \\
\phi_3 =& -x + \epsilon T \cosh(k(y - h_3 - 1/2)) \mathrm{e}^{\mathrm{i}kx} + \text{c.c.}, \\
B^- =& (1 - R_1)(1 - 1/F^2), \quad B^+ = (R_3 - 1)(1 + 1/F^2),
\end{aligned} \tag{6.13}$$

where K, L, P, Q, S and T are constant coefficients, c.c. denotes complex conjugate, and ϵ is a small parameter to measure the nonlinearity. The $-x$ term in the velocity potentials ϕ_i corresponds to the uniform stream of speed unity, arising due to the moving frame of reference. Substituting the above quantities into eqs (6.4)-(6.9) and collecting terms of $O(\epsilon)$, we can get six homogeneous linear equations for K, L, P, Q, S and T. Using the solvability condition, we can obtain a fourth order algebraic equation of F

$$\mathcal{A}F^4 + \mathcal{B}F^2 + \mathcal{C} = 0, \tag{6.14}$$

where the coefficients are

$$\begin{aligned}
\mathcal{A} =& k^2\left[1 + \coth(k)\Big(R_1\coth(kh_1) + R_3\coth(kh_3)\Big) + \coth(kh_1)\coth(kh_3)R_1R_3\right],\\
\mathcal{B} =& k\left[\coth(k)(R_3 - R_1) + R_3\coth(kh_3)(1 - R_1) - R_1\coth(kh_1)(1 - R_3)\right],\\
\mathcal{C} =& R_3 + R_1 - R_3R_1 - 1.
\end{aligned} \tag{6.15}$$

Solving this equation for the positive roots, we obtain the following two branches of the dispersion relation

$$F_1 = c_{p1}(k, R_1, R_3, h_1, h_3), \quad F_2 = c_{p2}(k, R_1, R_3, h_1, h_3), \tag{6.16}$$

where $c_{p1} \geq c_{p2}$ for the same parameters. c_{p1} and c_{p2} are the phase velocities of the mode-1 and the mode-2 waves. Mode-1 waves are defined by interface displacements of the same polarity ($KL > 0$) and mode-2 waves have interface displacements of opposite polarity ($KL < 0$). These linear solutions will be used as initial guesses to generate fully nonlinear profiles, and to motivate certain resonances between modes.

6.3 Numerical method

6.3.1 Boundary integral equations

Similar to the method used in previous chapters, we introduce the following transformation

$$\zeta = \mathrm{e}^{-\mathrm{i}kz}, \tag{6.17}$$

where k is the wave number and $z = x + \mathrm{i}y$. Introducing the complex velocity $w = \phi_x - \mathrm{i}\phi_y = u - \mathrm{i}v$, we write the Cauchy's integral formula in the ζ-plane

$$w(\zeta_0) = \frac{1}{\mathrm{i}\pi}\mathrm{p.v.}\oint_C \frac{w(\zeta)}{\zeta - \zeta_0}\,\mathrm{d}\zeta, \tag{6.18}$$

where ζ and ζ_0 are points on the boundary C of each fluid layer on which the integral is evaluated. For travelling waves, we can express the complex velocity w in terms of the velocity modulus q and the inclination angle θ as

$$w = q\mathrm{e}^{-\mathrm{i}\theta}. \tag{6.19}$$

On the interface, θ has the following relation to z

$$\frac{\mathrm{d}z}{\mathrm{d}s} = \mathrm{e}^{\mathrm{i}\theta}, \tag{6.20}$$

where s is the physical arclength parameter and we require that s is monotonically increasing along the interfaces in the direction such that the relatively heavier fluid is always to the right of the interfaces. In this way, (6.18) can be rewritten as

$$w(s_0) = -\frac{k}{\pi}\mathrm{p.v.}\oint_C \frac{q(s)}{1 - \zeta(s_0)/\zeta(s)}\,\mathrm{d}s, \tag{6.21}$$

where we have used (6.20). For the lower and the upper layer, (6.21) requires the information on the solid walls. However, using the Schwarz reflection principle, we can avoid this by reflecting the lower(upper) interface with respect to the bottom(top) wall to get a mirror image. In this fashion, the solid boundaries become a flat streamline inside the new region of the lower and upper layer, and (6.21) can be calculated by evaluating the integral on the physical interface and its mirror image.

In the lower fluid layer,

$$\zeta(s_0)/\zeta(s) = \begin{cases} \mathrm{e}^{-\mathrm{i}k\big(x(s_0)-x(s)\big)}\mathrm{e}^{k\big(\eta^-(s_0)-\eta^-(s)\big)}, & \text{on the lower interface} \\ \mathrm{e}^{-\mathrm{i}k\big(x(s_0)-x(s)\big)}\mathrm{e}^{k\big(\eta^-(s_0)+\eta^-(s)+2h_1\big)}, & \text{on the image of lower interface.} \end{cases}$$

In the upper layer,

$$\zeta(s_0)/\zeta(s) = \begin{cases} \mathrm{e}^{-\mathrm{i}k(x\big(s_0)-x(s)\big)}\mathrm{e}^{k\big(\eta^+(s_0)-\eta^+(s)\big)}, & \text{on the upper interface} \\ \mathrm{e}^{-\mathrm{i}k\big(x(s_0)-x(s)\big)}\mathrm{e}^{k\big(\eta^+(s_0)+\eta^+(s)-2h_3\big)}, & \text{on the image of upper interface.} \end{cases}$$

On the lower interface of the middle layer,

$$\zeta(s_0)/\zeta(s) = \begin{cases} \mathrm{e}^{-\mathrm{i}k\big(x(s_0)-x(s)\big)}\mathrm{e}^{k\big(\eta^-(s_0)-\eta^-(s)\big)}, & \text{on the lower interface} \\ \mathrm{e}^{-\mathrm{i}k\big(x(s_0)-x(s)\big)}\mathrm{e}^{k\big(\eta^-(s_0)-\eta^+(s)-1\big)}, & \text{on the upper interface.} \end{cases}$$

On the upper interface of the middle layer,

$$\zeta(s_0)/\zeta(s) = \begin{cases} \mathrm{e}^{-\mathrm{i}k\big(x(s_0)-x(s)\big)}\mathrm{e}^{k\big(\eta^+(s_0)-\eta^-(s)+1\big)}, & \text{on the lower interface} \\ \mathrm{e}^{-\mathrm{i}k\big(x(s_0)-x(s)\big)}\mathrm{e}^{k\big(\eta^+(s_0)-\eta^+(s)\big)}, & \text{on the upper interface.} \end{cases}$$

Finally, we can obtain four real-valued boundary-integral equations by taking the imaginary part of (6.21),

$$q_1(s_0)\sin(\theta^-(s_0)) = \underbrace{\frac{k}{\pi}\int_{-\alpha^-}^{\alpha^-} \mathrm{Im}\left(\frac{q_1(s)}{1-\frac{\zeta(s_0)}{\zeta(s)}}\right)\mathrm{d}s}_{\text{mirror image of lower interface}} - \underbrace{\frac{k}{\pi}\int_{-\alpha^-}^{\alpha^-} \mathrm{Im}\left(\frac{q_1(s)}{1-\frac{\zeta(s_0)}{\zeta(s)}}\right)\mathrm{d}s}_{\text{lower interface}}, \tag{6.22}$$

$$q_2^-(s_0)\sin(\theta^-(s_0)) = \underbrace{\frac{k}{\pi}\int_{-\alpha^-}^{\alpha^-} \mathrm{Im}\left(\frac{q_2^-(s)}{1-\frac{\zeta(s_0)}{\zeta(s)}}\right)\mathrm{d}s}_{\text{lower interface}} - \underbrace{\frac{k}{\pi}\int_{-\alpha^+}^{\alpha^+} \mathrm{Im}\left(\frac{q_2^+(s)}{1-\frac{\zeta(s_0)}{\zeta(s)}}\right)\mathrm{d}s}_{\text{upper interface}}, \tag{6.23}$$

$$q_2^+(s_0)\sin(\theta^+(s_0)) = \underbrace{\frac{k}{\pi}\int_{-\alpha^-}^{\alpha^-} \mathrm{Im}\left(\frac{q_2^-(s)}{1-\frac{\zeta(s_0)}{\zeta(s)}}\right)\mathrm{d}s}_{\text{lower interface}} - \underbrace{\frac{k}{\pi}\int_{-\alpha^+}^{\alpha^+} \mathrm{Im}\left(\frac{q_2^+(s)}{1-\frac{\zeta(s_0)}{\zeta(s)}}\right)\mathrm{d}s}_{\text{upper interface}}, \tag{6.24}$$

$$q_3(s_0)\sin(\theta^+(s_0)) = \underbrace{\frac{k}{\pi}\int_{-\alpha^+}^{\alpha^+}\mathrm{Im}\left(\frac{q_3(s)}{1-\frac{\zeta(s_0)}{\zeta(s)}}\right)\mathrm{d}s}_{\text{upper interface}} - \underbrace{\frac{k}{\pi}\int_{-\alpha^+}^{\alpha^+}\mathrm{Im}\left(\frac{q_3(s)}{1-\frac{\zeta(s_0)}{\zeta(s)}}\right)\mathrm{d}s}_{\text{mirror image of upper interface}}, \tag{6.25}$$

where $2\alpha^-$ and $2\alpha^+$ are the total arclength in a spatial period for the lower and upper interfaces, q_1 and q_3 are the tangential velocities of the lower and upper fluid layers on their corresponding interfaces, q_2^- and q_2^+ are the tangential velocities of the middle fluid layer on the lower and the upper interfaces, and θ^- and θ^+ are the inclination angles of the lower and upper interfaces. Note that we have put the point where $s = 0$ on the symmetry axis, i.e. the $y-$axis.

6.3.2 Fourier series solutions

For the convenience of numerical calculation, we introduce two pseudo-arclength parameter $\tau^\pm = s/\alpha^\pm \in [-1, 1]$ and write the following Fourier series of the six unknown functions:

$$q_1 = \sum_{n=0}^{\infty} a_n \cos(n\pi\tau^-), \tag{6.26}$$

$$q_2^- = \sum_{n=0}^{\infty} b_n \cos(n\pi\tau^-), \tag{6.27}$$

$$q_2^+ = \sum_{n=0}^{\infty} c_n \cos(n\pi\tau^+), \tag{6.28}$$

$$q_3 = \sum_{n=0}^{\infty} d_n \cos(n\pi\tau^+), \tag{6.29}$$

$$\theta^- = \sum_{n=1}^{\infty} e_n \sin(n\pi\tau^-), \tag{6.30}$$

$$\theta^+ = \sum_{n=1}^{\infty} f_n \sin(n\pi\tau^+). \tag{6.31}$$

From (6.20), we can construct the lower and upper interfaces from θ^- and θ^+ by the following equations

$$x^-(\tau^-) = \alpha^- \int_0^{\tau^-} \cos(\theta^-(\tau))\,\mathrm{d}\tau, \tag{6.32}$$

$$x^+(\tau^+) = \alpha^+ \int_0^{\tau^+} \cos(\theta^+(\tau))\,\mathrm{d}\tau, \tag{6.33}$$

$$\eta^-(\tau^-) = \eta_0^- + \alpha^- \int_0^{\tau^-} \sin(\theta^-(\tau))\,\mathrm{d}\tau, \tag{6.34}$$

$$\eta^+(\tau^-) = \eta_0^+ + \alpha^+ \int_0^{\tau^+} \sin(\theta^+(\tau))\,\mathrm{d}\tau, \tag{6.35}$$

which $\eta_0^\pm$ are unknowns. To guarantee spatial periodicity that $x^\pm(1) - x^\pm(-1) = 2\pi/k$, we must impose the following conditions

$$\alpha^- \int_{-1}^{1} \cos(\theta^-(\tau^-))\,\mathrm{d}\tau^- = \frac{2\pi}{k}, \tag{6.36}$$

$$\alpha^+ \int_{-1}^{1} \cos(\theta^+(\tau^+))\,\mathrm{d}\tau^+ = \frac{2\pi}{k}. \tag{6.37}$$

To determine $\eta_0^\pm$, we need to impose the following constraints which represent volume conservation

$$\int_0^1 \eta^- \frac{\mathrm{d}x^-}{\mathrm{d}\tau^-}\,\mathrm{d}\tau^- = 0, \tag{6.38}$$

$$\int_0^1 \eta^+ \frac{\mathrm{d}x^+}{\mathrm{d}\tau^+}\,\mathrm{d}\tau^+ = 0. \tag{6.39}$$

Also, we need to prescribe the current speed $-c$ (which has been scaled to -1) defined as the average velocity in the lower fluid

$$\frac{k}{2\pi} \int_{-\pi/k}^{\pi/k} u_1(x, y = \text{const.})\,\mathrm{d}x = -1, \tag{6.40}$$

where y = const. is an arbitrary horizontal line within the lower layer. Equation (6.40) can be rewritten in terms of q_1 using the irrotationality condition

$$\frac{\alpha^- k}{2\pi} \int_{-1}^{1} q_1 \,\mathrm{d}\tau^- = -1. \tag{6.41}$$

In addition, similar conditions for the middle and upper layers are also necessary. Here we focus on the case that all three layers have the same averaged background current (implying zero average shear between each layer). Therefore, the same condition as in equation (6.41) is adopted for q_2^-, q_2^+ and q_3, we have three extra conditions

$$\frac{\alpha^- k}{2\pi} \int_{-1}^{1} q_2^- \,\mathrm{d}\tau^- = -1, \tag{6.42}$$

$$\frac{\alpha^+ k}{2\pi} \int_{-1}^{1} q_2^+ \,\mathrm{d}\tau^+ = -1, \tag{6.43}$$

$$\frac{\alpha^+ k}{2\pi} \int_{-1}^{1} q_3 \,\mathrm{d}\tau^+ = -1, \tag{6.44}$$

which imply the following equations

$$a_0 = b_0 = -\frac{\pi}{\alpha^- k}, \;\; c_0 = d_0 = -\frac{\pi}{\alpha^+ k}. \tag{6.45}$$

6.3.3 Newton's method for the nonlinear system

Since we focus on waves which have symmetry about the $y-$axis, only half of the spatial period is needed in the computation. Therefore, we introduce N uniformly distributed mesh points $\tau_n^\pm$ in the right half interval $[0, 1]$:

$$\tau_n^\pm = \frac{n-1}{N-1}, \quad n = 1, 2, \cdots, N. \tag{6.46}$$

To avoid the singularity in the integral equations, we introduce a second set of mesh points $\tau_n^{m\pm}$

$$\tau_n^{m\pm} = \frac{\tau_n^{\pm} + \tau_{n+1}^{\pm}}{2}, \quad n = 1, 2, \cdots, N-1. \tag{6.47}$$

We let the boundary integral equations (6.22)-(6.25) to be satisfied on $\tau_n^{m\pm}, n = 1, 2, \cdots, N-1$. The integrals are calculated by the trapezoid rule using the function values on $\tau_n, n = 1, 2, \cdots, N$, which gives a spectral accuracy for periodic functions. The Bernoulli equations (6.4) and (6.5) are rewritten as

$$\begin{aligned} &(q_2^-)^2 - R_1 q_1^2 + \frac{2(1-R_1)}{F^2}\left(-\frac{1}{2} + \eta^-\right) = B^-, \\ &R_3 q_3^2 - (q_2^+)^2 + \frac{2(R_3-1)}{F^2}\left(\frac{1}{2} + \eta^+\right) = B^+, \end{aligned} \tag{6.48}$$

and satisfied on $\tau_n, n = 1, 2, \cdots, N$. Together with the four conditions (6.36) to (6.39), we have $6N$ equations to solve. To close the system, we truncate the Fourier series after N terms to get $6(N-1)$ unknown coefficients $a_n, b_n, c_n, d_n, e_n, f_n (n = 1, 2, \cdots, N-1)$ and six unknown constants $B^+, B^-, \alpha^-, \alpha^+, \eta_0^-$ and η_0^+, which makes the number of unknowns $6N$.

This nonlinear system can be solved by Newton-Krylov method. Initially, we choose a small-amplitude linear solution as the initial guess of iteration. The value of F is calculated from the dispersion relation. Once the iterations have converged to a small amplitude solution, we use continuation methods (usually with F as a continuation parameter) to compute the branch of solutions. To display the bifurcation curve clearly, we choose the wave speed F and a second parameter which measures the nonlinearity of the solutions. The wave amplitude is a candidate as usual, however, considering there are two interfaces and complex profiles, it is more appropriate to choose the wave energy E as the second parameter. It is given by

$$\begin{aligned} E = &-\frac{F^2R_1}{2}\int_{-1}^{1}\phi_1^{\mathrm{s}}\frac{\mathrm{d}\eta^-}{\mathrm{d}\tau^-}\,\mathrm{d}\tau^- + \frac{F^2}{2}\left(\int_{-1}^{1}\phi_2^{-\mathrm{s}}\frac{\mathrm{d}\eta^-}{\mathrm{d}\tau^-}\,\mathrm{d}\tau^- - \int_{-1}^{1}\phi_2^{+\mathrm{s}}\frac{\mathrm{d}\eta^+}{\mathrm{d}\tau^+}\,\mathrm{d}\tau^+\right) \\ &+\frac{F^2R_3}{2}\int_{-1}^{1}\phi_3^{\mathrm{s}}\frac{\mathrm{d}\eta^+}{\mathrm{d}\tau^+}\,\mathrm{d}\tau^+ + \frac{R_1-1}{2}\int_{-1}^{1}(\eta^-)^2\frac{\mathrm{d}x^-}{\mathrm{d}\tau^-}\,\mathrm{d}\tau^- + \frac{1-R_3}{2}\int_{-1}^{1}(\eta^+)^2\frac{\mathrm{d}x^+}{\mathrm{d}\tau^+}\,\mathrm{d}\tau^+. \end{aligned} \tag{6.49}$$

where ϕ_1^s and ϕ_2^{-s} are the potential functions of the lower and the middle fluid layers on the lower interface, ϕ_2^{+s} and ϕ_3^s are the potential functions of the middle and upper layer on the upper interface. Hereafter, the bifurcation curves will always be plotted on the (F, E) space.

The Boussinesq approximation is obtained by setting $R_1 = R_3 = 1$ in the kinetic energy terms of the Bernoulli equations (3.20), (6.48) and the energy, resulting in

$$\begin{aligned} (q_2^-)^2 - q_1^2 + \frac{2(1-R_1)}{F^2}(-\frac{1}{2}+\eta^-) &= B^-, \\ q_3^2 - (q_2^+)^2 + \frac{2(R_3-1)}{F^2}(\frac{1}{2}+\eta^+) &= B^+, \end{aligned} \tag{6.50}$$

$$\begin{aligned} E_b = &-\frac{F^2}{2}\int_{-1}^{1}\phi_1^{\mathrm{s}}\frac{\mathrm{d}\eta^-}{\mathrm{d}\tau^-}\,\mathrm{d}\tau^- + \frac{F^2}{2}\left(\int_{-1}^{1}\phi_2^{-\mathrm{s}}\frac{\mathrm{d}\eta^-}{\mathrm{d}\tau^-}\,\mathrm{d}\tau^- - \int_{-1}^{1}\phi_2^{+\mathrm{s}}\frac{\mathrm{d}\eta^+}{\mathrm{d}\tau^+}\,\mathrm{d}\tau^+\right) \\ &+\frac{F^2}{2}\int_{-1}^{1}\phi_3^{\mathrm{s}}\frac{\mathrm{d}\eta^+}{\mathrm{d}\tau^+}\,\mathrm{d}\tau^+ + \frac{R_1-1}{2}\int_{-1}^{1}(\eta^-)^2\frac{\mathrm{d}x^-}{\mathrm{d}\tau^-}\,\mathrm{d}\tau^- + \frac{1-R_3}{2}\int_{-1}^{1}(\eta^+)^2\frac{\mathrm{d}x^+}{\mathrm{d}\tau^+}\,\mathrm{d}\tau^+, \end{aligned} \tag{6.51}$$

6.4 Numerical results

6.4.1 Numerical accuracy

In table 6.1, we present the results of two-layer interfacial gravity waves previously obtained by [70] (second column), [55] (third column), two-layer model (forth column), and the results of current three-layer model (fifth column). By choosing $R_1 = 10$, $R_3 = 1$, $h_1 = 100$, $h_3 = 99$ and $k = 1$, we actually approach a two-layer interfacial deep-water wave setting whose effective density ratio is 0.1. The lower

kH	C_s(S&Y)	C_s(M&S)	C_s(two-layer)	C_s(three-layer)
0.1	1.0010433	1.001043327	1.001043327	1.001043327
0.3	1.0093851	1.009385147	1.009385147	1.009385147
0.5	1.0260381	1.026038075	1.026038075	1.026038075
0.7	1.0509243	1.050924313	1.050924313	1.050924313
0.9	1.0839603	1.083960270	1.083960271	1.083960271
1.10	1.125454	1.125454593	1.125454593	1.125454593
1.20	1.149904	1.149903889	1.149903889	1.149903889
1.30	1.177	1.177754503	1.177754503	1.177754503
1.32	—	1.183901408	1.183901408	1.183901408
1.34	—	1.190327567	1.190327567	1.190327567
1.36	—	1.197125838	1.197125838	1.197125838
1.38	—	1.204514662	1.204514662	1.204514662
1.39	—	1.208645838	1.208645838	1.208645838
1.39	—	1.213326106	1.213326106	1.213326106
1.38	—	1.210675485	1.210675485	1.210675485
1.36	—	1.204401123	1.204401123	1.204401124
1.34	—	1.197369928	1.197369928	1.197369928
1.32	—	1.189740717	1.189740717	1.189740717
1.30	—	1.181506483	1.181506483	1.181506483
1.28	—	1.172510673	1.172510673	1.172510674

Table 6.1: C_s versus kH for two-layer interfacial gravity deep-water waves with density ratio 0.1. The second and third columns are results from Saffman and Yuen [70] and Maklakov and Sharipov [55]. The results in forth and fifth columns are calculated using the two-layer model in chapter 4 and the current three-layer model with 500 Fourier modes.

interface is still a real interface separating two different fluids, while the upper interface now becomes a streamline within the upper fluid. In table 6.1, we display the computed values of C_s for different given values of kH, where C_s is the dimensionless wave speed defined by Saffman and Yuen, k is the wave number, and H is the wave amplitude defined as the difference between the displacement at the peak and the displacement at the trough. For this special deep-water case, C_s can be related to our F by the following relation

$$C_s = F\sqrt{\frac{1-R}{1+R}}, \tag{6.52}$$

where R is the equivalent density ratio for the two-layer model and equals to 0.1 in this example. In our computations, we let $N = 500$ to generate the results of three-layer model. Also, we recalculated the results of the corresponding two-layer model using the method in chapter 4 with 500 Fourier modes. It is clear from the table that our three-layer result agrees with other authors' results in the first eight decimals for all wave amplitude using 500 Fourier modes, which shows that our algorithm has an excellent numerical accuracy. Two typical solutions with different given wave heights are shown in figure 6.2 (a). We also plot solutions of the corresponding two-layer deep water system with density ratio 0.1 (black dots) for comparison. Furthermore, we compare the current three-layer model with the two layer model in a different way. Following [69], we choose $R_1 = 1.01$ and $R_3 = 0.99$ so that they satisfy $R_1 + R_3 = 2$, i.e. the middle layer has the mean density of the other two layers. We let $h_1 = h_3 = 99.5$ to approximate the deep water condition. Due to the thinness of middle layer, one can assume that this whole layer can be represented by a typical streamline, for example, the middle one. Two typical wave profiles are plotted in figure 6.2 (b), as well as the middle streamline (black dashed lines). To compare with these solutions, we choose the density ratio of the two-layer model to be $0.9802 \approx 0.99/1.01$. Two wave profiles are plotted with black dots. It should be pointed out that there is no unique way to determine which solution of the two-layer model corresponds to the chosen three-layer solution. Matching the crest-to-trough height is not always possible, for example, the streamline plotted in the bottom figure of 6.2 (b) has larger crest-to-trough height than all the two-layer solutions with density ratio 0.9802. Therefore, we choose the solution of the two-layer model in an *ad hoc* way so that it measures the mean shape of the top and bottom interface well. It should be noted that the agreement between the dashed line and the dotted line isn't good when the three-layer solution develops overhanging profile, which means the basic assumption that the middle streamline resembles the two-layer solution breaks down. In fact, it is found that even for an overhanging solution, most streamlines are still non-overhanging except those very adjacent to

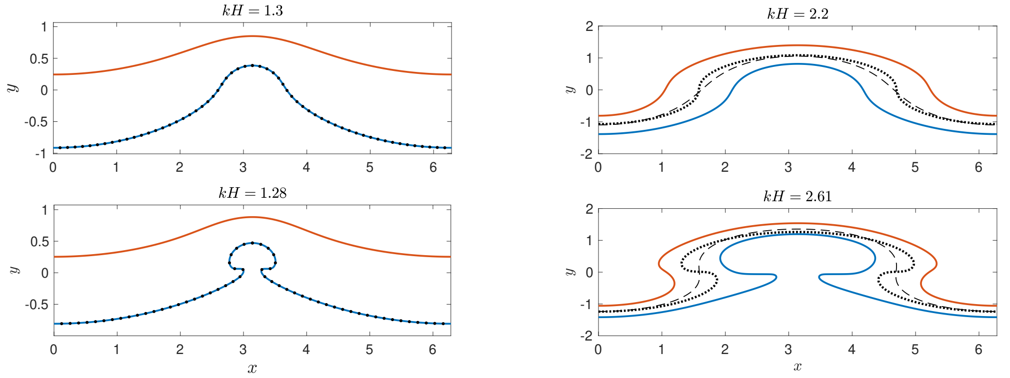

(a) (b)

Figure 6.2: (a) Typical wave profiles of $R_1 = 10$, $R_3 = 1$, $h_1 = 100$, $h_3 = 99$ and $k = 1$. The upper and lower interfaces are the solid curves. Due to the chosen parameters, the upper curve is the real interface of a two-layer system and the lower curve is a streamline. The black dots are solutions of the corresponding two-layer deep water system with density ratio 0.1. (b) Typical wave profiles of $R_1 = 1.01$, $R_3 = .99$, $h_1 = 99.5$, $h_3 = 99.5$ and $k = 1$. The black dashed lines denote the mid streamlines of three-layer solutions. The black dots are solutions of the corresponding two-layer deep water system with density ratio 0.9802. In (a) and (b), H denotes the crest-to-trough wave amplitude of the blue curve.

the interface.

6.4.2 Bifurcations and wave profiles

To clarify the bifurcation structures, we find that it is useful to compare the numerical solutions with the solutions obtained under the Boussinesq approximation. Hereafter we shall use the terms “Euler” and “Boussinesq” to distinguish the numerical solutions for the two systems when they appear in the same figure. Given the large parameter space (R_1, R_3, h_1, h_3 and k are physical parameters) we will mainly restrict our attention to the symmetric configurations and density stratification cases, assuming that $R_1 - 1 = 1 - R_3$ and $h_1 = h_3$. We shall also focus more on cases where the density contrasts are not large. With a symmetric choice of parameters and under the Boussinesq approximation, the equations have the symmetry about the mid-line of the channel referred to above, i.e. the upside-down symmetry we defined in the preceding section.

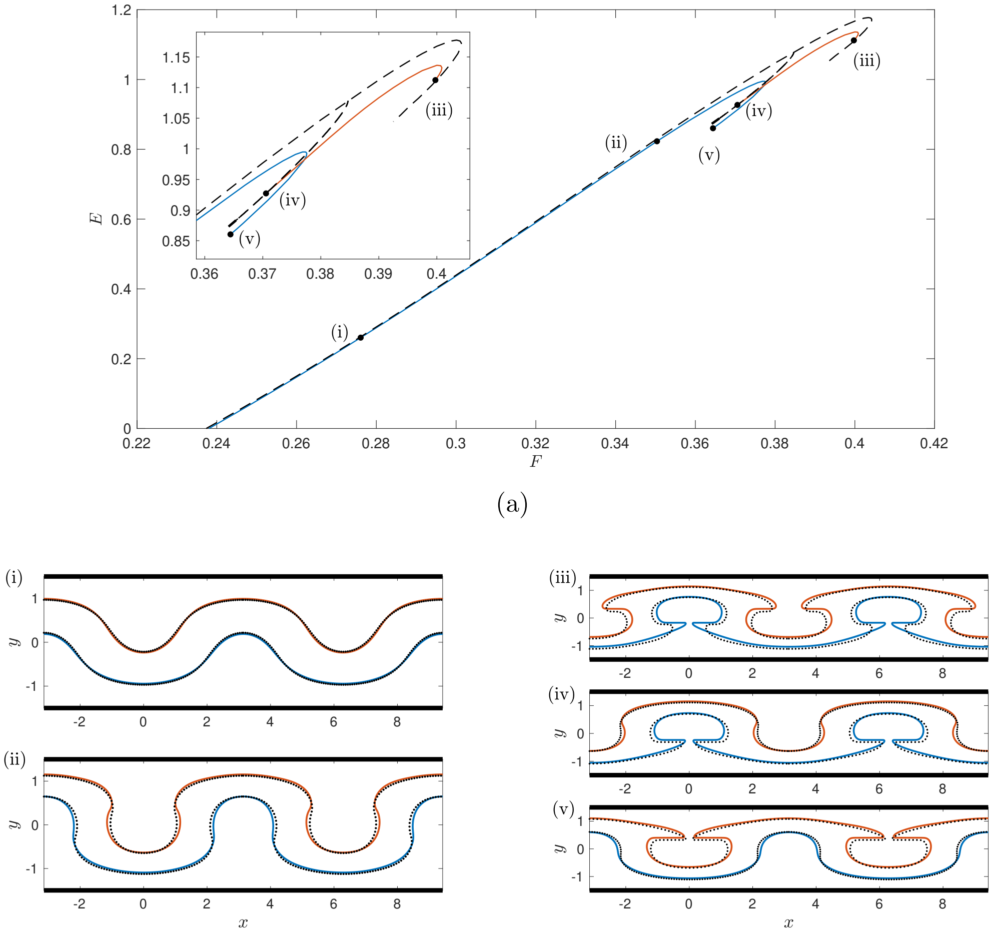

(a)

(b) (c)

Figure 6.3: Numerical solutions of mode-1 waves with $R_1 = 1.1$, $R_3 = 0.9$, $h_1 = 1$, $h_3 = 1$, $k = 1$. (a) Speed-energy bifurcation curves: solid curves (Euler), dashed curves (Boussinesq). (b) and (c) Typical solutions of the Euler (solid lines) and Boussinesq (dotted lines) cases labelled in (a) plotted at the same value of the Froude number. In (i), (ii) and (iii) the Boussinesq solutions are invariant under the transformation (6.12) (plus a phase shift of half a wavelength). In (iv) and (v) the symmetry-breaking bifurcation means that solutions obtained by the transformation (6.12) are distinct.

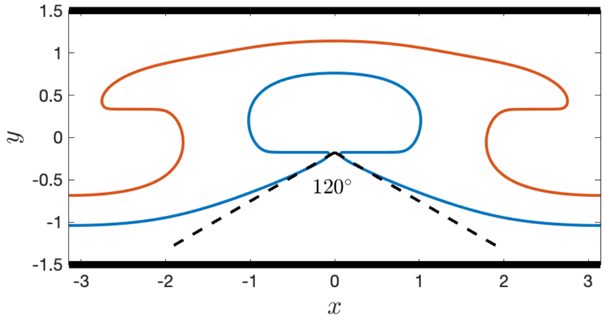

Figure 6.4: Almost limiting wave profile (iii) in figure 6.3(c) in one spatial period. The black dash line represents the limiting 120° angle.

Starting with mode-1 waves, we find in the Euler case, two closely connected bifurcation branches which collapse onto one branch in the Boussinesq case. A typical example for $R_1 = 1.1$, $R_3 = 0.9$, $h_1 = 1$, $h_3 = 1$ and $k = 1$ is shown in figure 6.3 where the branches of the Euler case and the Boussinesq case are shown. Given a solution in the Boussinesq case, we can construct another solution via operations (6.12). These either lead to the same solution with upside-down symmetry and a phase shift (symmetric branch) or a new solution without such symmetry (symmetry-breaking branch). In the latter case, the new solution and the given solution are mirror images having same energy E. The bifurcation diagram for the Boussinesq case has one symmetric branch and one symmetry-breaking branch which bifurcates near $F = 0.3845$ from the symmetric branch. The Boussinesq case is in excellent agreement with the Euler case when the energy is small. The difference between the Boussinesq and the Euler cases becomes significant when the wave energy is increased. The solutions in the Euler case do not have the upside-down symmetry, hence splitting the symmetry-breaking branch of the Boussinesq curve into two distinct curves which terminate at different points, where one of the interfaces touches itself. The branches of the Euler's equations are shown by the blue and red curves in the figure.

In Figure 6.3 we also display five typical profiles of solutions to the Euler equation along the two branches. Solution (i) is almost upside-down symmetric (with a phase

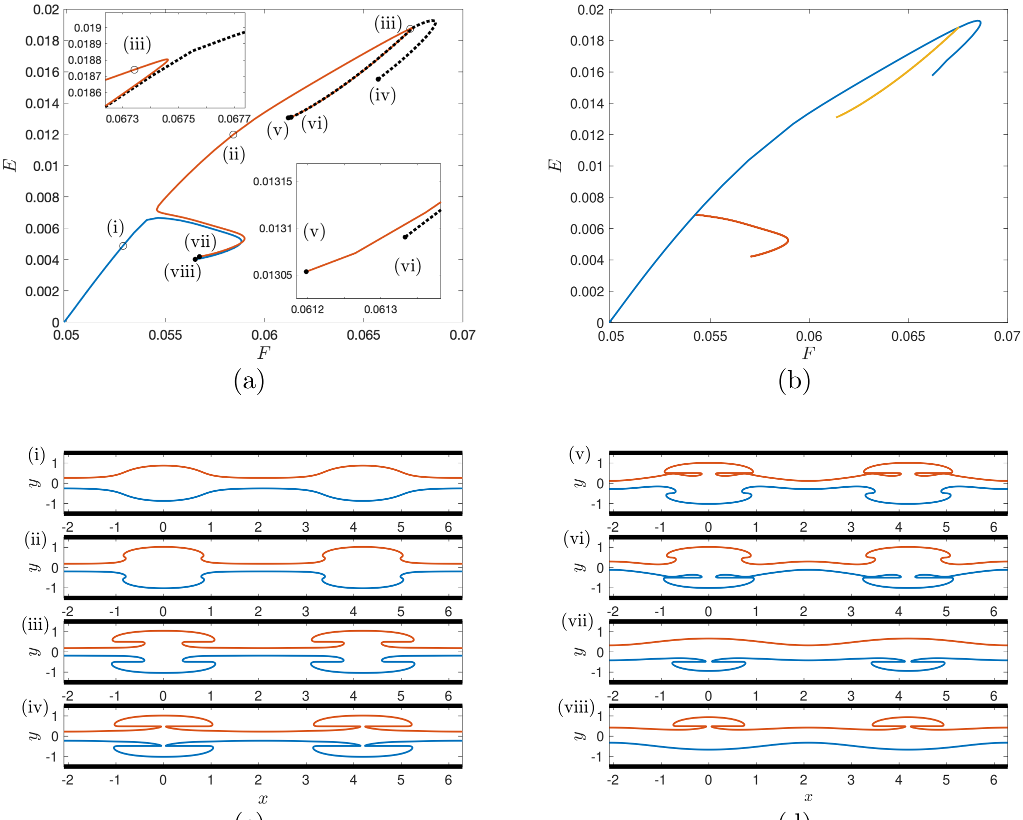

(a) (b)

(c) (d)

Figure 6.5: Numerical solutions of mode-2 waves with $R_1 = 1.01$, $R_3 = 0.99$, $h_1 = 1$, $h_3 = 1$, $k = 1.5$. (a) Speed-energy bifurcation branches of the Euler case. (b) Speed-energy bifurcation branches of the Boussinesq case. (c, d) Typical wave profiles of Euler case which are labelled in (a) and plotted in two spatial periods.

shift), while solution (ii) has developed some asymmetry. Solutions of the Boussinesq case with the same values of F are also plotted in (b) by the black dots. Solutions (i) of the Euler case and Boussinesq case are almost indistinguishable, while solutions (ii) exhibit some slight differences as expected because solutions in the Boussinesq case are always upside-down symmetric. The three almost limiting waves (iii), (iv) and (v) also do not exhibit upside-down symmetry although (iv) and (v) are approximately mirror images, as they are close to the symmetry-breaking Boussinesq bifurcated branch. As in the two-layer interfacial gravity wave case, the mode-1 waves also feature overhanging profiles and self-intersecting singularities when the wave energy is sufficiently large. From the almost limiting waves (iii), (iv) and (v), it is reasonable to expect that their limiting waves would develop closed fluid bubbles on one of the interfaces and form a sharp angle at the intersection points. Using a local asymptotic analysis, one can show that it is possible for the interface to develop a 120° angle in contact with a closed fluid bubble. In figure 6.4, a local blow-up of the almost limiting profiles (iii) of figure 6.3 is shown, as well as two dashed lines placed at 120° to each other.

For mode-2 waves, more than two bifurcation branches are usually found, which increases the complexity of the bifurcation structure. An example is shown in figure 6.5. The corresponding parameters are $R_1 = 1.01$, $R_3 = 0.99$, $h_1 = 1$, $h_3 = 1$ and $k = 1.5$. In 6.5 (a) and (b), we plot the energy-speed bifurcation curves of the Euler case and the Boussinesq case respectively. Due to the weak density stratification, the Boussinesq case displays an excellent agreement with the Euler case, with almost indistinguishable bifurcation curves. There are now two symmetry-breaking bifurcation points (F approximately 0.054 and 0.068) on the symmetric Boussinesq branch (blue) and two folded symmetry-breaking branches (red and yellow) grow from these points. Solutions (i) to (iv) in figure 6.5(c) are the almost symmetric solutions which can be seen both from their profiles and the fact that they lie near the symmetric

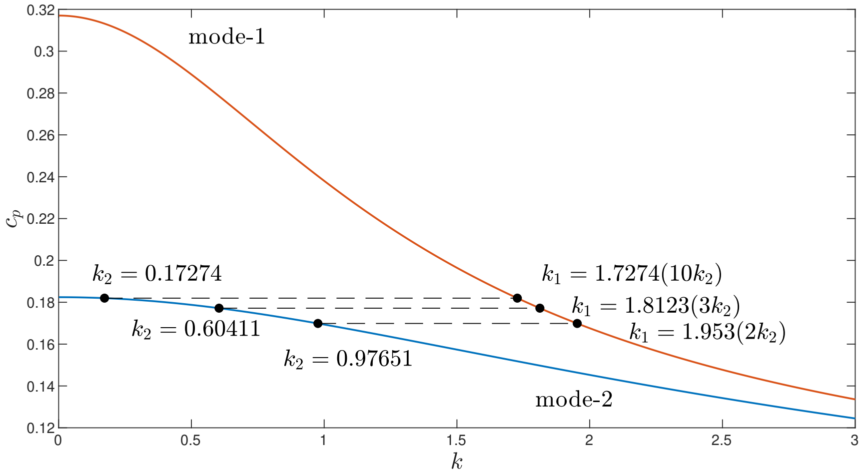

Figure 6.6: Dispersion relation curves with $R_1 = 1.1$, $R_3 = 0.9$, $h_1 = 1$ and $h_3 = 1$. The upper and lower curves correspond to the mode-1 and mode-2 waves. The horizontal dashed lines represent three possible resonant pairs (k_1, k_2) for which $k_1/k_2 = 2, 3, 10$ respectively.

branch of the Boussinesq approximation. On the other hand, solutions (v) to (viii) are almost limiting profiles of the symmetry-broken waves. It is interesting to note that these solutions show some characteristics of mode-1 waves, which is probably due to the mode-resonance mechanism described below. Like the mode-1 waves, we also expect the corresponding limiting waves to have closed bubbles attached to 120° angles. Solutions (iv), (vii) and (viii) are the almost limiting waves of this type. However, there are other possible limiting waves as solutions (v) and (vi) suggest. Taking solution (v) for example, one can infer that the upper interface (red) becomes self-intersecting if the local peak ($x \approx \pm 0.8$) touches the mushroom's base. In this fashion, there will be two closed fluid bubbles (of the upper fluid) which are symmetric with respect to the vertical lines $x = 0$. A further discussion on this new limiting configuration is beyond the scope of the current chapter and shall not be addressed here.

For longer periodic mode-2 waves (k decreasing) the complexity of the bifurcation curves increases as there is the possibility of important resonances between the mode-2 waves and the mode-1 waves. Analogous to the well-known case of Wilton Ripples in capillary-gravity surface waves [81], it is possible to find two wavenumbers k_1 and

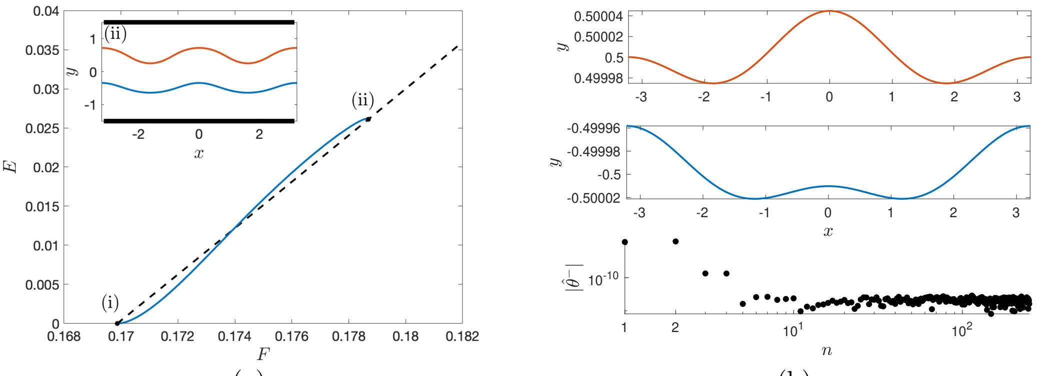

(a) (b)

Figure 6.7: (a) Speed-energy bifurcation cures with $R_1 = 1.1$, $R_3 = 0.9$, $h_1 = 1$, $h_3 = 1$, $k = 0.97651$(blue, mode-2), and $k = 1.953$(black, mode-1). The energy of the mode-1 waves are calculated in two spatial periods. The figure in the upper left box shows the wave profile of solution (ii). (b) The top and middle figure are the upper and lower interfaces of solution (i) in (a). The bottom figure displays the absolute value of $\widehat{\theta}^-$ of solution (i) in a log-scale, where $\widehat{\theta}^-$ is the Fourier coefficient of the lower interfacial inclination angle θ^-, and n is the order of the Fourier modes.

k_2 such that

$$c_{p1}(k_1) = c_{p2}(k_2), \quad mk_1 = nk_2, \quad n > m \text{ are two positive integers,} \tag{6.53}$$

where $c_{p1}(k_1)$ is the phase speed of the mode-1 waves for $k = k_1$ and $c_{p2}(k_2)$ is the phase speed of the mode-2 waves for $k = k_2$. A similar mechanism has been pointed by [19] who focused on the case $m = 1$. These resonances can be seen from figure 6.6, where we plot the dispersion relation curves for $R_1 = 1.1$, $R_3 = 0.9$, $h_1 = 1$, and $h_3 = 1$. For simplicity, we shall use the term (m, n) resonance to denote such conditions. Three examples corresponding to $(1, 2)$, $(1, 3)$ and $(1, 10)$ are shown in figure 6.6 by the three dashed horizontal lines. There exist a countable number of resonant pairs since $n/m \to \infty$ when $k_2 \to 0$. These resonant pairs imply that if one chooses the wavenumber to satisfy (6.53), then, linearly, a mode-1 component and a mode-2 component coexist. This has consequences in the nonlinear solution branches.

In figure 6.7, we display the special example corresponding to the $(1, 2)$ resonance of figure 6.6. In 6.7(a), the blue curve is the speed-energy bifurcation branch of solutions with $k = 0.97651$ (which corresponds to one branch of Wilton ripple-like solution), and the black dashed curve is the speed-energy bifurcation mode-1 waves with $k = 1.953$ for which the energy is calculated in two spatial periods. Solution (i), which is labelled by a black dot, is a small-amplitude linear wave, so we plot the corresponding upper interface(red) and lower interface(blue) in 6.7(b) respectively. In the bottom figure of (b), we plot $|\widehat{\theta}^-|$ versus n in a log-scale, where $\widehat{\theta}^-$ denotes the Fourier coefficient of the lower interfacial inclination θ^-, and n is the order of the Fourier modes. It is clear that only the first two Fourier modes are significant while the rest are tiny enough to be neglected. Because of the existence of the resonant pair, the wave profile of (i) exhibits a mixture of the mode-1 and mode-2 waves. When the value of F increases, the energy monotonically grows until the mode-2 wave bifurcation curve intersects the mode-1 wave bifurcation curve near $F = 0.1787$. The final solution (ii) is a mode-1 wave and is shown in the small box in figure 6.7(a). In general, this mode resonance still exists when k_1/k_2 is a rational number rather than just an integer. In this case, we expect to see n mode-1 wave components coexist with m mode-2 waves, at least in the linear region. Figure 6.8 displays an example with parameters: $R_1 = 1.01$, $R_3 = 0.99$, $h_1 = 1$, $h_3 = 1$ and $k = 0.2525$. According to the dispersion relation, the $(2, 7)$ resonance is predicted when $k_1 \approx 1.7679$ and $k_2 \approx 0.5051$. Therefore, we choose the length of the computing domain to support two mode-2 waves with $k = 0.5051$ or seven mode-1 wave with $k = 1.7679$. Three typical solutions are labelled on the local energy-speed bifurcation curve in 6.8(a), their wave profiles are plotted in 6.8(b). As the figure clearly shows, solution (i) is almost a standard mode-2 wave having two spatial periods. Solution (ii) has already generated some mode-1 components and clearly lost the double periodicity. Solution (iii) almost becomes a mode-1 wave and develops seven quasi-periodic mode-1 waves.

In fact, due to the nonlinearity, the resonant condition (6.53) only needs to be

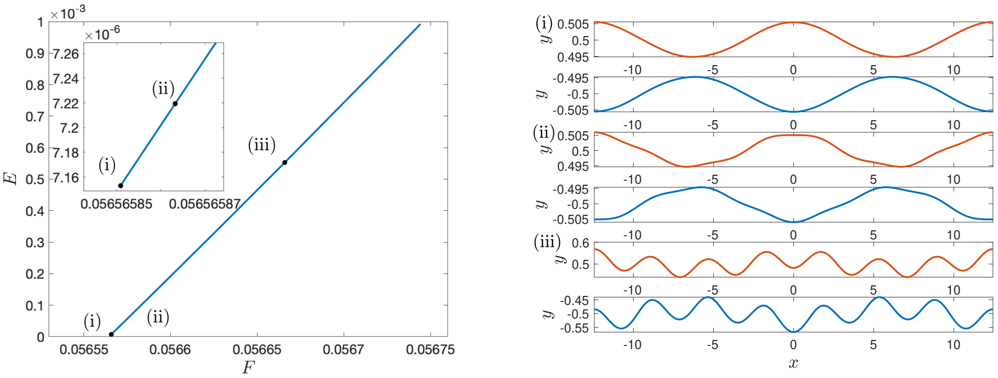

(a) (b)

Figure 6.8: (a) Speed-energy bifurcation cures with $R_1 = 1.01$, $R_3 = 0.99$, $h_1 = 1$, $h_3 = 1$ and $k = 0.2525$. (b) Three typical wave profiles corresponding to the labelled solutions in (a). The red and blue curves are the upper and lower interfaces.

satisfied approximately to support the resonance. In figure 6.9, we plot six speed-energy bifurcation branches of the mode-2 waves with $R_1 = 1.1$, $R_3 = 0.9$, $h_1 = 1$, $h_3 = 1$, and $k = 1$. The black dashed lines are the speed-energy bifurcation curve of the mode-1 waves with $k = 2$. The blue curve and part of the red curve are of the $(1, 2)$ resonant type. The wave profiles of solutions (i) and (ii) are shown in the small boxes. This clearly indicates that they become the mode-1 waves with wavenumber $k = 2$. Nine almost limiting wave profiles are shown in figure 6.10. Note that the blue curve is not the only one which intersects the mode-1 bifurcation curve, the cyan branch also has an intersection at solution (x). The corresponding profile is a rather nonlinear mode-1 wave with an overhanging upper interface. This means that the mode-resonance exists not only in the weakly nonlinear region but also when solutions become highly nonlinear. Solutions (v) to (ix) are similar to those shown in figure 6.5. However, solutions (iii), (iv) and (xi) suggest the existence of a new limiting wave, but we shall not discuss it in the current chapter.

An important question is how the bifurcation structure and wave profiles change when the five related parameters R_1, R_3, h_1, h_3 and k are gradually varied. In general, if we change the depth h_1 and h_3 but keep the other parameters fixed, the bifurcation structures and solutions are quantitatively similar. Wave profiles

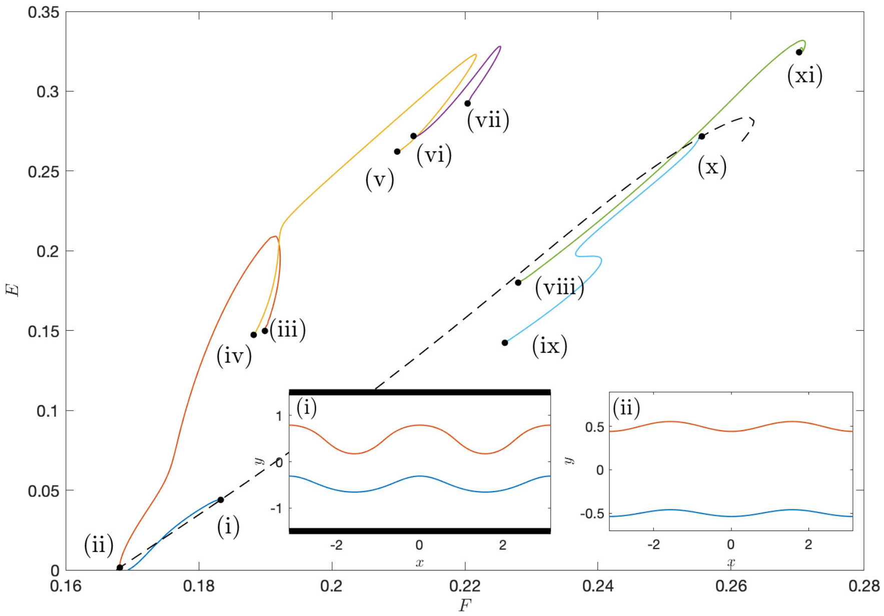

Figure 6.9: Energy-speed bifurcation curves and two related wave profiles of the mode-2 solutions with $R_1 = 1.1$, $R_3 = 0.9$, $h_1 = 1$, $h_3 = 1$ and $k = 1$. Associated (almost) limiting waves are labelled by black dots on curves. The black dashed line is the energy-speed bifurcation of the mode-1 solutions for the same values of R_1, R_3, h_1, h_3 and $k = 2$ whose energy is calculated in two spatial periods. The two small boxes show the wave profiles corresponding to (i) and (ii).

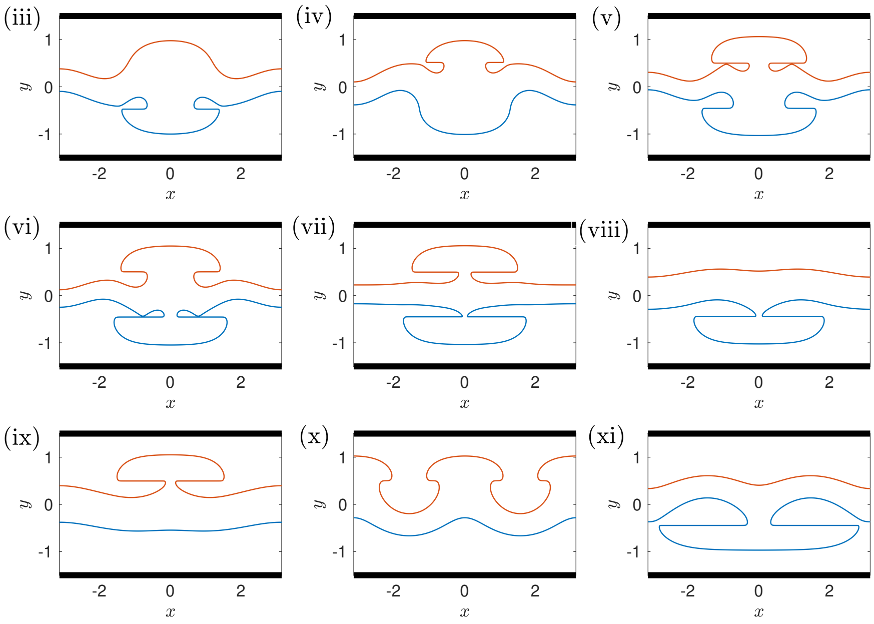

Figure 6.10: Almost limiting wave profiles corresponding to the nine labelled solutions (iii) to (xi) in figure 6.9.

become spatially longer(shorter) if the depth is increased(decreased). On the other hand, if we gradually change the values of R_1 and R_3 away from the weak density stratification, but keep $(R_1 - 1)/(1 - R_3)$ constant, i.e. the lower and the upper layer have the same density variation to the density of the middle layer, then one generally observe that the adjacent solution branches gradually get further away from each other in the speed-energy bifurcation space. In figure 6.11, we display two numerical results with with $h_1 = h_3 = 1$, $k = 1$, $R_1 = 1.3$, $R_3 = 0.7$ (left) and $R_1 = 1.5$, $R_3 = 0.5$ (right). For these two cases, the bifurcation structure is complex and the Boussinesq approximation is no longer valid since the density stratification is no longer weak. Comparing the bifurcations and the almost limiting wave profiles displayed in figure 6.12 with the numerical results shown in figure 6.9 and 6.10, it is noted that the number of bifurcation branches is decreased to four and some typical solutions in figure 6.10 vanish. In fact, this was also found in the two-layer interfacial waves that some bifurcation branches gradually shrink and ultimately disappear in the bifurcation space when the related parameters are varied. Note that the $(1, 2)$ resonance exists when $k \approx 1.1$ for $R_1 = 1.3$, $R_3 = 0.7$ and when $k \approx 1.43$ for $R_1 = 1.5$, $R_3 = 0.5$. Therefore, we do not directly observe the mode-resonant phenomenon for these two cases since the wavenumbers that we choose is not very close to these critical wavenumbers. However, solutions (i), (ii) and (iii) still display some characteristics of resonance and can be thought of as the nonlinear evolution of mode resonance. The waves in figure 6.12 show that the possible limiting configurations are either a closed bubble attached to a 120° angle, or two closed bubbles located symmetrically to the vertical line $x = 0$, or special mode-1 waves having larger wavenumber. It is interesting to note that the almost closed bubble on the upper interface could have both upward and downward orientations.

If we fix the values of R_1, R_3, h_1 and h_3, but gradually decrease k, then we obtain a family of long waves which converges to generalised solitary waves. In this process,

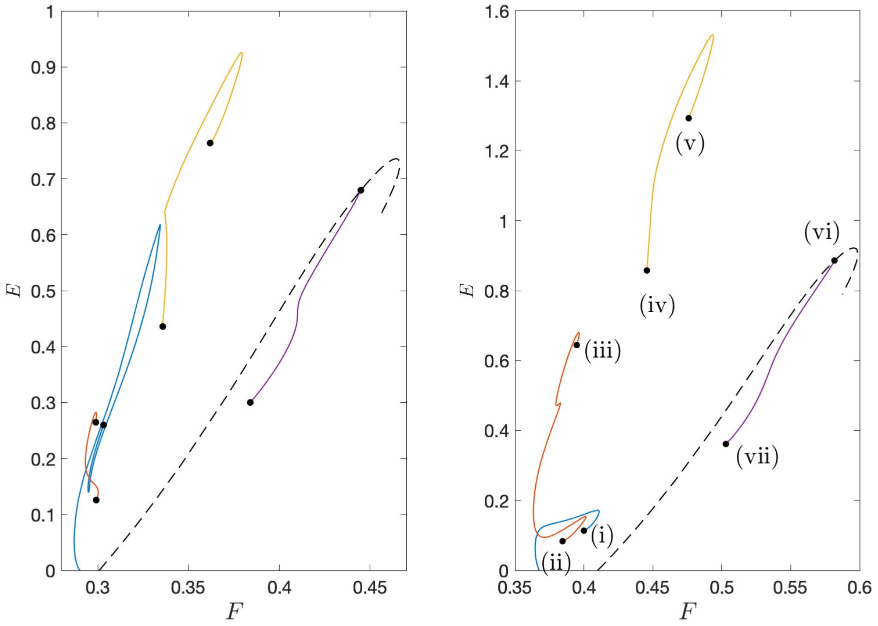

Figure 6.11: Left: Speed-energy bifurcation curves of the mode-2 waves with $R_1 = 1.3$, $R_3 = 0.7$, $h_1 = 1$, $h_3 = 1$, and $k = 1$. Right: Speed-energy bifurcation curves of the mode-2 waves with $R_1 = 1.5$, $R_3 = 0.5$, $h_1 = 1$, $h_3 = 1$, and $k = 1$. The black dashed curve is the bifurcation of the mode-1 waves with the same parameters except $k = 2$. The corresponding energy is calculated in two spatial periods.

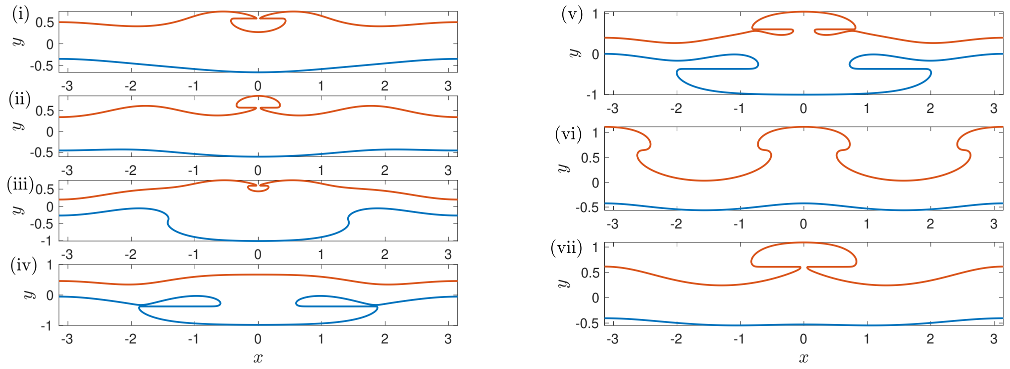

(a)

(b)

Figure 6.12: Almost limiting wave profiles corresponding to the labelled solutions (i) to (vii) in figure 6.11.

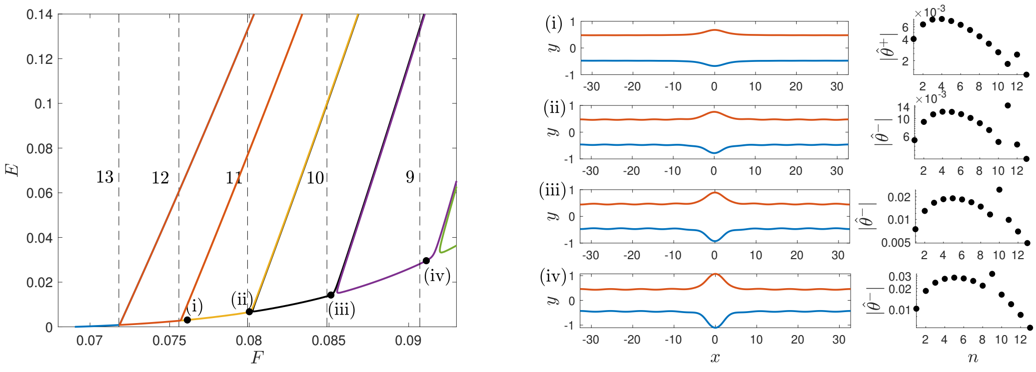

(a) (b)

Figure 6.13: (a) Speed-energy bifurcation curves for $R_1 = 1.01$, $R_3 = 0.99$, $h_1 = 50$, $h_3 = 50$, and $k = 0.096$. The vertical dashed lines denote the predicted value of F where the mode-2 waves are resonant with the mode-1 waves having waves number nk. The corresponding values of n are shown close to the vertical lines. (b) Typical wave profiles and related absolute value of one of $\widehat{\theta}^{\pm}$ of the labelled solutions (i) to (iv) in (a), where $\widehat{\theta}^-$ and $\widehat{\theta}^+$ are the Fourier coefficients of the inclination angle of the lower and upper interface.

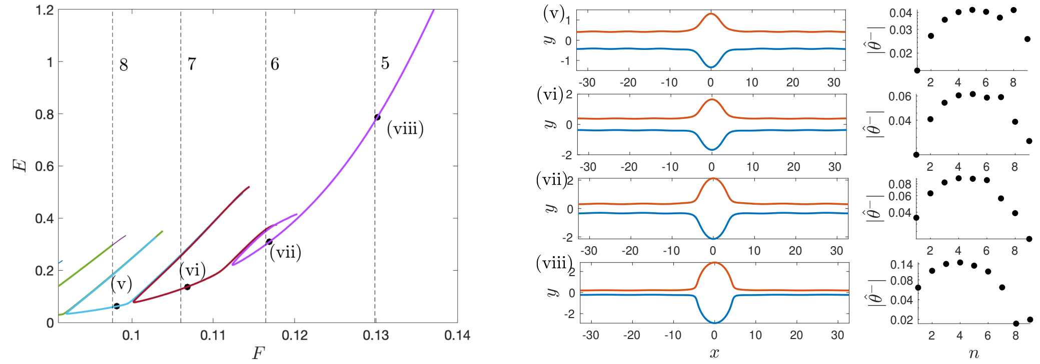

(a) (b)

Figure 6.14: (a) Continuation of figure 6.13(a). (b) Typical wave profiles and related absolute value of $\widehat{\theta}^-$ of the labelled solutions (v) to (viii) in (a).

the bifurcation structure becomes even more complex since there emerge a number of new resonant pairs. In figure 6.13, 6.14 and 6.15, we exhibit the numerical solutions for $R_1 = 1.01$, $R_3 = 0.99$, $h_1 = 1$, $h_3 = 1$, and $k = 0.096$. According to the linear theory, we can predict the critical values of F at which the mode-resonance occurs

$$F = c_{p1}(nk), \quad n \text{ is a positive integer},$$

where $c_{p1}(k)$ is the phase velocity of the mode-1 waves with wavenumber k. In figure 6.13(a), five critical values of F corresponding to $n = 9$ to 13 are shown by the five vertical dashed lines. To show the existence of the resonant mode-1 component, we select four typical solutions in the region close to the predicted critical values of F, display their profiles, as well as the corresponding $|\widehat{\theta}^{\pm}|$ in a log-scale, where $\widehat{\theta}^{\pm}$ are the Fourier coefficients of the inclination angles of the upper and lower interfaces. It is interesting to note that this prediction gives fairly good agreement to the numerical results. More importantly, it indicates that close to these critical values there are new bifurcation branches. Therefore, the bifurcation structure is like a comb. Every branch has a part that belongs to the almost symmetric branch, and the symmetry-breaking part becomes a tooth of the comb at some turning points close to the predicted critical values of F. The second part of the whole bifurcation is shown in figure 6.14 as well as the four predicted critical values of F corresponding to $n = 5$ to 8. As can been clearly seen, the positions of these turning points gradually differ from the predictions when waves become nonlinear, and the solutions gradually develop profiles of typical mode-2 generalised solitary wave type. The $|\widehat{\theta}^{-}|$ plot does not clearly show the resonant mode-1 component since more Fourier modes come into play.

If we follow different comb-teeth bifurcation curves and let the energy increase, then the wave profiles could develop rather different limiting configurations. In figure 6.15, we show six typical highly nonlinear solutions following those branches shown

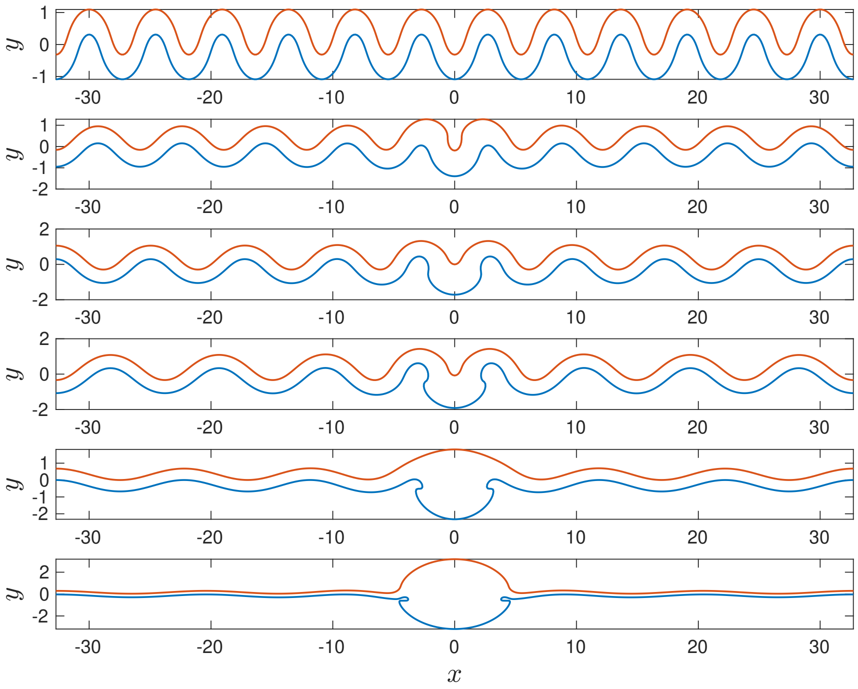

Figure 6.15: Six different (almost) limiting wave profiles with $R_1 = 1.01$, $R_3 = 0.99$, $h_1 = 50$, $h_3 = 50$, and $k = 0.096$.

in figure 6.13 and 6.14. From top to bottom, these solutions come from the $(1, 12)$, $(1, 10)$, $(1, 9)$, $(1, 8)$, $(1, 7)$ resonance teeth, and the rightmost almost symmetric branch in figure 6.14, i.e. the lower magenta branch. It turns out solutions could become pure mode-1 waves as shown in the top figure, or the long mode-1 waves with a distorted midsection and periodic mode-1 tails shown in the middle three figures, or the long mode-2 waves with periodic mode-1 tails shown in the bottom two figures.

Figure 6.16 shows bifurcation curves for $R_1 = 1.01, R_3 = 0.99, h_1 = h_3 = 0.1$, and $k = 0.1$. Here, the middle-layer is deep relative to the upper and lower layer, and the wave is relatively long. The main central pules of the resonant mode-2 waves in this case are found to be concave (that is, the upper interface is of depression, and the lower is of elevation). Note that in this case, the branches are found to cross the linear long-wave speed of mode-1, which for these parameters is given by $F \approx 0.0316$. This feature was also observed for mode-2 solitary waves [8, 27], and indeed when the

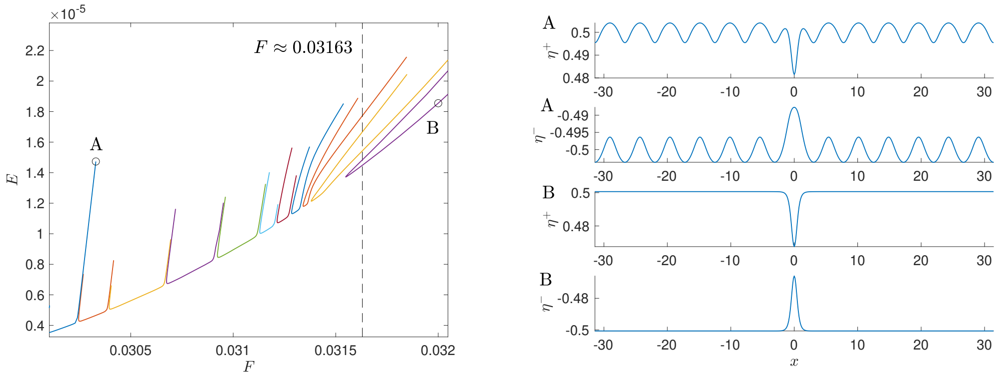

(a) (b)

Figure 6.16: (a) Speed-energy bifurcations of mode-2 waves with $R_1 = 1.01, R_3 = 0.99, h_1 = h_3 = 0.1$, and $k = 0.1$. The black dashed line represents the max phase speed of mode-1 waves. (b) Solutions A and B labelled in (a).

magenta branch exits the linear spectrum, the resulting solutions are true mode-2 solitary waves with no resonances (solution B in the figure). Although linear waves do not exist for speeds $F > 0.0316$, nonlinear mode-1 solitary and periodic waves do, and the other branches which exit the spectrum still have resonances with nonlinear mode-1 waves.

When $R_1 - 1 \neq 1 - R_3$, there exists a kind of "trapped waves" solution as shown by the typical solutions in figure 6.17. The related parameters are $R_1 = 1.01$, $R_3 = 0.95$, $h_1 = 1$, $h_3 = 1$, and $k = 1$. According to the dispersion relation, a $(1, 7)$ resonance exists when $k \approx 0.98472$. This explains the profile in figure (i) where seven oscillations are generated on the top interface in one spatial period. Surprisingly, there appears only one single wave on the lower interface. These waves are very similar to those previously obtained by [50] and [19]. When the amplitude of the lower interface gradually increases, it develops a bell-shaped profile and the oscillations on the upper interface gathered in the region above the trough of the lower interface. It is worth mentioning that similar solutions have been previously discovered in [51] experimentally and in [27] numerically. Figures (iii) and (iv) show that the waves could become even more nonlinear so that the upper interface develops an overhanging profile and tends to become self-intersecting. One or several closed

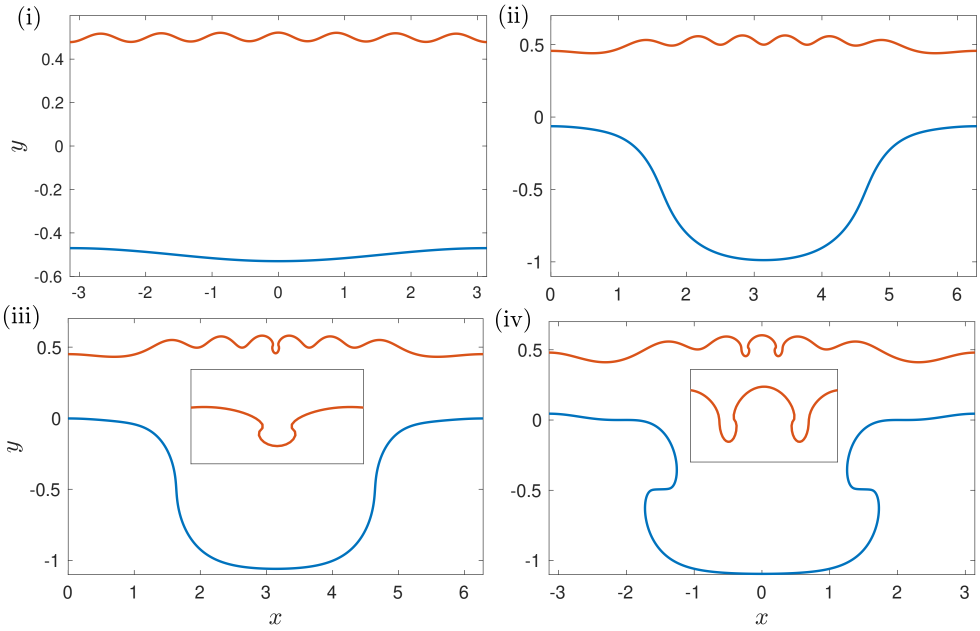

Figure 6.17: Four typical wave profiles with $R_1 = 1.01$, $R_3 = 0.95$, $h_1 = 1$, $h_3 = 1$, and $k = 1$.

bubbles are almost formed for solutions on different bifurcation branches. These overhanging structures are locally similar to those profiles shown before, except that the bubble size is greatly decreased. The lower interface also becomes steep and even overhanging. If the value of R_3 is further decreased to zero, then the three-layer model approaches an “air-water-water” setting. In this case, there are even more tiny oscillations on the upper interface and a large amplitude internal wave on the lower interface, which is a rough approximation of the real “surface-internal waves” oceanic scenario.

6.5 Conclusions

In this section, we present numerical calculations of periodic interfacial gravity waves in a three-layer fluid system. We assume that each layer has a finite depth and constant density, and impose two rigid lid conditions at the bottom and top (see figure 6.1). Density constants have non-increasing values from the bottom layer to top layer to ensure a statically stable configuration. Travelling wave solutions are calculated in a moving frame of reference where waves are steady. Using the analyticity of the complex velocity, we obtain four boundary integral equations from the Cauchy's integral formula. Together with the Bernoulli equations and several other constraints imposed on the two interfaces, a nonlinear algebraic system is obtained and solved via Newton's iteration. To achieve a high numerical accuracy, we apply the Fourier series technique. By setting the parameters to get an essentially two-layer deep water solution, we compare the wave speed for different given wave heights with other authors' results and find an 8-decimal-places accuracy. Using this algorithm, we explore the mode-1 and mode-2 wave solutions and find fruitful bifurcation structures. For clarity, we mainly focus on the weak stratification case for which the Boussinesq approximation is suited. Under this approximation, exactly symmetric solutions, which are invariant under the upside-down transformation, are found to form a symmetric solution branch. However, asymmetric solutions can coexist and their bifurcations connect to this symmetric branch. On the other hand, without using the Boussinesq assumption, solution branches are of a different nature, namely they are separated rather than connected (see figure 6.3), a sign of an imperfect bifurcation. For mode-1 waves, we observe one symmetry breaking bifurcation, whereas for mode-2 waves we observe two. Limiting waves which are located at the endpoint of each branch show similar bubble-crest structure to those found in two-layer interfacial gravity waves. For mode-2 waves, more bifurcations and other possibilities of limiting waves are found. Among them, a mode-resonance mechanism is particularly interesting. Roughly speaking, this is similar to the well-known "Wilton ripple" phenomenon in capillary-gravity waves. When the resonance condition (6.53) is satisfied, wave profiles can display a hybrid character of mode-1 and mode-2 waves because these modes have the same phase speed and thus coexist. Due to this mechanism, bifurcations can connect waves of different modes which results in a far more complicated structure than that of mode-1 waves (see figure 6.9 for example). When density ratios are gradually changed and beyond the weak stratification region, we observe the separation of bifurcation curves that are gathered initially, as well as the distortion of related wave profiles (see figure 6.12 and 6.17) . When we decrease the wave number to get a long wave approximation of generalised solitary waves, we find the comb-shaped bifurcation structure (figure 6.13 and 6.14). Following each tooth of the comb, we get generalised solitary waves having different numbers of periodic mode-1 tails. Surprisingly, these numbers can be well predicted by the resonant condition (6.53).

From a physical perspective, any finite-amplitude interfacial gravity wave suffers from the Kelvin-Helmholtz (K-H) instability, making the layered-Euler equations mathematically ill-posed for time evolution. Without regularizing effects, the instability grows unboundedly fast as the wavenumber increases. However, in real two-layer fluid configurations or fluids with a continuous sharp density stratification, the K-H instability can be suppressed by the stratification profile or other effects, preventing the breakdown of large-scale wave motion [21]. Therefore, we can expect that stable solutions exist in long-wave region [22]. Recently, [17] observed stable mode-2 waves in their laboratory experiments. Some of the waves are very similar to our numerical solutions (solution (i) in figure 6.5(c) and those in figure 6.13 and 6.14). In addition, the experiments performed by [51] suggest that waves (i) and (ii) shown in figure 6.17 may be stable.

Chapter 7

Future work

In the previous chapters, we have only presented the numerical method and the results for traveling waves. Therefore, a natural question is the stability of these waves. This gives rise to several future plans to extend the current work and will be completed in two steps: (1) designing a boundary-integral algorithm for unsteady interfacial waves; (2) performing the linear stability analysis for the travelling waves. Some preliminary results in this chapter can be found in Guan and Vanden-Broeck [34].

7.1 Time-dependent algorithm

We have shown that the boundary-integral method based on Cauchy's integral formula and arclength parameterization is an excellent approach to calculate nonlinear travelling interfacial waves. We want to extend the idea to unsteady waves. Since the governing equation will still be Laplace equation, we can inherit the methodology used previously by using the complex variable ζ

$$\zeta = \mathrm{e}^{-\mathrm{i}kz}, \tag{7.1}$$

and write the Cauchy's integral

$$w_i(\zeta_0) = \frac{1}{\mathrm{i}\pi} \oint_{C_i} \frac{w_i(\zeta)}{\zeta - \zeta_0} \, \mathrm{d}\zeta. \tag{7.2}$$

In general, the interface is no longer a streamline. As a result, equation (2.29) needs to be extended to include the normal velocity $\mathcal{N}_i$

$$w_i = (q_i - \mathrm{i}\mathcal{N}_i)\mathrm{e}^{-\mathrm{i}\theta}. \tag{7.3}$$

Hereafter we drop off the subscript of $\mathcal{N}_i$ because normal velocity is continuous across the interface. Substituting (7.3) into the Cauchy's integral and separating its real part and imaginary part, we have four real-valued equations

$$\mathcal{N}(s_0) = \int_0^S \Big(\mathcal{A}(s_0, s) - \mathcal{B}(s_0, s)\Big) q_1(s) \, \mathrm{d}s + \int_0^S \Big(\mathcal{C}(s_0, s) + \mathcal{D}(s_0, s)\Big) \mathcal{N}(s) \, \mathrm{d}s, \tag{7.4}$$

$$\mathcal{N}(s_0) = \int_0^S \Big(\mathcal{B}(s_0, s) - \mathcal{E}(s_0, s)\Big) q_2(s) \, \mathrm{d}s - \int_0^S \Big(\mathcal{D}(s_0, s) + \mathcal{F}(s_0, s)\Big) \mathcal{N}(s) \, \mathrm{d}s, \tag{7.5}$$

$$q_1(s_0) = \int_0^S \Big(\mathcal{D}(s_0, s) - \mathcal{C}(s_0, s)\Big) q_1(s) \, \mathrm{d}s + \int_0^S \Big(\mathcal{A}(s_0, s) + \mathcal{B}(s_0, s)\Big) \mathcal{N}(s) \, \mathrm{d}s, \tag{7.6}$$

$$q_2(s_0) = \int_0^S \Big(\mathcal{F}(s_0, s) - \mathcal{D}(s_0, s)\Big) q_2(s) \, \mathrm{d}s - \int_0^S \Big(\mathcal{B}(s_0, s) + \mathcal{E}(s_0, s)\Big) \mathcal{N}(s) \, \mathrm{d}s, \tag{7.7}$$

where S denotes the total arclength in a spatial period, and functions $\mathcal{A}(s_0, s)$ to $\mathcal{F}(s_0, s)$ are

$$\mathcal{A}(s_0, s) = \frac{k}{\pi} \mathrm{Im}\left(\frac{\mathrm{e}^{\mathrm{i}\theta(s_0)} \mathrm{e}^{-2kh_1}/\zeta^*(s)}{\mathrm{e}^{-2kh_1}/\zeta^*(s) - \zeta(s_0)} \right), \qquad \mathcal{B}(s_0, s) = \frac{k}{\pi} \mathrm{Im}\left(\frac{\mathrm{e}^{\mathrm{i}\theta(s_0)} \zeta(s)}{\zeta(s) - \zeta(s_0)} \right), \tag{7.8}$$

$$\mathcal{C}(s_0, s) = \frac{k}{\pi}\mathrm{Re}\left(\frac{\mathrm{e}^{\mathrm{i}\theta(s_0)}\mathrm{e}^{-2kh_1}/\zeta^*(s)}{\mathrm{e}^{-2kh_1}/\zeta^*(s) - \zeta(s_0)}\right), \qquad \mathcal{D}(s_0, s) = \frac{k}{\pi}\mathrm{Re}\left(\frac{\mathrm{e}^{\mathrm{i}\theta(s_0)}\zeta(s)}{\zeta(s) - \zeta(s_0)}\right), \tag{7.9}$$

$$\mathcal{E}(s_0, s) = \frac{k}{\pi}\mathrm{Im}\left(\frac{\mathrm{e}^{\mathrm{i}\theta(s_0)}/\zeta^*(s)}{1/\zeta^*(s) - \zeta(s_0)/\mathrm{e}^{2kh_2}}\right), \qquad \mathcal{F}(s_0, s) = \frac{k}{\pi}\mathrm{Re}\left(\frac{\mathrm{e}^{\mathrm{i}\theta(s_0)}/\zeta^*(s)}{1/\zeta^*(s) - \zeta(s_0)/\mathrm{e}^{2kh_2}}\right), \tag{7.10}$$

where Re and Im denote the real and imaginary parts, $\zeta^*(s)$ is the complex conjugate of $\zeta(s)$, and $h_{1,2}$ represents depths of the lower and upper layers. Since the dynamic boundary condition

$$(\rho_1\phi_1 - \rho_2\phi_2)_t + \frac{\rho_1}{2}|\nabla\phi_1|^2 - \frac{\rho_2}{2}|\nabla\phi_2|^2 + (\rho_1 - \rho_2)g\eta - \sigma\kappa = 0 \tag{7.11}$$

is a natural evolution equation for variable $\rho_1\phi_1 - \rho_2\phi_2$, we rewrite the boundary-integral equations using variable $\rho_1 q_1 - \rho_2 q_2$. For convenience, we introduce

$$\mathcal{T} := \rho_1 q_1 - \rho_2 q_2, \qquad \mathcal{U} := q_1 + q_2. \tag{7.12}$$

The resulting boundary-integral equations in terms of $\mathcal{T}$, $\mathcal{U}$ and $\mathcal{N}$ become

$$\begin{pmatrix} I - \frac{\mathcal{F} - R\mathcal{C} - (1-R)\mathcal{D}}{1+R}\Delta s & (\mathcal{E} - \mathcal{A})\Delta s \\ \frac{R(\mathcal{E} - \mathcal{A})}{(1+R)^2}\Delta s & I - \frac{\mathcal{C} - R\mathcal{F} + (1-R)\mathcal{D}}{1+R}\Delta s \end{pmatrix} \cdot \begin{pmatrix} \mathcal{U} \\ \mathcal{N} \end{pmatrix} = \begin{pmatrix} \frac{2\mathcal{D} - \mathcal{C} - \mathcal{F}}{1+R} \cdot \mathcal{T} \\ \frac{\mathcal{A} + R\mathcal{E}}{(1+R)^2} \cdot \mathcal{T} - \frac{\mathcal{B}}{1+R} \cdot \mathcal{T} - \frac{\partial\mathcal{T}/\partial s}{\pi(1+R)} \end{pmatrix} \Delta s, \tag{7.13}$$

where $R = \rho_2/\rho_1$, I denotes the identity matrix, and Δs is the spatial step after being discretized. Given the value of $\mathcal{T}$, we can solve $\mathcal{N}$ and $\mathcal{U}$, and obtain q_1 and q_2.

To do time integration, we can use the formulation in terms of the tangent angle

θ and infinitesimal arclength δs (see Yang [84] and Hou et al. [42])

$$\frac{D\theta}{Dt} = \mathcal{N}_s + \theta_s q_i, \tag{7.14}$$

$$\frac{D\delta s}{Dt} = (q_{i,s} - \theta_s \mathcal{N})\delta s. \tag{7.15}$$

From (7.15), we can get the evolution equation for total arclength S

$$\frac{\mathrm{d}S}{\mathrm{d}t} = -\int_0^S \theta_s \mathcal{N} \,\mathrm{d}s, \tag{7.16}$$

where the periodicity of q_i has been used. The material derivative can be written as

$$\frac{D}{Dt} = \frac{\partial}{\partial t} + \frac{Ds}{Dt}\frac{\partial}{\partial s}, \tag{7.17}$$

where

$$\frac{Ds}{Dt} = \int_0^s (q_{i,s} - \theta_s \mathcal{N}) \,\mathrm{d}s = q_i(s,t) - q_i(0,t) - \int_0^s \theta_s \mathcal{N} \,\mathrm{d}s. \tag{7.18}$$

Introducing $\varphi = \rho_1\phi_1(x,\eta,t) - \rho_2\phi_2(x,\eta,t)$, we can derive its governing equation from the dynamic boundary condition

$$\varphi_t = q_1(0,t)\mathcal{T} + \frac{1}{2}(\rho_1 - \rho_2)\mathcal{N}^2 - \frac{1}{2}(\rho_1 q_1^2 - \rho_2 q_2^2) + \mathcal{T}\int_0^s \theta_s \mathcal{N} \,\mathrm{d}s - (\rho_1 - \rho_2)g\eta + \sigma\theta_s, \tag{7.19}$$

where the relation between $\mathcal{T}$ and φ is

$$\mathcal{T} = \varphi_s. \tag{7.20}$$

Thus, we obtain a time-marching algorithm for interfacial waves. Given initial conditions for θ, φ and S, we can simulate their time evolution.

In the future, this formulation will be used to study the time-evolution of travelling waves obtained previously. It will also be extended to more complex scenarios, such as jet flows in three-layer flows, interfacial waves interacting with electric fields, surface/interfacial waves over bottom topography, surface waves interacting with floating objects, etc.

7.2 Linear stability analysis

7.2.1 Formulation from Calvo and Akylas

Akylas and Calvo [15] have presented a method to perform linear stability of interfacial solitary waves. They consider the following perturbations superposed on the steady solutions $\eta(x)$, $\Phi_i(x,y)$ and $\Psi_i(x,y)(i=1,2)$ in the moving frame of reference, where Ψ_i are the stream functions in each layer

$$\eta(x,t) \to \eta(x) + \mathrm{e}^{\lambda t}\widetilde{\eta}(x), \tag{7.21}$$

$$\phi_1(x,y,t) \to \Phi_1(x,y) + \mathrm{e}^{\lambda t}\widetilde{\phi}_1(x,y), \quad \psi_1(x,y,t) \to \Psi_1(x,y) + \mathrm{e}^{\lambda t}\widetilde{\psi}_1(x,y), \tag{7.22}$$

$$\phi_2(x,y,t) \to \Phi_2(x,y) + \mathrm{e}^{\lambda t}\widetilde{\phi}_2(x,y), \quad \psi_2(x,y,t) \to \Psi_2(x,y) + \mathrm{e}^{\lambda t}\widetilde{\psi}_2(x,y), \tag{7.23}$$

where the tiled terms represent small perturbations. After linearizing the kinematic boundary condition and the dynamic boundary condition, they obtained

$$\lambda\widetilde{\eta} = -\frac{1}{\cos\theta}\frac{\mathrm{d}\mathcal{P}_1(\widetilde{\phi}_1)}{\mathrm{d}s} - \frac{1}{\cos\theta}\frac{\mathrm{d}}{\mathrm{d}s}(q_1\cos\theta)\widetilde{\eta} - q_1\frac{\mathrm{d}\widetilde{\eta}}{\mathrm{d}s}, \tag{7.24}$$

$$\lambda\widetilde{\eta} = -\frac{1}{\cos\theta}\frac{\mathrm{d}\mathcal{P}_2(\widetilde{\phi}_2)}{\mathrm{d}s} - \frac{1}{\cos\theta}\frac{\mathrm{d}}{\mathrm{d}s}(q_2\cos\theta)\widetilde{\eta} - q_2\frac{\mathrm{d}\widetilde{\eta}}{\mathrm{d}s}, \tag{7.25}$$

$$\begin{aligned}\lambda(\widetilde{\phi}_1 - R\widetilde{\phi}_2) =& - q_1\frac{\mathrm{d}\widetilde{\phi}_1}{\mathrm{d}s} + Rq_2\frac{\mathrm{d}\widetilde{\phi}_2}{\mathrm{d}s} - \left(q_1\frac{\mathrm{d}(q_1\sin\theta)}{\mathrm{d}s} - Rq_2\frac{\mathrm{d}(q_2\sin\theta)}{\mathrm{d}s} + 1 - R\right)\widetilde{\eta} \\ &+ \frac{1}{\cos\theta}\frac{\mathrm{d}}{\mathrm{d}s}\left(\cos^2\theta\frac{\mathrm{d}\widetilde{\eta}}{\mathrm{d}s}\right),\end{aligned} \tag{7.26}$$

where $\mathcal{P}_1$ and $\mathcal{P}_2$ are operators relating $\widetilde{\phi}_{1,2}$ and $\widetilde{\psi}_{1,2}$ and can be found from Cauchy's integral formula. This leads to a generalised eigenvalue problem

$$\begin{pmatrix} M_1 & M_2 & 0 \\ M_3 & 0 & M_4 \\ M_5 & M_6 & M_7 \end{pmatrix} \begin{pmatrix} \widetilde{\eta} \\ \widetilde{\phi}_1 \\ \widetilde{\phi}_2 \end{pmatrix} = \lambda \begin{pmatrix} I & 0 & 0 \\ I & 0 & 0 \\ 0 & I & -RI \end{pmatrix} \begin{pmatrix} \widetilde{\eta} \\ \widetilde{\phi}_1 \\ \widetilde{\phi}_2 \end{pmatrix} \tag{7.27}$$

where 0 and I represent the zero and identity matrices. Although it can be solved by the built-in Matlab function eig, we found this is rather time-consuming and numerically sensitive. Therefore, we derive a new formulation to perform the linear stability analysis.

7.2.2 New formulation

Motivated by the time-marching algorithm, we introduce two variables $\widetilde{\xi}$ and $\widetilde{\chi}$

$$\widetilde{\xi} := \widetilde{\phi}_1 - R\widetilde{\phi}_2, \qquad \widetilde{\chi} := \widetilde{\phi}_1 + \widetilde{\phi}_2 \tag{7.28}$$

$\widetilde{\phi}_1$ and $\widetilde{\phi}_2$ can be obtained from the following two relations

$$\widetilde{\phi}_1 = \frac{\widetilde{\xi} + R\widetilde{\chi}}{1+R}, \qquad \widetilde{\phi}_2 = \frac{\widetilde{\chi} - \widetilde{\xi}}{1+R}, \tag{7.29}$$

Replacing w_i by $\widetilde{\phi}_i + \mathrm{i}\widetilde{\psi}_i$, we have

$$\widetilde{\phi}_1 = -\mathcal{M}_r\widetilde{\psi}_1 - \mathcal{M}_i\widetilde{\phi}_1, \tag{7.30}$$

$$\widetilde{\phi}_2 = \mathcal{M}_r\widetilde{\psi}_2 + \mathcal{M}_i\widetilde{\phi}_2, \tag{7.31}$$

where $\mathcal{M}_r$ and $\mathcal{M}_i$ represent the real and imaginary part of the boundary-integral operator. Adding them together, we have

$$\widetilde{\chi} = -\mathcal{M}_r(\widetilde{\psi}_1 - \widetilde{\psi}_2) - \mathcal{M}_i\widetilde{\phi}_1 + \mathcal{M}_i\widetilde{\phi}_2. \tag{7.32}$$

The following identity is implied by subtracting (7.24) and (7.25)

$$\widetilde{\psi}_1 - \widetilde{\psi}_2 = \widetilde{\eta}(q_2 - q_1)\cos\theta. \tag{7.33}$$

Thus (7.32) becomes

$$\widetilde{\chi} = -\mathcal{M}_r\Big(\widetilde{\eta}(q_2 - q_1)\cos\theta\Big) - \mathcal{M}_i\widetilde{\phi}_1 + \mathcal{M}_i\widetilde{\phi}_2. \tag{7.34}$$

Replacing $\widetilde{\phi}_1$ and $\widetilde{\phi}_2$ by $\widetilde{\xi}$ and $\widetilde{\chi}$, we obtain

$$\Big(I + \frac{(R-1)\mathcal{M}_i}{1+R}\Big)\widetilde{\chi} = -\mathcal{M}_r\Big(\widetilde{\eta}(q_2 - q_1)\cos\theta\Big) - \frac{2\mathcal{M}_i}{1+R}\widetilde{\xi}, \tag{7.35}$$

or in a more compact form

$$\widetilde{\chi} = \mathcal{Q}_1\widetilde{\eta} + \mathcal{Q}_2\widetilde{\xi}. \tag{7.36}$$

Now we can rewrite the kinematic boundary condition and dynamic boundary condition

- For (7.24)

$$\begin{aligned}\lambda\widetilde{\eta} &= -\frac{1}{\cos\theta}\frac{\mathrm{d}}{\mathrm{d}s}\Big(\mathcal{P}_1(\widetilde{\phi}_1) + \widetilde{\eta}q_1\cos\theta\Big) = -\frac{1}{\cos\theta}\frac{\mathrm{d}}{\mathrm{d}s}\Big(\frac{\mathcal{P}_1\widetilde{\xi} + R\mathcal{P}_1\widetilde{\chi}}{1+R} + \widetilde{\eta}q_1\cos\theta\Big)\\ &= -\frac{1}{\cos\theta}\frac{1}{1+R}\frac{\mathrm{d}}{\mathrm{d}s}(\mathcal{P}_1\widetilde{\xi}) - \frac{1}{\cos\theta}\frac{R}{1+R}\frac{\mathrm{d}}{\mathrm{d}s}(\mathcal{P}_1\mathcal{Q}_1\widetilde{\eta} + \mathcal{P}_1\mathcal{Q}_2\widetilde{\xi}) - \frac{1}{\cos\theta}\frac{\mathrm{d}}{\mathrm{d}s}(\widetilde{\eta}q_1\cos\theta).\end{aligned} \tag{7.37}$$

- For (7.26), the kinetic energy term becomes

$$
\begin{aligned}
-q_1\frac{\mathrm{d}\widetilde{\phi}_1}{\mathrm{d}s}+Rq_2\frac{\mathrm{d}\widetilde{\phi}_2}{\mathrm{d}s} &= -\,q_1\frac{\mathrm{d}}{\mathrm{d}s}\left(\frac{\widetilde{\xi}+R\widetilde{\chi}}{1+R}\right)+Rq_2\frac{\mathrm{d}}{\mathrm{d}s}\left(\frac{\widetilde{\chi}-\widetilde{\xi}}{1+R}\right)\\
&= -\,\frac{q_1+Rq_2}{1+R}\frac{\mathrm{d}\widetilde{\xi}}{\mathrm{d}s}-\frac{R(q_1-q_2)}{1+R}\frac{\mathrm{d}}{\mathrm{d}s}(\mathcal{Q}_1\widetilde{\eta}+\mathcal{Q}_2\widetilde{\xi}). \qquad (7.38)
\end{aligned}
$$

So (7.26) becomes

$$
\begin{aligned}
\lambda\widetilde{\xi} = &-\frac{q_1+Rq_2}{1+R}\frac{\mathrm{d}\widetilde{\xi}}{\mathrm{d}s}-\frac{R(q_1-q_2)}{1+R}\frac{\mathrm{d}}{\mathrm{d}s}(\mathcal{Q}_1\widetilde{\eta}+\mathcal{Q}_2\widetilde{\xi}),\\
&-\left(q_1\frac{\mathrm{d}(q_1\sin\theta)}{\mathrm{d}s}-Rq_2\frac{\mathrm{d}(q_2\sin\theta)}{\mathrm{d}s}+1-R\right)\widetilde{\eta}+\frac{1}{\cos\theta}\frac{\mathrm{d}}{\mathrm{d}s}\left(\cos^2\theta\frac{\mathrm{d}\widetilde{\eta}}{\mathrm{d}s}\right).
\end{aligned}
\qquad (7.39)
$$

Ultimately, we have

$$
\lambda\widetilde{\eta} = -\,\frac{1}{\cos\theta}\frac{\mathrm{d}}{\mathrm{d}s}\left(\frac{\mathcal{P}_1+R\mathcal{P}_1\mathcal{Q}_2}{1+R}\widetilde{\xi}\right)-\frac{1}{\cos\theta}\frac{\mathrm{d}}{\mathrm{d}s}\left(\widetilde{\eta}q_1\cos\theta\right)-\frac{1}{\cos\theta}\frac{\mathrm{d}}{\mathrm{d}s}\left(\frac{R\mathcal{P}_1\mathcal{Q}_1\widetilde{\eta}}{1+R}\right) \qquad (7.40)
$$

$$
\begin{aligned}
\lambda\widetilde{\xi} = &-\frac{q_1+Rq_2}{1+R}\frac{\mathrm{d}\widetilde{\xi}}{\mathrm{d}s}-\frac{R(q_1-q_2)}{1+R}\frac{\mathrm{d}\mathcal{Q}_2(\widetilde{\xi})}{\mathrm{d}s}-\left(q_1\frac{\mathrm{d}(q_1\sin\theta)}{\mathrm{d}s}-Rq_2\frac{\mathrm{d}(q_2\sin\theta)}{\mathrm{d}s}+1-R\right)\widetilde{\eta}\\
&+\frac{1}{\cos\theta}\frac{\mathrm{d}}{\mathrm{d}s}\left(\cos^2\theta\frac{\mathrm{d}\widetilde{\eta}}{\mathrm{d}s}\right)-\frac{R(q_1-q_2)}{1+R}\frac{\mathrm{d}\mathcal{Q}_1(\widetilde{\eta})}{\mathrm{d}s}
\end{aligned}
\qquad (7.41)
$$

This is an eigenvalue problem of standard form. When setting $R = 0$, it becomes the formulation in [14, 72]. Compared with equations (7.24)-(7.26), our formulation reduces the number of unknowns by a third and turns out to be more stable numerically.

In the future, this formulation will be used to study the linear stability of the travelling waves obtained previously. It still has a drawback that the solutions under consideration must be a function of x, i.e. the solutions can not be overhanging. However, we are interested in some overhanging solutions, such as the interfacial solitary waves obtained in chapter 3. As pointed in Nie et al. [60], these solutions may have connections to the droplet splashing observed in wave breaking. To address this issue, it is better to do the linearization directly from the time-dependent formulation, which will be done in future.

7.3 Preliminary results

In this section, we display some preliminary numerical results from the time-marching algorithm.

In figure 7.1, we show a simulation of breaking of gravity surface waves. The initial condition is a travelling Stokes wave whose spatial size is amplified three times. At the initial stage, gravitational potential energy is transferred to kinematic energy, resulting an accelerating moving front. At $t \approx 5.375$, the wave develops a vertical tangent and then becomes overhanging. A plunging breaker appears and becomes sharp at its tip. At $t = 7.725$, the wave becomes almost self-touching and encloses an air bubble on its front face. The nipple of the breaker has a locally round shape and tiny wiggles, which probably come from numerical oscillations due to the drastic increase of curvature. Higher resolutions are used to show that a gradually convergent solution can be obtained. A comparison of the wave profile at $t = 7.725$ with $N = 1024, 2048$ and 3072 is plotted on the bottom of Fig. 7.1(a).

In figure 7.2, we exhibit a simulation of the overhanging waves that we calculated in chapter 4. The parameter is $R = 0.5$, $k = 5$, $h_1 = h_2 = 1$. There is no background shear as we have explained in chapter 4 when introducing the definition of wave speed. However, since $q_1 \neq q_2$ on the interface, there is a wave-induced shear generally. It is thus expected such a solution is unstable due to the Kelvin-Helmholtz instability and Rayleigh-Taylor instability. It turns out Kelvin-Helmholtz mechanism dominates. In fact, what we have found is initial-value problem for nonlinear gravity waves is ill-posed. One has to introduce regularization either by using filer or including surface

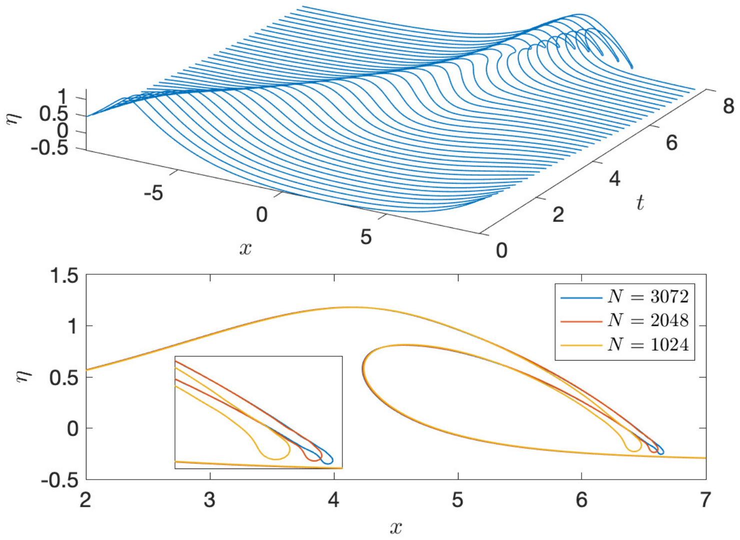

Figure 7.1: Top: breaking process of a gravity wave. Bottom: wave profile at $t = 7.725$ with $N = 1024, 2048$ and 3072.

tension or viscosity.

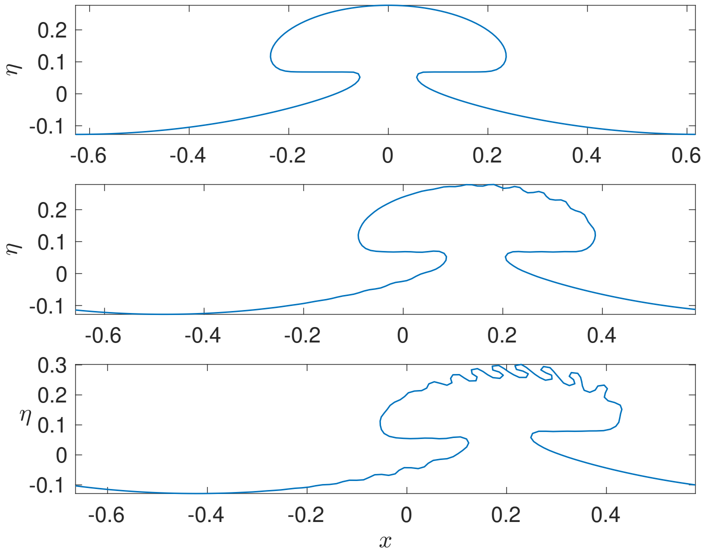

Figure 7.2: Evolution of an overhanging interfacial gravity wave.

Chapter 8

Final conclusions

In conclusion, we have presented novel interfacial travelling waves in various scenarios, including two-layer gravity waves of solitary type and periodic type, two-layer periodic capillary waves and three-layer periodic gravity waves. We have established an unified numerical scheme based on Cauchy's integral formula and Newton-Krylov method. Using the arclength parametrization, we are able to calculate fully nonlinear solutions following bifurcations until singularities almost appear, either by self-intersecting or boundary-touching. We focused on the limiting configuration proposed by Grimshaw and Pullin [30]. Our numerical simulations based on Euler equations and the simplified model have provided solid evidence for their conjecture, especially in small-density ratio case. For interfacial capillary waves and three-layer gravity waves, we have shown the existence of new limiting configurations. In addition, we also found an universal bifurcation mechanism due to symmetry breaking, for all types of interfacial waves. In the future, all the present work will be extended to the time-dependent case to study their stability. A time-marching algorithm based on a $\theta - s$ formulation has recently been developed by the author [34] and applied to the travelling-wave solution found in this thesis.

Bibliography

[1] B. F. Akers, D. M. Ambrose and J. D. Wright. Traveling waves from the arclength parameterization: Vortex sheets with surface tension. *Interfaces and Free Boundaries*, 15(3):359–380, 2013.

[2] B. F. Akers, D. M. Ambrose and J. D. Wright. Gravity perturbed crapper waves. *Proceedings of the Royal Society A: Mathematical, Physical and Engineering Sciences*, 470(2161):20130526, 2014.

[3] T. R. Akylas and R. Grimshaw. Solitary internal waves with oscillatory tails. *Journal of Fluid Mechanics*, 242:279–298, 1992.

[4] C. J. Amick, L. E. Fraenkel and J. F. Toland. On the Stokes conjecture for the wave of extreme form. 1982.

[5] C. J. Amick and R. E. L. Turner. A global theory of internal solitary waves in two-fluid systems. *Transactions of the American Mathematical Society*, 298(2):431–484, 1986.

[6] G. R. Baker, D. I. Meiron and S. A. Orszag. Generalized vortex methods for free-surface flow problems. *Journal of Fluid Mechanics*, 123:477–501, 1982.

[7] R. Barros and W. Choi. Holmboe instability in non-boussinesq fluids. *Physics of Fluids*, 23(12):124103, 2011.

[8] R. Barros, W. Choi and P. A. Milewski. Strongly nonlinear effects on internal solitary waves in three-layer flows. *Journal of Fluid Mechanics*, 883, 2020.

[9] T. B. Benjamin. Internal waves of permanent form in fluids of great depth. *Journal of Fluid Mechanics*, 29(3):559–592, 1967.

[10] T. B. Benjamin and T. J. Bridges. Reappraisal of the kelvin–helmholtz problem. part 2. interaction of the kelvin–helmholtz, superharmonic and benjamin–feir instabilities. *Journal of Fluid Mechanics*, 333:327–373, 1997.

[11] M. G. Blyth and E. I. Părău. The stability of capillary waves on fluid sheets. *Journal of Fluid Mechanics*, 806:5–34, 2016.

[12] M. G. Blyth and J.-M. Vanden-Broeck. New solutions for capillary waves on fluid sheets. *Journal of Fluid Mechanics*, 507:255–264, 2004.

[13] A. Boonkasame and P. Milewski. The stability of large-amplitude shallow interfacial non-boussinesq flows. *Studies in Applied Mathematics*, 128(1):40–58, 2012.

[14] D. C. Calvo and T. R. Akylas. Stability of steep gravity–capillary solitary waves in deep water. *Journal of Fluid Mechanics*, 452:123–143, 2002.

[15] D. C. Calvo and T. R. Akylas. On interfacial gravity-capillary solitary waves of the benjamin type and their stability. *Physics of Fluids*, 15(5):1261–1270, 2003.

[16] R. Camassa, S. Chen, G. Falqui, G. Ortenzi and M. Pedroni. An inertia ‘paradox’for incompressible stratified euler fluids. *Journal of Fluid Mechanics*, 695:330–340, 2012.

[17] M. Carr, P. A. Davies and R. P. Hoebers. Experiments on the structure and stability of mode-2 internal solitary-like waves propagating on an offset pycnocline. *Physics of Fluids*, 27(4), 2015.

[18] B. Chen and P. G. Saffman. Numerical evidence for the existence of new types of gravity waves of permanent form on deep water. *Studies in Applied Mathematics*, 62(1):1–21, 1980.

[19] M. J. Chen and L. K. Forbes. Steady periodic waves in a three-layer fluid with shear in the middle layer. *Journal of Fluid Mechanics*, 594:157–181, 2008.

[20] W. Choi and R. Camassa. Fully nonlinear internal waves in a two-fluid system. *Journal of Fluid Mechanics*, 396:1–36, 1999.

[21] L. Chumakova, F. E. Menzaque, P. A. Milewski, R. R. Rosales, E. G. Tabak

and C. V. Turner. Shear instability for stratified hydrostatic flows. *Comm. on Pure and Appl. Math.*, 62(2):183–197, 2009.

[22] L. Chumakova, F. E. Menzaque, P. A. Milewski, R. R. Rosales, E. G. Tabak and C. V. Turner. Stability properties and nonlinear mappings of two and three-layer stratified flows. *Studies in Applied Mathematics*, 122(2):123–137, 2009.

[23] G. D. Crapper. An exact solution for progressive capillary waves of arbitrary amplitude. *Journal of Fluid Mechanics*, 2(6):532–540, 1957.

[24] D. G. Crowdy. A new approach to free surface Euler flows with capillarity. *Studies in Applied Mathematics*, 105(1):35–58, 2000.

[25] D. Daboussy, F. Dias and J.-M. Vanden-Broeck. Gravity flows with a free surface of finite extent. *European Journal of Mechanics-B/Fluids*, 17(1):19–31, 1998.

[26] D. Deepwell, M. Stastna, M. Carr and P. A. Davies. Interaction of a mode-2 internal solitary wave with narrow isolated topography. *Physics of Fluids*, 29(7), 2017.

[27] A. Doak, R. Barros and P. A. Milewski. Large mode-2 internal solitary waves in three-layer flows. *Journal of Fluid Mechanics*, 953:A42, 2022.

[28] W. A. B. Evans and M. J. Ford. An integral equation approach to internal (2-layer) solitary waves. *Physics of Fluids*, 8(8):2032–2047, 1996.

[29] M. Funakoshi and M. Oikawa. Long internal waves of large amplitude in a two-layer fluid. *Journal of the Physical Society of Japan*, 55(1):128–144, 1986.

[30] R.H.J. Grimshaw and D.I. Pullin. Extreme interfacial waves. *Physics of Fluids*, 29(9):2802–2807, 1986.

[31] R. H. J. Grimshaw, E. Pelinovsky and T. Talipova. The modified korteweg-de vries equation in the theory of large-amplitude internal waves. *Nonlinear Processes in Geophysics*, 4(4):237–250, 1997.

[32] J. Grue, A. Jensen, P. O. Rusås and J. K. Sveen. Properties of large-amplitude internal waves. *Journal of Fluid Mechanics*, 380:257–278, 1999.

[33] X. Guan, A. Doak, P. Milewski and J.-M. Vanden-Broeck. Nonlinear travelling

periodic waves for the Euler equations in three-layer flows. *Journal of Fluid Mechanics*, 981:A12, 2024.

[34] X Guan and J.-M. Vanden-Broeck. A novel boundary-integral algorithm for nonlinear unsteady surface and interfacial waves. *arXiv preprint arXiv:2312.13019*, 2023.

[35] X Guan, J-M Vanden-Broeck and Z Wang. New solutions for periodic interfacial gravity waves. *Journal of Fluid Mechanics*, 928:R5, 2021.

[36] X. Guan, J.-M. Vanden-Broeck and Z. Wang. New solutions for interfacial capillary waves of permanent form. *Journal of Fluid Mechanics*, 951:A43, 2022.

[37] X. Guan, J.-M. Vanden-Broeck, Z. Wang and F. Dias. A local model for the limiting configuration of interfacial solitary waves. *Journal of Fluid Mechanics*, 921:A9, 2021.

[38] A. Guha and R. Raj. On the inertial effects of density variation in stratified shear flows. *Physics of Fluids*, 30(12), 2018.

[39] T. H. Havelock. Periodic irrotational waves of finite height. *Proceedings of the Royal Society of London. Series A, Containing Papers of a Mathematical and Physical Character*, 95(665):38–51, 1918.

[40] E. Heifetz and J. Mak. Stratified shear flow instabilities in the non-boussinesq regime. *Physics of Fluids*, 27(8), 2015.

[41] J. Y. Holyer. Large amplitude progressive interfacial waves. *Journal of Fluid Mechanics*, 93(3):433–448, 1979.

[42] T. Y. Hou, J. S. Lowengrub and M. J. Shelley. Removing the stiffness from interfacial flows with surface tension. *Journal of Computational Physics*, 114(2):312–338, 1994.

[43] J. K. Hunter and J.-M. Vanden-Broeck. Accurate computations for steep solitary waves. *Journal of fluid Mechanics*, 136:63–71, 1983.

[44] T.-C. Jo and Y.-K. Choi. Dynamics of strongly nonlinear internal long waves in a three-layer fluid system. *Ocean Science Journal*, 49(4):357–366, 2014.

[45] W. Kinnersley. Exact large amplitude capillary waves on sheets of fluid. *Journal of Fluid Mechanics*, 77(2):229–241, 1976.

[46] C. G. Koop and G. Butler. An investigation of internal solitary waves in a two-fluid system. *Journal of Fluid Mechanics*, 112:225–251, 1981.

[47] O. E. Kurkina, A. A. Kurkin, E. A. Rouvinskaya and T. Soomere. Propagation regimes of interfacial solitary waves in a three-layer fluid. *Nonlinear Processes in Geophysics*, 22(2):117–132, 2015.

[48] K. G. Lamb. Conjugate flows for a three-layer fluid. *Physics of Fluids*, 12(9):2169–2185, 2000.

[49] C. W. Lenau. The solitary wave of maximum amplitude. *Journal of Fluid Mechanics*, 26(2):309–320, 1966.

[50] J. E. Lewis, B. M. Lake and D. R. S. Ko. On the interaction of internal waves and surface gravity waves. *Journal of Fluid Mechanics*, 63(4):773–800, 1974.

[51] V. Yu. Liapidevskii and N. V. Gavrilov. Large internal solitary waves in shallow waters. In *The Ocean in Motion*, pages 87–108. Springer, 2018.

[52] M. S. Longuet-Higgins. On the form of the highest progressive and standing waves in deep water. *Proceedings of the Royal Society of London. A. Mathematical and Physical Sciences*, 331(1587):445–456, 1973.

[53] M. S. Longuet-Higgins and M. Tanaka. On the crest instabilities of steep surface waves. *Journal of Fluid Mechanics*, 336:51–68, 1997.

[54] D. V. Maklakov. A note on the existence of pure gravity waves at the interface of two fluids. *Physica D: Nonlinear Phenomena*, 401:132157, 2020.

[55] D. V. Maklakov and R. R. Sharipov. Almost limiting configurations of steady interfacial overhanging gravity waves. *Journal of Fluid Mechanics*, 856:673–708, 2018.

[56] D. I. Meiron and P. G. Saffman. Overhanging interfacial gravity waves of large amplitude. *Journal of Fluid Mechanics*, 129:213–218, 1983.

[57] W. K. Melville and K. R. Helfrich. Transcritical two-layer flow over topography.

Journal of Fluid Mechanics, 178:31–52, 1987.

[58] H. Michallet and E. Barthelemy. Experimental study of interfacial solitary waves. *Journal of Fluid Mechanics*, 366:159–177, 1998.

[59] M. Miyata. Long internal waves of large amplitude. pages 399–406. Springer, 1988.

[60] B. C. Nie, X. Guan, J.-M. Vanden-Broeck and F. Dias. Air/water interfacial waves with a droplet at the tip of their crest. *Physics of Fluids*, 35(1), 2023.

[61] H. Okamoto. *The mathematical theory of permanent progressive water-waves*, volume 20. World Scientific, 2001.

[62] H. Okamoto. Uniqueness of crapper's pure capillary waves of permanent shape. *Journal of Mathematical Sciences-University of Tokyo*, 12(1):67–76, 2005.

[63] H. Okamoto and M. Shoji. Nonexistence of bifurcation from crapper's pure capillary. , 745:21–38, 1991.

[64] H. Ono. Algebraic solitary waves in stratified fluids. *Journal of the Physical Society of Japan*, 39(4):1082–1091, 1975.

[65] E. Părău and F. Dias. Interfacial periodic waves of permanent form with free-surface boundary conditions. *Journal of Fluid Mechanics*, 437:325–336, 2001.

[66] R. Pethiyagoda, S. W. McCue, T. J. Moroney and J. M. Back. Jacobian-free newton–krylov methods with gpu acceleration for computing nonlinear ship wave patterns. *Journal of Computational Physics*, 269:297–313, 2014.

[67] D.I. Pullin and R. H. J. Grimshaw. Finite-amplitude solitary waves at the interface between two homogeneous fluids. *The Physics of fluids*, 31(12):3550–3559, 1988.

[68] P.-O Rusås. *On nonlinear internal waves in two- and three-layer fluids.* PhD thesis, University of Oslo, 2000.

[69] P.-O. Rusås and J. Grue. Solitary waves and conjugate flows in a three-layer fluid. *European Journal of Mechanics-B/Fluids*, 21(2):185–206, 2002.

[70] P. G. Saffman and H. C. Yuen. Finite-amplitude interfacial waves in the presence

of a current. *Journal of Fluid Mechanics*, 123:459–476, 1982.

[71] L. W. Schwartz. Computer extension and analytic continuation of stokes' expansion for gravity waves. *Journal of Fluid Mechanics*, 62(3):553–578, 1974.

[72] M. Tanaka. The stability of solitary waves. *The Physics of fluids*, 29(3):650–655, 1986.

[73] R. Tiron and W. Choi. Linear stability of finite-amplitude capillary waves on water of infinite depth. *Journal of fluid mechanics*, 696:402–422, 2012.

[74] L. N. Trefethen and D. Bau. *Numerical linear algebra*, volume 181. Siam, 2022.

[75] C. Ţugulan, O. Trichtchenko and E. Părău. Three-dimensional waves under ice computed with novel preconditioning methods. *Journal of Computational Physics*, 459:111129, 2022.

[76] R. E. L. Turner and J.-M. Vanden-Broeck. The limiting configuration of interfacial gravity waves. *The Physics of fluids*, 29(2):372–375, 1986.

[77] R. E. L. Turner and J.-M. Vanden-Broeck. Broadening of interfacial solitary waves. *The Physics of fluids*, 31(9):2486–2490, 1988.

[78] J.-M. Vanden-Broeck. *Gravity-capillary free-surface flows.* Cambridge University Press, 2010.

[79] J.-M. Vanden-Broeck and L. W. Schwartz. Numerical computation of steep gravity waves in shallow water. *The Physics of Fluids*, 22(10):1868–1871, 1979.

[80] V. Vasan and B. Deconinck. The bernoulli boundary condition for traveling water waves. *Applied Mathematics Letters*, 26(4):515–519, 2013.

[81] J. R. Wilton. On ripples. *The London, Edinburgh, and Dublin Philosophical Magazine and Journal of Science*, 29(173):688–700, 1915.

[82] H. Yamada. Highest waves of permanent type on the surface of deep water. *Research Institute for Applied Mechanics, Kyushu University*, 5:37–52, 1957.

[83] H. Yamada. On the highest solitary wave. *Research Institute for Applied Mechanics, Kyushu University*, (18):37–52, 1957.

[84] Yumin Yang. The initial value problem of a rising bubble in a two-dimensional

vertical channel. *Physics of Fluids A: Fluid Dynamics*, 4(5):913–920, 1992.